3D POROUS COMPOSITE SCAFFOLD OF PCL-PEG-PCL/Sr^{2+} AND Mg^{2+} IONS CO-DOPED BORATE HYDROXYAPATITE FOR BONE TISSUE ENGINEERING

A THESIS SUBMITTED TO
THE GRADUATE SCHOOL OF NATURAL AND APPLIED SCIENCES
OF
MIDDLE EAST TECHNICAL UNIVERSITY

BY

BUŞRA YEDEKÇİ

IN PARTIAL FULFILLMENT OF THE REQUIREMENTS
FOR
THE DEGREE OF DOCTOR OF PHILOSOPHY
IN
ENGINEERING SCIENCES

SEPTEMBER 2021

Approval of the thesis:

3D POROUS COMPOSITE SCAFFOLD OF PCL-PEG-PCL/Sr^{2+} AND Mg^{2+} IONS CO-DOPED BORATE HYDROXYAPATITE FOR BONE TISSUE ENGINEERING

submitted by **BUŞRA YEDEKÇİ** in partial fulfillment of the requirements for the degree of **Doctor of Philosophy** i**n Engineering Sciences, Middle East Technical University** by,

Prof. Dr. Halil Kalıpçılar
Dean, Graduate School of **Natural and Applied Sciences** _____

Prof. Dr. Murat Dicleli
Head of the Department, **Engineering Sciences** _____

Prof. Dr. Zafer Evis
Supervisor, **Engineering Sciences, METU** _____

Prof. Dr. Ayşen Tezcaner
Co-Supervisor, **Engineering Sciences, METU** _____

Examining Committee Members:

Prof. Dr. Dilek Keskin
Engineering Sciences, METU _____

Prof. Dr. Zafer Evis
Engineering Sciences, METU _____

Prof. Dr. Volkan Şahin
Department of Prosthodontics, Faculty of Dentistry, Kırıkkale University _____

Prof. Dr. Hasan Okuyucu
Metallurgy and Materials Engineering, Ankara Yıldırım Beyazıt University _____

Assist. Prof. Dr. Fatih Akkurt
Chemical Engineering, Gazi University _____

Date: 06.09.2021

I hereby declare that all information in this document has been obtained and presented in accordance with academic rules and ethical conduct. I also declare that, as required by these rules and conduct, I have fully cited and referenced all material and results that are not original to this work.

Name Last name : Buşra Yedekçi

Signature :

ABSTRACT

3D POROUS COMPOSITE SCAFFOLD OF PCL-PEG-PCL/Sr^{2+} AND Mg^{2+} IONS CO-DOPED BORATE HYDROXYAPATITE FOR BONE TISSUE ENGINEERING

Yedekçi, Buşra
Doctor of Philosophy, Engineering Sciences
Supervisor : Prof. Dr. Zafer Evis
Co-Supervisor: Prof. Dr. Ayşen Tezcaner

September 2021, 126 pages

Bioceramic/polymer composite systems have gained importance in treating hard tissue damages using bone tissue engineering (BTE). In this context, it was aimed to develop 3D porous composite PCL-PEG-PCL scaffolds containing different amounts of B, Sr and Mg multi-doped hydroxyapatite (HA) that can provide bone regeneration in the bone defect area and to investigate the effect of both the amount of inorganic phase and the porosity on the mechanical and the biological properties. B-Sr-Mg multi-doped HAs were synthesized by microwave irradiation method and samples were sintered at 700, 900 and 1100°C. Microstructural, mechanical and biological characterization results were evaluated and 4 different groups sintered at 1100°C were selected for scaffold construction. Then, PCL-PEG-PCL copolymer was successfully synthesized with ring opening polymerization method and characterized by FTIR, ^{1}H NMR and GPC analyses. PCL-PEG-PCL composite scaffolds containing different amounts of hydroxyapatite (HA) (10% and 20 wt%) were produced with the desired porosity (50% and 60%) by compression-molding/particulate leaching method. Presence of HA in the scaffolds improved the

mechanical properties. Compressive strength of the scaffolds was between 9.32-24.27 MPa and 20% 2Sr0.5BHA scaffolds were found to have the maximum compressive strength. In the relative cell viability (%) test, the highest viability was observed on the scaffolds with HA and 2Sr0.5BHA. The specific ALP activity level of the cells on the scaffolds containing 2Sr0.5BHA was significantly higher (2.6 times) than that of the control group. It was concluded that PCL-PEG-PCL composite scaffolds with 2Sr0.5BHA have the potential to be used in BTE.

Keywords: B-Sr-Mg multi-doped hydroxyapatite, PCL-PEG-PCL, Composite scaffolds, Bone tissue engineering

ÖZ

KEMİK DOKU MÜHENDİSLİĞİ İÇİN PCL-PEG-PCL/STRONSİYUM VE MAGNEZYUM İYONLARI İLAVE EDİLMİŞ BOR KATKILI HİDROKSİAPATİT İLE 3 BOYUTLU GÖZENEKLİ KOMPOSİT İSKELE ÜRETİMİ

Yedekçi, Buşra
Doktora, Mühendislik Bilimleri
Tez Yöneticisi: Prof. Dr. Zafer Evis
Ortak Tez Yöneticisi: Prof. Dr. Ayşen Tezcaner

Eylül 2021, 126 sayfa

Biyoseramik/polimer kompozit sistemler, kemik doku mühendisliği (BTE) alanında sert doku hasarlarının tedavisinde önem kazanmıştır. Bu kapsamda, kemik hasar alanında kemik rejenerasyonunu sağlayabilen, farklı miktarlarda B, Sr ve Mg çoklu katkılı hidroksiapatit (HA) içeren 3 boyutlu gözenekli kompozit PCL-PEG-PCL iskelelerinin geliştirilmesi, ayrıca hem inorganik faz miktarının hem de gözenekliliğin mekanik ve biyolojik özellikler üzerindeki etkisinin araştırılması amaçlanmıştır. B-Sr-Mg çoklu katkılı HA'lar mikrodalga ışınımı yöntemiyle sentezlenmiş ve örnekler 700, 900 ve 1100°C'de sinterlenmiştir. Mikroyapısal, mekanik ve biyolojik karakterizasyon sonuçları değerlendirilmiş ve iskele yapımı için 1100°C'de sinterlenmiş 4 farklı grup seçilmiştir. Daha sonra PCL-PEG-PCL kopolimeri halka açma polimerizasyon yöntemi ile başarılı bir şekilde sentezlenmiş ve FTIR, ^{1}H NMR ve GPC analizleri ile karakterize edilmiştir. Farklı miktarlarda hidroksiapatit (HA) (ağırlıkça %10 ve %20) içeren PCL-PEG-PCL kompozit iskeleler, basma-kalıplama ve partikül uzaklaştırma yöntemi kullanılarak istenen gözeneklilik (%50 ve %60) seviyesinde üretilmiştir. İskelelerde HA varlığı mekanik

özellikleri iyileştirmiştir. İskelelerin basma dayanımı 9,32-24,27 MPa arasında olup, %20 2Sr0.5BHA içeren iskelerlerde maksimum basma dayanımı tespit edilmiştir. Göreceli hücre canlılığı (%) testinde en yüksek canlılık HA ve 2Sr0.5BHA içeren iskelelerde gözlenmiştir. 2Sr0.5BHA içeren iskeleler üzerindeki hücrelerin spesifik ALP aktivite seviyesi, kontrol grubuna göre önemli ölçüde (2,6 kat) daha yüksektir. 2Sr0.5BHA içeren PCL-PEG-PCL kompozit iskelelerin BTE'de kullanılma potansiyeli olduğu sonucuna varılmıştır.

Anahtar Kelimeler: B-Sr-Mg çoklu-katkılı hidroksiapatit, PCL-PEG-PCL, Kompozit iskeleler, Kemik doku mühendisliği

To my family, my husband, my son and my daughter in womb,

ACKNOWLEDGMENTS

My deepest gratitude is to my supervisor, Prof. Dr. Zafer Evis and my co-supervisor Prof. Dr. Ayşen Tezcaner for their guidance, critism, advice and patience throughout the research.

In my daily work I appreciate my all lab members, especially Deniz Atila, Ali Deniz Dalgıç, Engin Pazarçeviren, Hossein Jodati for their help and friendship.

I would like to express my heart-felt gratitude to my dear family for their unconditional support all these years. They have supported me whenever I needed it. I am so grateful to have a son, Oğuz, who is the source of my life energy and cheer me up everytime I see him. And in particular, I must acknowledge my husband and best friend, Yağız Yedekçi, without whose love, encouragement and guidance, I would not have finished this thesis.

This work is partially funded by Scientific and Technological Research Council of Turkey under grant number TUBİTAK 217M264.

TABLE OF CONTENTS

ABSTRACT v

ÖZ vii

ACKNOWLEDGMENTS x

TABLE OF CONTENTS xi

LIST OF TABLES xv

LIST OF FIGURES xvii

1. INTRODUCTION 1

1.1 Biomaterials 1

1.1.1 Bioceramics 1

1.1.1.1 Hydroxyapatite 2

1.1.1.2 Ion-doping into Hydroxyapatite 2

1.1.1.3 Boron doped HA 3

1.1.1.4 Strontium doped HA 6

1.1.1.5 Magnesium doped HA 9

1.1.1.6 Co-doping of different ions into HA 11

1.1.2 Polymers 12

1.1.2.1 Poly (ε-caprolactone) 13

1.1.2.2 Poly (ethylene glycol) 13

1.1.2.3 Poly (ε-caprolactone) - poly (ethylene glycol) - poly (ε-caprolactone) 14

1.1.3 Composite Materials 15

1.2 Aim of the Study 16

2. MATERIALS AND METHODS 17
2.1 MATERIALS 17
2.2 METHODS 18
2.2.1 Synthesis and Characterization of B, Sr and Mg Multi-Doped Hydroxyapatite 18
2.2.1.1 Synthesis of B, Sr and Mg Multi-Doped Hydroxyapatite 18
2.2.1.2 Structural Characterization 20
2.2.1.2.1 X-Ray Diffraction Analysis 20
2.2.1.2.2 Fourier Transform Infrared Spectroscopy (FTIR) 20
2.2.1.2.3 Thermogravimetric Analysis (TGA) 21
2.2.1.2.4 Inductively Coupled Plasma-Mass Spectrometry (ICP-MS) 21
2.2.1.2.5 Density Measurements 21
2.2.1.2.6 Vicker's Microhardness Measurements 22
2.2.1.2.7 Scanning Electron Microscopy (SEM) 22
2.2.1.3 Mechanical Properties 23
2.2.1.3.1 Compression Test 23
2.2.1.3.2 Diametral Test 23
2.2.1.4 Biological Characterization 24
2.2.1.4.1 Alamar Blue™ Cell Viability Test 24
2.2.1.4.2 Alkaline Phosphatase (ALP) Activity Test 25
2.2.2 Synthesis and Characterization of PCL-PEG-PCL 26
2.2.2.1 Synthesis of PCL-PEG-PCL 26
2.2.2.2 Fourier Transform Infrared Spectroscopy (FTIR) 27
2.2.2.3 Proton Nuclear Magnetic Resonance (^{1}H NMR) Spectroscopy 27

2.2.2.4 Gel Permeation Chromatography (GPC) 28
2.2.3 Production and Characterization of PCL-PEG-PCL/B, Sr, Mg Multi-Doped Hydroxyapatite Composite Scaffolds 28
2.2.3.1 Production of Composite Scaffolds 28
2.2.3.2 Determination of Porosity of Scaffolds 30
2.2.3.3 Thermogravimetric (TGA) Analysis of Scaffolds 31
2.2.3.4 *In Vitro* Degradation and Water Uptake Test 31
2.2.3.5 *In Vitro* Bioactivity Analysis 32
2.2.3.6 Compression Test 32
2.2.3.7 Cell Culture Studies 32
2.2.3.7.1 Alamar Blue™ Cell Viability Test 33
2.2.3.7.2 Osteogenic Activity of Cells 34
2.2.4 Statistical Analysis 35
3. RESULTS AND DISCUSSION 37
3.1 Characterization of B, Sr and Mg Multi-Doped Hydroxyapatite 37
3.1.1 Structural Characterization 37
3.1.1.1 X-Ray Diffraction Analysis 37
3.1.1.2 Fourier Transform Infrared Spectroscopy (FTIR) 44
3.1.1.3 Thermogravimetric Analysis (TGA) 46
3.1.1.4 Inductively Coupled Plasma-Mass Spectrometry (ICP-MS) 47
3.1.1.5 Density Measurements 50
3.1.1.6 Vicker's Microhardness Measurements 53
3.1.1.7 Scanning Electron Microscopy (SEM) 55
3.1.2 Mechanical Properties 59

3.1.2.1 Compression Test 59
3.1.2.2 Diametral Test 60
3.1.3 Biological Characterization 62
3.1.3.1 Alamar Blue™ Cell Viability Test 62
3.1.3.2 Alkaline Phosphatase (ALP) Activity Test 66
3.2 Characterization of PCL-PEG-PCL 69
3.2.1 Fourier Transform Infrared Spectroscopy (FTIR) 69
3.2.2 Proton Nuclear Magnetic Resonance (^{1}H NMR) Spectroscopy 70
3.2.3 Gel Permeation Chromatography (GPC) 71
3.3 Characterization of PCL-PEG-PCL/B, Sr, Mg Multi-Doped Hydroxyapatite Composite Scaffolds 72
3.3.1 Production of Composite Scaffolds 72
3.3.2 Determination of Porosity of Scaffolds 72
3.3.3 Thermogravimetric (TGA) Analysis of Scaffolds 74
3.3.4 *In Vitro* Degradation and Water Uptake Test 75
3.3.5 *In Vitro* Bioactivity Analysis 78
3.3.6 Compression Test 83
3.3.7 Cell Culture Studies 86
3.3.7.1 Alamar Blue™ Cell Viability Test 86
3.3.7.2 Osteogenic Activity of Cells 89
4. CONCLUSION 93
REFERENCES 95
CURRICULUM VITAE 125

LIST OF TABLES

TABLES

Table 1. Parameters of B doped HAs..... 5
Table 2. Parameters of Sr doped HAs..... 7
Table 3. Parameters of Mg doped HAs..... 10
Table 4. Molar concentrations of the elements used in the preparation of pure and doped HAs. 19
Table 5. Amount of components used for the preparation of B-Sr-Mg doped HA composite scaffolds..... 30
Table 6. Amount of phases in the multi doped HAs after the XRD analysis calculated by the relative intensity ratio (RIR). 40
Table 7. Degree of crystallinity of the multi doped HAs calculated from the XRD analysis..... 42
Table 8. Lattice parameters of the samples..... 43
Table 9. ICP-MS analysis of the multi-doped HA samples sintered at different temperatures. 49
Table 10. The effect of sintering temperature and ion-doping on average and relative densities of the samples (n = 10, mean ± standard deviation). 51
Table 11. Vicker's microhardness of the samples (n=5, mean ± standard deviation). 55
Table 12. Average grain size of samples sintered at different temperatures. 58
Table 13. Compressive strength of samples sintered at 700, 900 and 1100°C (n=10). 59
Table 14. Diametral strength of the samples (n=10, mean ± standard deviation). . 61
Table 15. Average molecular weights of synthesized PCL-PEG-PCL triblock copolymer according to ^{1}H NMR and GPC analyses 71
Table 16. Theoretical and experimental weight changes in scaffolds by removal of NaCl and experimental porosity of the scaffolds (n = 5)..... 73

Table 17. The amount of HA in the scaffolds 74
Table 18. Compressive strength and compressive modulus of the scaffolds (n=10) 85

LIST OF FIGURES

FIGURES

Figure 1. Synthesis procedure of HA. A) Chemical reaction of the precursors, B) Microwave irradiation, C) Washing and filtering operation. 19
Figure 2. Experimental setup of PCL-PEG-PCL synthesis 27
Figure 3. The general outlook of scaffolds before leaching 29
Figure 4. XRD patterns of the samples sintered at A) 700°C, B) 900°C and C) 1100°C. Vertical solid lines indicate the peaks of standard HA (PDF#09-0432) and dash lines β-TCP (PDF#09-0169). 38
Figure 5. FTIR spectra of the samples sintered at A) 700°C, B) 900°C and C) 1100°C. 45
Figure 6. Thermal gravimetric analysis (TGA) curves displaying the mass loss of pure and doped HA samples. 47
Figure 7. General view of HA particles sintered at A)700°C, B)900°C and C)1100°C; a) HA, b) 0.5BHA, c) 2Sr0.5BHA, d) 1Sr0.25Mg0.5BHA, e) 0.75Sr0.5Mg0.5BHA, f) 0.5Sr0.75Mg0.5BHA, g) 0.25Sr1Mg0.5BHA, h) 1Mg0.5BHA. Images provided evidence of increased grain size with increasing sintering temperatures. 57
Figure 8. Viability of Saos-2 cells on pure and doped HA sintered at A) 700°C, B) 900°C and C) 1100° C and incubated for 1, 4 and 7 days (n=4). The error bars represent the standard error of means. For Figures A and B at day 1 there was significant difference ($p<0.05$) between pure HA and all groups sintered at the same temperature, except the groups indicated with # ($p>0.05$). α and β denote statistical difference between the group and pure HA group, at day 1 (α: $p<0.01$, β: $p<0.05$). 65
Figure 9. Specific ALP activity of Saos-2 cells seeded on pure and doped HA sintered at A) 700°C, B) 900°C and C) 1100°C and incubated in osteogenic differentiation medium at 37°C for 7 and 14 days (n=4). The error bars represent the standard error of means. For Figures A and B there was significant difference ($p<0.05$) between pure HA and all groups sintered at the same temperature at day 7,

except the groups indicated with # ($p>0.05$). β implies the difference between pure HA and the given group at day 7 ($p<0.05$). 67
Figure 10. A) FTIR spectrum of synthesized PCL-PEG-PCL copolymer, B) ^{1}H NMR spectrum of synthesized PCL-PEG-PCL copolymer 70
Figure 11. Water uptake capacity of the composite scaffolds containing A) 10% and B) 20% inorganic phase (n = 3). The water uptake capacity of the groups marked with * is significantly different from the 50% porous groups ($p<0.05$) at each incubation period. A significant difference is found between the water uptake capacity in the group marked with # and the other groups ($p<0.05$). 77
Figure 12. CaP accumulation on 50% porous scaffolds after 1, 7 and 14 days of incubation in SBF at 37ºC. 80
Figure 13. CaP accumulation on 60% porous scaffolds after 1, 7 and 14 days of incubation in SBF at 37ºC. 81
Figure 14. Change in the pH of SBF in which PCL-PEG-PCL/B-Sr-Mg doped HA scaffolds are incubated (n = 5) 82
Figure 15. Relative cellular viability of Saos-2 cells on A) 50% porous B) 60% porous pure PCL-PEG-PCL and PCL-PEG-PCL / B-Sr-Mg doped HA composite scaffolds. Samples are incubated for 1, 4 and 7 days (n = 4). At each incubation period, a significant difference is found between the cell viability in the groups marked with *, &, £ and the other groups ($p<0.05$). The groups marked with £ do not differ significantly among themselves. Groups marked with # are significantly different from all groups ($p <0.01$). Viability on pure PCL-PEG-PCL was accepted as 100%. 88
Figure 16. Specific ALP activity of Saos-2 cells seeded on A) 50% porous, B) 60% porous PCL-PEG-PCL/B-Sr-Mg doped HA composite scaffolds. Samples were incubated in osteogenic differentiation medium at 37°C for 7 and 14 days (n = 4). Error bars represent the standard error of the means (n = 4). A statistically significant difference ($p <0.01$) in the ALP activity is found between the groups indicated by $ and the other groups. While the groups marked with $* do not differ significantly

within themselves, they are different from the other groups at a level of significance of 0.01. 91
Figure 17. The amount of intracellular calcium accumulation of Saos-2 cells seeded on composite scaffolds with A) 50% porosity, B) 60% porosity. Samples were incubated in osteogenic differentiation medium at 37°C for 7 and 14 days (n = 4). Error bars represent the standard error of the means (n = 4). A statistically significant difference ($p < 0.01$) is found between the groups indicated by $ and the other groups. While the groups marked with $* do not differ significantly within themselves, they are different from the other groups at a level of significance of 0.01..... 92

CHAPTER 1

INTRODUCTION

1.1 Biomaterials

Biomaterials science is a field that has been developing rapidly since the 1940s and raises people's living standards by playing an important role in the treatment of some previously incurable diseases. It is an interdisciplinary science that covers engineering, medicine and basic sciences such as biology, chemistry, physics. The definition of biomaterial term was first defined in 1987 (Williams, 1987), then it was redefined multiple times. The latest definition was done at 2005 by the European Society for Biomaterials Consensus Conference II as “Material intended to interface with biological systems to evaluate, treat, augment, or replace any tissue, organ or function of the body”.

Biomaterials can be classified as metals, ceramics, polymers, naturally derived materials and composites. Also, they can be categorized as inert, bioactive and biomimetic materials according to the response they elicit from living tissues.

1.1.1 Bioceramics

In biomedical applications, bioceramics are frequently used for the repair and replacement of damaged hard tissues (Bohner, 2000; Dorozhkin, 2009; Jodati et al., 2020) as surface coating of metallic implants for increasing cellular adhesion and initial bone formation (Avcı et al., 2017; Ke et al., 2019) and as scaffolds for BTE (Feng et al., 2020; Shuai et al., 2021; Swetha et al., 2010). Considering that approximately 2.9 million joint replacement surgeries which include 1.4 million hip,

1.1 million knee, and over 100,000 shoulder replacements are performed annually (Vetalice, 2012), the high demand for orthopaedic implants can be easily understood. Bone grafts are needed for bone defects including tumour resection, congenital malformation, trauma, fractures, surgery, osteoporosis and arthritis and more than 2.2 million bone graft operations are carried out worldwide per year (Jimi et al., 2012; Kashte et al., 2017). Therefore, the development of bone substitutes having similar or superior features as of biological bone has gained importance for efficient treatment.

1.1.1.1 Hydroxyapatite

Among the bioceramics, hydroxyapatite (HA) is one of the most remarkable because its elemental composition has a great resemblance to minerals found in bone and teeth (Lusvardi et al., 2002). HA which is also known as bone mineral, has a hexagonal structure with chemical formula of $Ca_{10}(PO_4)_6(OH)_2$. Under physiological condition, it is thermodynamically the most stable calcium phosphate (CaP) (Kalita et al., 2007).

Synthetic HA differs from biological HA in mechanical properties and thermal stability. Magnesium (Mg), sodium (Na), strontium (Sr), zinc (Zn), potassium (K), fluorine (F) and carbonate ($CaCO_3$) are present in the structure of biological HA (Aaseth et al., 2012). The concentrations of these ions vary with the age of hard tissue. Even in small quantities, their presence is of vital importance in the bone formation process and they play an active role against diseases that can affect the bone.

1.1.1.2 Ion-doping into Hydroxyapatite

To mimic the chemical composition of biological apatite containing trace ions, many ions can be doped into synthetic HA. Some of them are silver (Ag), copper (Cu), boron (B), selenium (Se) and Sr due to their antibacterial effects (Grubova et al.,

2015; Radovanović et al., 2014; Ravi et al., 2012; Rodríguez-Valencia et al., 2013; Yılmaz and Evis, 2016), chlorine (Cl), F, Zn, Sr, Mg, $CaCO_3$ and silicate (Si) for improving HA's bioactivity, biocompatibility and/or mechanical properties (Sun et al., 2010; Surmeneva et al., 2013; Uysal et al., 2013; Zhu et al., 2015).

The methods mainly used to dope ions into the HA structure are the chemical precipitation, sol-gel, mechanochemical and hydrothermal synthesis methods. The synthesis of HA by microwave irradiation in hydrothermal synthesis is frequently preferred in recent years due to the fact that the process is very fast and simple. The crystallinity of the HA powders obtained with this method is also very high (Alshemary et al., 2018; İpekoglu and Altıntaş, 2009).

1.1.1.3 Boron doped HA

The deficiency of boron (B), which is considered to be an essential nutrient for humans, is associated with osteoporosis (Price et al., 2012). B has also a regulatory effect on the *in vitro* activity of osteoblastic cells depending on the concentration (Yılmaz and Evis, 2016). B incorporation into HA during synthesis has a beneficial effect on apatite formation (Barheine et al., 2011; Hakkı et al., 2010). When B is introduced into HA lattice, it mostly replaces PO_4^{3-} groups. Sintering has also great importance in the synthesis of B-doped HAs. When HA is sintered above 900 °C, chemical reactions that result in the formation of β-tricalcium phosphate (β-TCP) phase transformation to α-tricalcium phosphate (α-TCP) at 1200 °C along with the formation of B-doped HA particles occur (Hayakawa et al., 2007). In addition to sintering temperature, the amount of B to be doped to HA's structure is also very important. When the ratio of P/B is 7.22, borate groups could enter the lattice structure of HA. Secondary phases were observed when the B ratio was increased. (Ternane et al., 2002). Mechanical, optical and dielectric properties and morphology of B-doped HA depend on the amount of B in its structure. 5 wt% B_2O_3 addition improved the bending strength and fracture toughness while it reduced the

degradation rate. More than 5 wt% doping decreased the bending strength and fracture toughness and increased degradation rate (Yang et al., 2010).

While HA polarization is important for drug release systems, its UV protection effect is also important to prevent damage of hazardous UV rays. It was shown that B-doped HAs synthesized for the improvement of these properties exhibited good protection in the 200-400 nm UV region and exhibited ferroelectric properties, hence it was reported that B-doped HAs can be used in drug release systems and bioceramic applications (AlHammad, 2016). Parameters of B doped HA in literature are provided in Table 1.

Table 1. Parameters of B doped HAs

Parameters of BHA in the Composites							
B content (x)	**Sintering Temp. (°C)**	**Lattice Parameters**			**Synthesis Method**	**Phases**	**Reference**
$Ca_{10}(PO_4)_{6-x}(BO_3)_x(OH)_2$		a (Å)	c (Å)	V (Å^3)			
0, 0.08, 0.017 and 0.034	1000				Acid-Base	HA and β-TCP	(Albayrak, 2016)
	1100						
	1200						
0.20	1200	9.5960	6.9730	556.1	Solid-State Reaction		(Güler et al., 2011)
0.07	700, 900 and 1200				Wet Chemical Processing	HA, β-TCP and α-TCP	(Hayakawa et al., 2007)
0.00	1000	9.4180	6.8840	528.8	Solid-State Reaction	HA and β-TCP	(Ternane et al., 2002)
0.10		9.4130	6.8880	528.5			
0.20		9.4090	6.8925	528.4			
0.30		9.3991	6.8995	527.9			
0.40		9.3831	6.9084	526.7			
0.50		9.3763	6.9116	526.2			
0.60		9.3760	6.9122	526.2			
0	1200	9.4060	6.8820	527.3	High Temperature Solid-State Reaction	HA	(Bahreine et al., 2011)
0.5		9.3890	6.9040	527.1		HA	
1		9.3890	6.9270	528.8		HA, CaO	
1.2		9.4000	6.9170	529.3		HA, α-TCP	
0	1100	9.4221	6.8881	611.5	Wet Precipitation/Microwave Reflux Method	HA and β-TCP	(Pazarçeviren et al., 2021)
1		9.4234	6.8884	611.7			
2		9.4236	6.8887	611.7			
3		9.4223	6.8899	611.7			
5		9.4195	6.8931	611.6			
10		9.4047	6.9083	611.0			
2	1000				Sol Gel	HA	(Atila et al., 2019)

1.1.1.4 Strontium doped HA

The trace amount of Sr in the human body improves bone strength, bone healing and bone microarchitecture (Bose et al., 2013). It increases bone collagen synthesis and preosteoblastic proliferation, while prevents osteoclast differentiation. For this reason, Sr is a promising candidate for osseointegration. Most of the Sr, physically and chemically very similar to Ca, is located in the bone tissue (Guo et al., 2005). Under normal conditions, it has been reported that 99.1% of the body-absorbed Sr is stored in bones and the ratio in the Sr / Ca bone changes from 1:1000 to 1:2000, just as it is in the blood serum (Cabrera et al., 1999). In addition, many studies have shown that Sr increases bone formation and reduces bone resorption (Marie et al., 2001; Meunier, 2002). Sr takes the place of Ca in the structure of HA to reduce the degradation or to improve the mechanical, biological and antibacterial properties of bioceramic (Bigi et al., 2007). Sr, which can participate in the HA structure with more than one element, has positive effects on hard tissues (Gao et al., 2017).

It was found that Sr can be added to the structure of HA up to 4 mol%. Even when the amount of Sr was 4 mol%, it was revealed that the main phase was HA. Although the thermal stability of Sr-added HA was slightly lower than that of pure HA, it was shown that it can be used for medical applications due to its ability to increase bone formation (Özbek et al., 2016). In the study by Kaygılı et al. (2015) a low amount of Sr-added HA was synthesized and it was found that the synthesized HA was in 95% pure phase. In the same study, when Sr was added to the HA structure, the average crystallite size calculated from XRD was found in the range of 21-27 nm (Kaygılı et al., 2015). Sr doped HAs in literature are presented in Table 2.

Table 2. Parameters of Sr doped HAs

Parameters of SrHA in the Composites							
Sr content (y)	**Sintering Temp. (°C)**	**Lattice Parameters**			**Synthesis Method**	**Phases**	**Reference**
$Ca_{10-y}Sr_y(PO_4)_6(OH)_2$		a (Å)	c (Å)	V ($Å^3$)			
0.03		9.4437	6.8918	532.3	Direct Synthesis in an Aqueous Medium	HA	(Bigi et al., 2007)
0.05		9.4511	6.9017	533.9			
0.5		9.63	7.1026	570.4			
0		9.4269	6.884	529.8	Wet Chemical Processing	HA	(Capuccini et al., 2009)
0.01		9.4375	6.8909	531.5			
0.03		9.4437	6.8918	532.3			
0.07		9.4511	6.9017	533.9			
0.06	1200				Microwave Sintering	HA, β-TCP, α-TCP	(Curran et al., 2011)
0.11					Conventional Sintering	HA, β-TCP, α-TCP	
0	1500				Precipitation	Tetracalcium phosphate (TTCP), dicalcium phosphate anhydrous (DCPA) and dicalcium phosphate dihydrate (DCPD).	(Guo et al., 2005)
0.06							
0.11							

Table 2. (Continued)

Parameters of SrHA in the Composites							
Sr content (y)	**Sintering Temp. (°C)**	**Lattice Parameters**			**Synthesis Method**	**Phases**	**Reference**
$Ca_{10-y}Sr_y(PO_4)_6(OH)_2$		a (Å)	c (Å)	V ($Å^3$)			
0		9.381	6.849	522	Sol Gel	HA	(Kaygılı et al., 2015)
0.45		9.408	6.885	527.8		HA and β-TCP	
0.9		9.404	6.88	526.9			
1.35		9.408	6.87	526.6			
1.8		9.413	6.875	527.5			
2.25		9.395	6.875	525.5			
0.11					Precipitation and Calcination		(Ni et al., 2006)
0.11	800				Radio Frequency (RF) Plasma Spray	HA, β-TCP, α-TCP	(Roy et al., 2011)
0.1	900	9.42	6.88		Wet Chemical Method	HA	(Zhu et al., 2018)
1		9.44	6.9				
2		9.45	6.92				
2	1200				Chemical Precipitation	HA	(Özbek et al., 2016)
4						HA, β-TCP	

1.1.1.5 Magnesium doped HA

Enamel, dentin, and bone contain 0.44 wt%, 1.23 wt% and 0.72 wt% Mg, respectively (Cacciotti et al., 2009; Suchanek et al., 2004). Accordingly, Mg-substituted HA materials (Mg-HA) were expected to have excellent biocompatibility. Mg plays a key role in bone metabolism by stimulating osteoblasts in early stages of osteogenesis (Rude and Gruber, 2004). The presence of Mg^{2+} ions in the HA structure affects the crystallization of HA in solution and its thermal stability and accelerates the formation of β-TCP as a result of sintering, thus biphasic calcium phosphates (BCP) formation (Cacciotti et al., 2009). Therefore, when it is desired to obtain a pure HA phase, it is important that the amount of Mg in the HA should not be above a certain value.

According to the literature, the replacement of Mg with Ca is limited in HA. This is related to the large size difference between the Mg^{2+} and Ca^{2+} ions, which causes degradation in the HA lattice and reduction of the crystal structure (Laurencin et al., 2011). The maximum amount of Mg ions replacement for the Ca ions varies from 0.3 to 29 wt%. However, the amount of Mg in the structure of synthetic HA is about 0.4 wt% (Suchanek et al., 2004). However, under hydrothermal conditions, HA containing up to 7.5 wt% of Mg can be synthesized (Bigi et al., 1993). When more than this amount of Mg is doped, the material became completely amorphous and it was observed that the maximum amount of 1.7 wt% Mg^{2+} ion could be added to the HA structure. Substitution of Mg for Ca in apatite lattice resulted in a slight increase in ‘a’ lattice and a decrease in ‘c’ lattice parameters (Farzadi et al., 2014). Mg doped HAs in literature are presented in Table 3.

Table 3. Parameters of Mg doped HAs

Parameters of MgHA in the Composites							
Mg content (z)	**Sintering Temp. (°C)**	**Lattice Parameters**			**Synthesis Method**	**Phases**	**Reference**
$Ca_{10-z}Mg_z(PO_4)_6(OH)_2$		a (Å)	c (Å)	V ($Å^3$)			
0.01	700 and 1100	9.4190	6.8770	528.4	Precipitation	HA and β-TCP	(Bertoni et al., 1998)
0.05		9.4120	6.8680	526.9			
0.10		9.4270	6.8580	527.8			
0, 0.25, 0.5 and 1	1000				Precipitation	HA, β-TCP, α-TCP	(Cacciotti et al., 2009)
0.1, 0.25, 0.5 and 1	300, 500, 700, and 1000				Microvawe	HA, β-TCP	(Fadeev et al., 2003)
0.11	900	9.4272	6.8614	528.1	Wet Chemical Processing	HA	(Farzadi et al., 2014)
0.24	900	9.4242	6.8844	529.5			
0.04	500				Water Based Sol Gel Powder Processing	HA	(Kalita and Bhatt, 2007)
0.10							
0.16							
0.57					Precipitation	HA	(Landi et al., 2008)
1.00		9.4000	6.9500	531.8	Wet Chemical Processing	HA, β-TCP	(Laurencin et al., 2011)
0.04	800				Radio Frequency (RF) Plasma Spray	HA	(Roy et al., 2011)
0.1 to 1.1	900				Mechanochemical – Hydrothermal	HA	(Suchanek et al., 2004)
0.04	1100				Wet Chemical Precipitation	HA, β-TCP	(Salma-Ancane et al., 2013)
0.40							
1.24							
4.13							
0.15	1250	9.4100	6.8700	526.8	Precipitation	HA, β-TCP, α-TCP	(Tampieri et al., 2004)
0.20		9.3850	6.8390	521.6			
0.25		9.3950	6.8400	522.8			
0.30		9.3900	6.8600	523.8			

1.1.1.6 Co-doping of different ions into HA

Over the past decade, considerable amount of experimental and theoretical studies have been carried out on the co-doping of more than one ion to HA structure. The ability to use the unique properties of different ions which has become an important strategy, provides great contributions in the field of tissue engineering. Besides the improved biological and mechanical properties, the magnetic and electronic properties can be enhanced, and it is also possible to gain advantages in stability and antibacterial properties of HA by co-doping of various ions.

In many *in vitro* studies, it was reported that implants coated with Ag^{+}, Cu^{2+} and Zn^{2+} ions play an important role in preventing or reducing bacterial adhesion (Chen et al., 2006; Heidenau et al., 2005). The results showed that HA with Cu and Zn added has antibacterial effects on bone repair or coating of implants (Stanić et al., 2010).

Europium and gadolinium co-doped HA nanorods were shown to have potential to be used as model imaging material for *in vitro* and *in vivo* magnetic resonance (MR) imaging, photoluminescence imaging, and computed tomography (CT) imaging (Chen et al., 2011). This feature has also been shown to be useful in biomedical field drug delivery systems (Chen et al., 2011).

Mg^{2+} and Sr^{2+} ions can be added one by one or co-doped to the HA structure. It was observed that when Mg-Sr is co-added, the crystallinity of HA decreased and that it contained HA and β-TCP phases together. As a result, by making changes in the amount of ions to be added it is possible to produce materials with the desired properties like crystallinity and phases (Aina et al., 2012). Sr and Mg containing calcium phosphates were shown to enhance the antimicrobial efficacy of antibiotics *in vitro*, and are biocompatible. They were reported to be useful in controlled drug delivery systems (Marques et al., 2016).

1.1.2 Polymers

Polymeric materials attract a lot of attention in BTE applications since they have a lot of useful features. These materials have biodegradability, biocompatibility, custom form and size, degradation rate that matches bone tissue regeneration rate, high surface to volume ratio for adsorption of bone related biological molecules, and so on (Makadia and Siegel, 2011).

Polymeric materials can be obtained synthetically or derived from natural sources. Despite the fact that natural polymers are biocompatible, they nonetheless present problems in *in vivo* systems. Xenogeneic or allogeneic biological molecules cause a large inflammatory response and disease transmission since they are derived from a natural source (Badylak and Gilbert, 2008). Natural polymers, on the other hand, lack the desired processability and are prohibitively expensive, even in small quantities (Sabir et al., 2009). Synthetic polymers, on the other hand, can be designed to be biodegradable and biocompatible on demand, with no inflammatory response (Nair and Laurencin, 2007). The polymerization reactions can also be tracked and regulated. As a result, the intrinsic features of the synthesized molecules can be changed, making them extremely processable. As a result, hydrophilicity or hydrophobicity, chain length, functional groups on chains, and the addition of biological molecules to synthetic polymers may all be easily handled (Kohane and Langer, 2008).

Because of their biocompatibility, non-cytotoxic degradation products, easily controlled degradation rates, and porosity, biocompatible synthetic polymers such as poly (caprolactone) (PCL) and poly (ethylene glycol) (PEG) have been commonly employed as scaffold materials in BTE studies (Bose et al., 2012; Kutikov and Song, 2013; Lin et al., 2013; Yang and Pierstorff, 2012).

1.1.2.1 Poly (ε-caprolactone)

PCL is a type of aliphatic polyester made from the monomer ε-caprolactone. PCL appears as one of the most commonly used FDA approved synthetic polymers in BTE scaffolds due to its biocompatibility (Chang et al., 2009; Erdemli et al., 2010). PCL has a high degree of crystallinity and hydrophobicity, hence it takes a long time to degrade *in vivo*, nearly three or four years (Woodruff and Hutmacher, 2010). Pure PCL scaffolds' slow *in vivo* degradation kinetics may limit its use as a versatile matrix material, and natural bone tissue regrowth may be inefficient within pure PCL scaffolds. PCL blended with hydrophilic and rapidly degrading functional polymers, as well as PCL composite scaffolds with bioactive molecules, have been widely used in BTE to solve this inconveniency. PCL, for example, can be used with natural polymers like gelatin, alginate, and collagen in composite scaffolds to increase cellular adhesion, wettability, and biodegradation (Chong et al., 2007; Gautam et al., 2013; Kim and Kim, 2015). The preparation of composite scaffolds using inorganic bioactive ceramics like HA and PCL has also been researched in the literature, and these scaffolds showed improved bioactivity and hydrophilicity (Heo et al., 2009; Zhao et al., 2008).

1.1.2.2 Poly (ethylene glycol)

PEG is a biocompatible polymer with a high hydrophilicity that makes it easy to hydrolyze. PEG has also been certified by the United States. Internal usage in biomedical research and applications approved by the FDA (Knop et al., 2010). Although unmodified PEG is a non-biodegradable polymer, smaller PEG units of 30 to 50 kDa can be easily extracted from kidneys and used efficiently in the creation of synthetic composite polymers without compromising biocompatibility (Veronese and Pasut, 2005).

PEG has been employed in bone tissue constructs in recent years to increase the hydrophilicity and degradability of scaffolds by combining it with other polymers

and bioactive compounds (Niu et al., 2014; Serra et al., 2014). PEG can be used safely to increase cellular adhesion, cellular guidance, and biocompatibility in bone tissue applications (Dahlin et al., 2014).

Bone morphogenic proteins (BMPs) are biologically active molecules that cause new bone formation and show potential for clinical use in bone defect repair. However, an ideal system for delivering BMPs that can strengthen bone stimulating ability and provide initial mechanical strength and scaffolding for bone development has not yet been developed. Interconnected porous HA and synthetic biodegradable PLA-PEG copolymers were used to create a 3D carrier / scaffold system for BMPs. Using this scaffold, the amount of BMP required was reduced by about one-tenth of the amount needed in the previous studies, thanks to HA's superior osteoconduction ability and PLA-based optimal drug delivery system (Kaito et al., 2005).

1.1.2.3 Poly (ε-caprolactone) - poly (ethylene glycol) - poly (ε-caprolactone)

In some cases, it is not possible to achieve the desired properties of a single polymer. For this reason, the copolymerization of more than one polymer is required. PCL-PEG-PCL (PCEC), produced to optimize the properties of hydrophobic PCL and hydrophilic PEG polymers, has attracted interest in recent years. In general, PCL is highly hydrophobic and degrades very slowly by simple hydrolysis in human body conditions. If PCL is copolymerized with PEG to obtain copolymers, the hydrophilicity and biodegradability can be improved and thus be included in a much wider range of applications (Piao et al., 2003). It was shown that the addition of nano-HA to PCL-PEG-PCL polymer changed the shape and size of the micropores of the composite membranes and increased the tensile strength of the membranes. Moreover, cytotoxicity studies had shown that nano-HA / PCEC membranes had positive effects on cell proliferation and growth. *In vivo* performance of this material yielded very good results. It showed that the new bone initially began to form at the edge of the host bone and then grew towards the center of the defect region. At the end of the 20^{th} week, the defect area was completely covered with cortical bone. As

a result, use of this material for composite scaffolding has been found to have positive effect on bone regeneration and can be used in BTE (Fu et al., 2010).

1.1.3 Composite Materials

A composite material is defined as a specific combination of multiple elements into a new composition or structure in order to acquire the combined materials' best features (Gloria et al., 2010; Nicolais et al., 2010). Composite materials allow for the creation of a new material that combines the properties of the separate materials (Callister Jr, 2000). Various material combinations, such as bioceramics and synthetic polymers, are mixed to overcome the restrictions during the manufacturing of BTE scaffolds for this purpose.

The combination of synthetic polymers with bioceramics offers up a new area of design not just for bioceramics with superior degradation and ion release capabilities, but also for the porous scaffolds with good overall mechanical qualities (Rezwan et al., 2006). The resulting impact of combining these materials can be used to create a successful BTE scaffold.

Scaffolds with biocompatibility, biodegradation, osteoconduction and/or osteoinduction properties and pore size between 1 and 300 μm are used in tissue engineering applications. They are easily formable, and their appropriate mechanical and physical properties make biopolymers suitable candidates for drug delivery systems. PCL and PEG are among the commonly used polymers in drug delivery systems. Drug delivery systems are preferred to conventional drug delivery methods because lower doses are sufficient for treatment, thereby reducing drug side effects.

PCL/HA tissue scaffolds are frequently used for BTE in terms of mechanical and biological properties which provide successful results. The elastic modulus of PCL/HA scaffolds containing 0 wt%, 5 wt%, 10 wt% and 20 wt% HA increased considerably from 0.12 MPa to 2.65 MPa with increasing HA content, while the pore size decreased from 9.2 μm to 4.2 μm. In addition, PCL/HA scaffolds have been

shown to significantly increase *in vitro* cellular responses assessed in terms of cell adhesion, proliferation and osteoblastic differentiation (Choi et al., 2013). The PCL/HA scaffolds with macrochannel had excellent ductility and high compressive strength. Moreover, good cellular responses were observed due to osteoconductivity due to the presence of HA particles (Koh et al., 2006). However, PCL, a highly hydrophobic polymer, degrades slowly in the body because it is insoluble in water and allows the drug to remain trapped in microspheres for a long period (Gaucher et al., 2005). These features can be advantageous as well as being disadvantageous in some cases.

1.2 Aim of the Study

The objective of this study was to synthesize B, Sr and Mg ions multi-doped HAs and to obtain porous composite scaffolds by combining multi-doped HAs with biocompatible and biodegradable PCL-PEG-PCL copolymer for having beneficial effects on bone formation, osteoconduction and bioactivity for BTE. The effect of multi-doping of B, Sr and Mg ions on the crystal structure, mechanical and biological properties of HA sintered at different temperatures was investigated. Then, composite scaffolds were prepared at two different porosity ratios (50% and 60%). The effect of inorganic phase content (10% and 20%) and porosity on the mechanical and the biological features of scaffolds was investigated. It was hypothesized that porous PCL-PEG-PCL/B-Sr-Mg multi-doped HA composite scaffolds with high mechanical strength promote cell proliferation and osteogenic activity so that it can be used in BTE applications.

CHAPTER 2

MATERIALS AND METHODS

2.1 MATERIALS

Calcium nitrate tetrahydrate ($Ca(NO_3)_2{\cdot}4H_2O$) (Merck, Germany) and diammonium hydrogen phosphate ($(NH_4)_2HPO_4$) (Merck, Germany) were used to synthesize pure HA. For the samples with doping, additional compounds were required besides these chemicals. For BO_3^{3-}, Sr^{2+}, Mg^{2+} doped samples, boric acid (H_3BO_3) (Merck, Germany), strontium nitrate ($Sr(NO_3)_2$) (Merck, Germany) and magnesium nitrate ($Mg(NO_3)_2$) were used (Merck, Germany) respectively. pH adjustment was made with ammonia solution (NH4OH) (Merck, Germany).

ε-caprolactone (pure, 97%, Sigma-Aldrich, USA), PEG (Mn: 4000 kDa, Sigma-Aldrich, USA), sodium chloride (NaCl, Biorad USA), calcium chloride dehydrate ($CaCl_2.2H_2O$, Sigma-Aldrich, USA), and 2-amino- 2-methyl 1,3-propanediol (Sigma-Aldrich, USA), Dibutyltin dilaurate (Merck, USA), o-cresophthalein (Merck, USA), 8-hydroxyquinone-5-sulfonic acid (Merck, USA), Sodium dodecyl sulfate (Biorad, USA), Picogreen (Invitrogen, USA), Alamar Blue (Invitrogen, USA), pNPP (Sigma-Aldrich, USA) and other chemicals were all of high purity, and used as received.

2.2 METHODS

2.2.1 Synthesis and Characterization of B, Sr and Mg Multi-Doped Hydroxyapatite

2.2.1.1 Synthesis of B, Sr and Mg Multi-Doped Hydroxyapatite

B, Sr and Mg doped HAs were produced by microwave irradiation method (Alshemary et al., 2018). The precursors for this method were calcium nitrate ($Ca(NO_3)_2.4H_2O$) and diammonium hydrogen phosphate ($(NH_4)_2HPO_4$). Calcium nitrate ($Ca(NO_3)_2.4H_2O$) and diammonium hydrogen phosphate ($(NH_4)_2HPO_4$) were dissolved separately in distilled water. Strontium nitrate ($Sr(NO_3)_2$ and magnesium nitrate ($Mg(NO_3)_2$) were added to the calcium nitrate solution, while boric acid (H_3BO_3) was added to the ammonium phosphate solution. The pH of both solutions was brought to 10 by adding ammonia solution (NH_4OH). The ammonium phosphate solution was added dropwise to the continuously stirred calcium nitrate solution. The pH of the solution was kept constant at 10 by adding ammonia solution. The resulting mixture was stirred at room temperature for 30 minutes. The mixture was then kept in a microwave oven for 15 minutes at 800W. The mixture removed from the microwave was filtered and washed with distilled water until the pH was 7. The resulting precipitate was dried overnight at 200°C to remove excess water and ammonia. The dried samples were sintered either at 700, 900 or 1100°C for 2h. The experimental setup of HA synthesis is given in Figure 1.

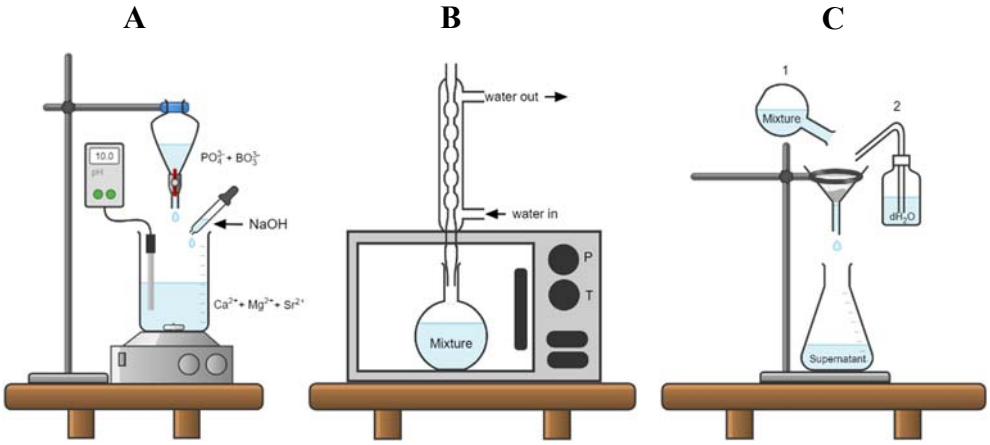

Figure 1. Synthesis procedure of HA. A) Chemical reaction of the precursors, B) Microwave irradiation, C) Washing and filtering operation.

Design of experiment was used to select the doping amount of each ion and sintering temperatures. Amounts of the elements used to prepare the B, Sr and Mg multi-doped HA at different ratios are shown in Table 4. BO_3^{3-}, Sr^{2+} and Mg^{2+} ions are abbreviated as B, Sr and Mg, respectively.

Table 4. Molar concentrations of the elements used in the preparation of pure and doped HAs.

Sample	Ca	P	B	Sr	Mg
HA	10	6	0	0	0
0.5BHA	10	5.5	0.5	0	0
2Sr0.5BHA	8	5.5	0.5	2	0
1Sr0.25Mg0.5BHA	8.75	5.5	0.5	1	0.25
0.75Sr0.5Mg0.5BHA	8.75	5.5	0.5	0.75	0.5
0.5Sr0.75Mg0.5BHA	8.75	5.5	0.5	0.5	0.75
0.25Sr1Mg0.5BHA	8.75	5.5	0.5	0.25	1
1Mg0.5BHA	9	5.5	0.5	0	1

2.2.1.2 Structural Characterization

2.2.1.2.1 X-Ray Diffraction Analysis

XRD analysis of the powders was used to identify the phases present after synthesis. A Rigaku Ultima IV X-ray diffractometer utilizing Cu-Kα radiation at 40 kV and 30 mA was used. The step size and scan rate were fixed at 0.02° and 2°/min, respectively. To compare the positions of diffracted planes, Joint Committee on Powder Diffraction Standards (JCPDS) files were used.

The percentages of β-TCP and HA phases found in the samples were calculated by the relative intensity ratio (RIR) (Equation 1). In Equation 1, $I_{\beta\text{-TCP}}$ and I_{HA} represent the normalized intensities of β-TCP and HA (2 0 1 0) and (2 1 1) peaks, respectively (Farzadi et al., 2011).

$$RIR = I_{\beta-TCP}/(I_{\beta-TCP} + I_{HA}) \quad (1)$$

The degree of crystallinity of crystalline phase available in the analyzed volume from XRD spectra was calculated by

$$X_C = 1 - \left(V_{112/300}/I_{300}\right) \quad (2)$$

where X_C is the degree of crystallinity, I_{300} is the intensity of (3 0 0) reflection and $V_{112/300}$ is the intensity of the hollow between (1 1 2) and (3 0 0) reflection. Lattice parameters (α and c) were analysed by using the software (MDI Jade 6 and UnitCell).

2.2.1.2.2 Fourier Transform Infrared Spectroscopy (FTIR)

The FTIR spectra were used to identify the bonds formed in the HA structure. The spectrum was recorded from 4000 cm^{-1} to 400 cm^{-1} by performing 100 scans on a spectrometer (Perkin Elmer, Norwalk, Conn., USA).

2.2.1.2.3 Thermogravimetric Analysis (TGA)

Thermal behaviour of pure and doped HAs was investigated by heating the sample from 10°C to 1100°C at a heating rate of 20°C/min under air atmosphere (PerkinElmer Pyris 1, PerkinElmer Inc., UK).

2.2.1.2.4 Inductively Coupled Plasma-Mass Spectrometry (ICP-MS)

Inductively coupled plasma-mass spectrometry (ICP-MS, Perkin Elmer Plasma 400) was used to determine the elements in the sample and the Ca/P ratios were also determined using inductively coupled plasma (ICP) analysis results. A total of 1.0 g of the powdered samples were dissolved in 5.0 ml HNO_3 then the evaluation was done by ICP-MS.

2.2.1.2.5 Density Measurements

Using Equation 3, the density of the disc-shaped samples after sintering was calculated using the mass and volume values according to the Archimede's principle, where d represents the density, m the mass and V the volume of the sample.

$$d = m / V \tag{3}$$

Dry weight and the wet weight of the samples immersed in dH_2O were measured. The volume of the samples (V) was calculated using the following formula (Equation 4) (Fuh et al., 2017; Hing et al., 1999):

$$Volume\ (V) = Dry\ weight - Wet\ weight \tag{4}$$

Then the density is calculated as follows (Equation 5);

$$Density = [Dry\ weight\ /\ (Dry\ weight - Wet\ weight)] \times \rho_{H_2O} \tag{5}$$

The relative densities of pure and doped HAs were calculated according to the theoretical density of pure HA which is 3.156 g/cm^3. Density measurements were done by using 3 identical disc-shaped samples of each group.

2.2.1.2.6 Vicker's Microhardness Measurements

The Vicker's microhardness tester (HMV-2, Shimadzu, Japan) was used to detect the microhardness of the samples. Samples were sintered at 700, 900 and 1100°C after disc shaping. After the samples were prepared, 1.962 N (200 g) force was applied to the surface of the samples for 10 seconds with a diamond indent. Diagonal lengths of the indentation were measured to determine the microhardness of the samples. Vicker's microhardness values of 3 different samples from each composition were determined by taking 10 different measurements from each sample. The following formula was used for calculation (Equation 6):

$$HV = 1.854\, P/d^2 \qquad (6)$$

Here, HV refers to the Vicker's microhardness (MPa), P is the applied load (N) and d is the average of the diagonal distance of the recess (mm).

2.2.1.2.7 Scanning Electron Microscopy (SEM)

SEM analysis was performed to determine the morphology and grain size of pure and doped HA particles. SEM analysis was performed with QUANTA 400F Field Emission SEM, USA device with a resolution of 1.2 nm. Samples were mounted onto metal stubs using carbon tape, vacuum-coated with gold by using Hummle VII sputter coating device (Anatech, USA) for SEM analysis.

2.2.1.3 Mechanical Properties

2.2.1.3.1 Compression Test

A universal tester with 5 kN load cell (Instron 5944, USA, TOBB-ETU) at a crosshead speed of 0.1 mm/min was used to determine the compressive strength of the samples and the data were recorded using the instrument's own computer software. The compression test was continued until fracture was obtained. 3 samples were used for each group. Samples were made into cylinders having 12.5 mm diameter, ~1 cm thickness, 2 g mass by applying 22.241 kN (≈5000 lbs) force with uniaxial cold press (Carver, USA). They were then sintered at 700, 900 and 1100°C for 2 h and made ready for testing.

2.2.1.3.2 Diametral Test

Diametral test, which is an alternative to bending test, is frequently preferred especially for biomaterials used in dentistry because the stresses created *in vivo* for dental implants are similar to those produced by diametral test (Speirs et al., 2005; Xu et al., 2007; Zandinejad et al., 2006). For the diametral test, a universal tester (Instron 5944, USA, TOBB-ETU) with a 2 kN load cell was used to perform the diametral test of the samples and the data were recorded using the instrument's computer software. The diametral test was continued until fracture. 5 samples were used for each group. Samples were made with 12.5 mm diameter, 1 mm thickness, 300 mg discs and applied a force of 22.241 kN (≈5000 lbs) with uniaxial cold press (Carver, USA). They were then sintered at 700, 900 and 1100°C for 2 h and made ready for testing.

The diametral strength of discs was calculated by Equation 7 (Evis and Öztürk, 2008). S in the equation represents diametral strength, while F represents the breaking force, D is the sample diameter and t represents the sample thickness. 5 identical discs from each group were tested for determining diametral strength.

$$S = \frac{2F}{\pi D t} \quad (7)$$

2.2.1.4 Biological Characterization

2.2.1.4.1 Alamar Blue™ Cell Viability Test

Cell compatibility of synthesized pure and multi-ion-doped HA's was investigated by *in vitro* cytotoxicity test. Human osteosarcoma cell line (Saos-2, ATCC) was used for *in vitro* cell culture studies. Saos-2 bone cells were cultured in Dulbecco's Modified Eagle's medium (DMEM) supplemented with 10% (v/v) FBS and 100 units/mL penicillin/streptomycin. Cell proliferation on samples was performed by AlamarBlue™ assay (Invitrogen, USA. 4 samples for each group were used for the AlamarBlue™ test. Synthesized HA powders were used to prepare 300 mg-discs (12.5 mm-diameter, 1 mm-thickness) by applying a force of 22.241 kN (~5000 lbs) with a uniaxial cold press (Carver, USA). HA discs were then sintered at 700, 900 or 1100°C for 2 h. All discs were heated at 200°C for 2 h for sterilization prior to cell culture experiments. Cells were seeded to HA discs at an initial seeding density of $2x10^4$ cells/disc and kept in an incubator containing 5% CO_2 at 37°C for 7 days. The culture medium was renewed every three days. Cell viability on discs was measured at different incubation periods (1, 4 and 7 days) by AlamarBlue™ cell viability test. After removal of the culture medium, phosphate buffered saline (PBS) was used to wash cells once and AlamarBlue™ (Invitrogen, USA) solution (10% AlamarBlue™ reagent in phenol red-free DMEM) was added. At the end of 4h-incubation, the medium in each well was collected. The optical densities were obtained at 570 nm and 600 nm via microplate spectrophotometer (μOuantTM, Biotek Instruments Inc., USA) and recorded (Ternane et al., 2002) using the ELISA software program (Atlanta, USA). Pure HA was used as the control group and cell viability of Saos-2 cells on HA discs was considered as 100% and the relative cell viability of the groups was calculated by normalizing the absorbance readings with

that of pure HA. Relative cell viability calculations were done for each time point (1, 4 and 7 days) and shown graphically. Cytotoxicity test was repeated for 3 times.

2.2.1.4.2 Alkaline Phosphatase (ALP) Activity Test

Alkaline phosphatase (ALP) assay was applied for determining the effect of synthesized materials on the osteogenic activity of cells. Saos-2 cells were seeded on discs at a density of $4x10^4$ cells/disc and incubated in osteogenic differentiation medium (DMEM supplemented with 10% FBS, 1% penicillin streptomycin, 50 μg/ml ascorbic acid, 10 mM β-glycerophosphate and 10^{-8} M dexamethasone), for 7 and 14 days. At the end of each time point, discs were collected and washed with sterile PBS. Then, discs were incubated in fresh 0.6 ml lysis buffer solution (0.1% Triton X-100 having 0.1 % w/v sodium azide and 1% protease inhibitor in sterile PBS, pH 7.4). Three cycles of freezing/thawing were applied and obtained lysates were diluted using osteogenic differentiation medium. 75 μl p-nitrophenyl phosphate (pNPP) substrate solution was mixed with 75 μl of each lysate-medium solution. Then, 25 μl $MgCl_2$ solution was added and incubated at 37°C for 60 minutes in an orbital shaker. During incubation, pNPP is converted into p-nitrophenol as shown below:

p-nitrophenyl ⟶ phosphate p-nitrophenol + phosphate

At the end of incubation period, the absorbance of the mixture was read at 405 nm by a spectrophotometer (μOuantTM, Biotek Instruments Inc., USA). A calibration curve was constructed with different concentrations of p-nitrophenol in the range of 25-250 μM and used for determining the amount of nitrophenol produced by the cells. ALP activity of the cells was normalized to its protein content and expressed as specific ALP activity (nmol/μg protein/min) and the test was repeated 3 times.

Bicinchoninic acid (BCA) assay was used to determine the protein contents of the lysates. For this procedure, by mixing 500 μl of copper sulfate solution with 50 ml of BCA reagent the substrate solution was prepared. 25 μl of the cell lysate was

added into 175 µl of copper sulphate-BCA mixture and following 15 minutes of incubation at 60°C and cooling, the absorbance was read at 562 nm with a µOuantTM microplate spectrophotometer. The total protein amount of the lysate on each disc was determined according to the calibration curve obtained with bovine serum albumin (BSA) in the range of 0-1 mg/mL. Pure and ion-doped HAs without cells served as negative controls.

2.2.2 Synthesis and Characterization of PCL-PEG-PCL

2.2.2.1 Synthesis of PCL-PEG-PCL

PCL-PEG-PCL was synthesized according to the protocol by Pazarçeviren et al., and the experimental setup is shown in Figure 2. Shortly, 0.75 g of poly (ethyl glycol) (PEG) was put in a 3-necked round bottom flask placed in liquid petroleum jelly, and the temperature was brought to 100°C with the help of a heater. The polymer was allowed to melt for 30 minutes. During this process, nitrogen gas was given from a neck of the flask. Then, the temperature was brought to 140°C and 18 g of ε-caprolactone (ε-PCL) polymer and 5 drops of dibutyltin dialurate catalyst were added and it was kept for 24 h. The mixture was then brought to room temperature and then placed in the refrigerator (4°C). After the solid mixture was dissolved with dichloromethane (CH_2Cl_2), it was dropped into cold technical alcohol with a syringe pump. Later, alcohol was evaporated from the mixture in an oven set at 40°C to obtain PCL-PEG-PCL copolymer (Pazarçeviren et al., 2017), stored in a desiccator until use.

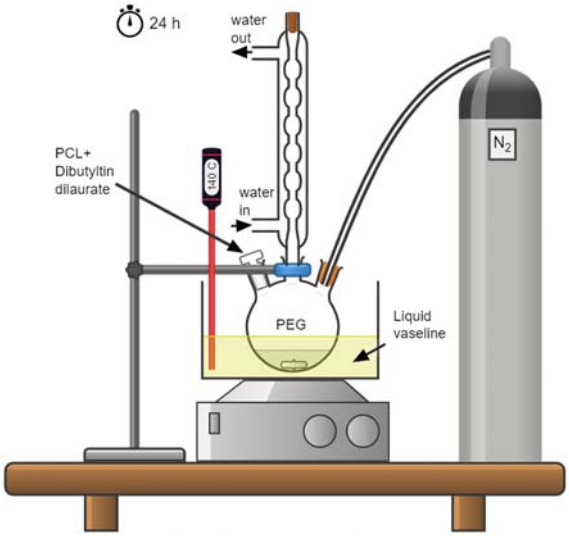

Figure 2. Experimental setup of PCL-PEG-PCL synthesis

2.2.2.2 Fourier Transform Infrared Spectroscopy (FTIR)

FTIR spectra were recorded with a spectrometer (Perkin Elmer 400, Norwalk, CT, USA) from 4000 cm^{-1} to 400 cm^{-1} by carrying out 16 scans to characterize chemical composition of the synthesized PCL-PEG-PCL triblock copolymer.

2.2.2.3 Proton Nuclear Magnetic Resonance (^{1}H NMR) Spectroscopy

The number average molecular weight (Mn) of the synthesized PCL-PEG-PCL triblock copolymer was determined by Nuclear Magnetic Resonance (NMR). The spectrum was obtained with the aid of a liquid spectrometer (Bruker Avance 300 MHz (~7 Tesla)) by dissolving the synthesized PCL-PEG-PCL copolymer with chloroform-d (d-$CDCl_3$). Using the integrity ratio of NMR peaks of methylene protons belonging to PCL and PEG segments at 4.07 ppm and 3.65 ppm, respectively, Mn value, PCL/PEG ratio and the degree of polymerization of the synthesized triblock copolymer were calculated. Equations 8, 9 and 10 were used in calculations (Huang et al., 2003):

$$\overline{PD}_{PEG} = \frac{Mn_{PEG}}{44} \quad (8)$$

$$\overline{PD}_{PCL} = \left(\frac{Mn_{PEG}}{44}\right) \times \frac{[CL]}{[EG]} \quad (9)$$

$$Mn = Mn_{PEG} + 114 \times \overline{PD}_{PCL} \quad (10)$$

In these equations, the molecular weight of ethylene glycol (EG) is 44 (g/mol) while the molecular weight of linearized caprolactone (CL) is 114 (g/mol). PD indicates the degree of polymerization, and it is used to determine Mn of the PCL-PEG-PCL copolymer.

2.2.2.4 Gel Permeation Chromatography (GPC)

Weight average molecular weight of the PCL-PEG-PCL copolymer was determined by using GPC (Agilent 110 HPLC, USA). After dissolving in spectroscopically pure tetrahydrofuran (THF, eluted at a rate of 1.0 mL/min), the sample was stirred on magnetic stirrer for 15h. Both the outside and column temperature were kept at 35°C. Then it was filtered through a 0.2 μm filter and analysed. The results were evaluated using the Triple Detection Method (Manjili et al., 2016).

2.2.3 Production and Characterization of PCL-PEG-PCL/B, Sr, Mg Multi-Doped Hydroxyapatite Composite Scaffolds

2.2.3.1 Production of Composite Scaffolds

Composite and porous scaffolds with PCL-PEG-PCL/B-Sr-Mg doped HA were produced by compression-molding/particulate leaching method (Pazarçeviren et al., 2017). The general look of the scaffolds before leaching is shown in Figure 3.

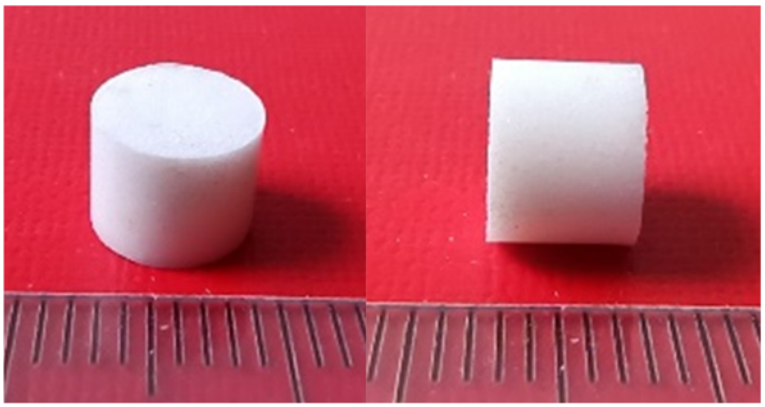

Figure 3. The general outlook of scaffolds before leaching

Briefly, a predetermined amount (Table 5) of PCL-PEG-PCL was pulverized in pure ethanol by stirring at 2000 rpm for 1h (T25 Ultra-Turrax, IKA, China), dried and sieved using a 112 μm sieve together with B-Sr-Mg doped HA and porogen (NaCl). The ingredients were mixed in pure ethanol at 1000 rpm for 10 minutes to obtain a homogeneous mixture. The mixture was dried in an atmospheric oven for 24h to remove ethanol. Then, the powder mixture was compressed unidirectionally under a pressure of 250 MPa for 3 minutes in a steel mold (Carver AutoPellet Press, USA) to obtain scaffolds. Prepared scaffolds were kept in distilled water at 37°C for 2 days in a water bath and porosity was obtained by removing NaCl. As an indicator of NaCl removal from the scaffolds, pH of 7.00 was accepted. dH_2O was renewed at certain time intervals until the pH of dH_2O reached to 7.00.

Table 5. Amount of components used for the preparation of B-Sr-Mg doped HA composite scaffolds

Desired porosity (%)	Scaffolds*	PCL-PEG-PCL (mg)	Pure/doped HA (mg)	Porogen (NaCl) (mg)
50	1:1	100	0	190
	1:1+10% HA	100	10	190
	1:1+20% HA	100	20	190
60	1:1.45	100	0	270
	1:1.45+10% HA	100	10	270
	1:1.45+20% HA	100	20	270

* Scaffolds are grouped according to their porosities and amount of HA inside. While the ratio of PCL-PEG-PCL: NaCl is 1: 1 by volume for 50% porosity, this ratio is 1: 1.45 for 60% porosity. In scaffolds containing HA; 10% by weight and 20% HA of the PCL-PEG-PCL content was used.

2.2.3.2 Determination of Porosity of Scaffolds

Archimedes' Principle was used to measure the experimental porosity of the scaffolds. Simply, it was determined using the dry weight (W_d), and the weight suspended in water (W_s) and wet weight of the scaffold removed from water (W_w). The weight of the samples was measured with a precision scale and porosity ratios were calculated by Equation 11 (Mazón and De Aza, 2018).

$$Porosity\ (\%) = \left(\frac{W_w - W_d}{W_w - W_s}\right) \times 100 \qquad (11)$$

2.2.3.3 Thermogravimetric (TGA) Analysis of Scaffolds

By heating the samples from 30°C to 1100°C at a heating rate of 10 °C/min, the pure and ion-doped HA content of the scaffolds was determined under air atmosphere using TGA (NETZSCH STA 449F3). Pure porous PCL-PEG-PCL scaffolds were used as the control group in all tests.

2.2.3.4 *In Vitro* Degradation and Water Uptake Test

Degradation analysis of pure PCL-PEG-PCL and PCL-PEG-PCL/B-Sr-Mg doped HA scaffolds was carried out, in 14 mL PBS solution (pH 7.4, 0.01 M) at 37°C for 3 weeks (n=4) by using a shaking water bath. After each incubation period, the weight change (%) of the scaffolds was calculated using Equation 12:

$$Weight\ loss\ (\%) = \left(\frac{M_i - M_f}{M_i}\right) \times 100 \qquad (12)$$

In the equation, initial and final weight of the scaffolds at different incubation periods are presented with M_i and M_f, respectively.

The water uptake behaviour of the scaffolds at certain time periods was studied by incubating them in 15 mL of PBS solution (n=3). By using a filter paper excess water on the scaffolds was removed before weighing the wet scaffolds, then wet weights of the scaffolds were determined for each incubation period. Water uptake (%) of the scaffolds was calculated with Equation 13 where W_i represents the initial dry weight and W_w represents the wet weight of the scaffold at the given incubation period:

$$Water\ uptake\ (\%) = \left(\frac{W_w - W_i}{W_i}\right) \times 100 \qquad (13)$$

2.2.3.5 *In Vitro* Bioactivity Analysis

The scaffolds were incubated in simulated body fluid (SBF, pH 7.4) which was prepared by the Kokubo's method (Kokubo and Takadama, 2006) to perform bioactivity analysis. The scaffolds were placed in smooth polypropylene containers containing SBF and kept at 37°C (n=5) for 3, 7 and 14 days. SBF solution was renewed every 2 days. For each incubation period, after immediate rinsing with dH_2O, the scaffolds were dried for 24h until there was no moisture left in. SEM analysis was used to examine the mineralization on the scaffolds. Ca and P peak intensities obtained from EDS spectra was used to determine Ca/P ratio. The pH of the solution at each incubation period was measured using a pH meter (S20 SevenEasy ™ pH).

2.2.3.6 Compression Test

The compressive strength of PCL-PEG-PCL/B-Sr-Mg doped HA scaffolds was determined with a universal tester (Instron 5944, USA, TOBB-ETU). Using a static compression load of 5000-N and a head speed of 0.1mm/sec, scaffolds of 7×3 mm^2 were compressed by placing between two parallel plates until 10% strain was obtained. The data were recorded using the test device's own software. The compressive strength and compressive moduli of the samples were obtained from the peak point of the stress-strain curve.

2.2.3.7 Cell Culture Studies

Human bone osteosarcoma (Saos-2) cells were grown in DMEM enriched with 10% FBS and 100 units/mL penicillin/streptomycin at 37°C in a carbon dioxide incubator (5% CO_2, 5215 Shel Lab., Cornelius, OR, USA) for cell culture studies. Cells were subcultured when they reached 80% confluency using 0.1% Trypsin/EDTA solution. In the experiments, cells at 4^{th} passage was used. To sterilize the scaffolds, incubation

in 70% ethanol for 2h followed by irradiation with UV for 30 minutes on each side was applied.

2.2.3.7.1 Alamar Blue™ Cell Viability Test

Saos-2 cells were seeded on the surface of pure PCL-PEG-PCL and PCL-PEG-PCL/B-Sr-Mg doped HA scaffolds at a density of $2x10^4$ cells/scaffold and incubated at 37°C for 7 days in a carbon dioxide incubator (Shell Lab, USA). Cell viability on scaffolds at different incubation periods (days 1, 4 and 7) was measured by the AlamarBlue™ viability test. The culture media were renewed every 3 days. After withdrawal of the culture medium, the scaffolds with cells were washed with PBS and AlamarBlue™ solution (10% Alamar Blue™ reagent in DMEM without phenol red) was added. Media in each well were collected after 4h of incubation, and absorbance measurements at 570 and 600 nm were made with a microplate reader (Module 9200, Turner Biosystem, USA). After media removal, the cells were washed once with PBS and fresh media were added to continue cultivation. Cell viability (%) was calculated by Equation 14.

$$\frac{(O_2 \times A_1) - (O_1 \times A_2)}{(O_2 \times P_1)(O_1 \times P_2)} \times 100 \quad (14)$$

In this equation, O_1 and O_2 represent the molar extinction coefficient (E) of the oxidized Alamar Blue at 570 and 600 nm; A_1 and A_2 are the absorbance of the test wells at 570 and 600 nm; P_1 and P_2 refer to the absorbance of the control wells at 570 and 600 nm, respectively. Relative cell viability at each time point was calculated using Equation 15 in which the viability of the control group was considered to be 100%.

$$\text{Relative cell viability (\%)} = \frac{\text{Viability}_{Test}}{\text{Viability}_{Control}} \times 100 \quad (15)$$

2.2.3.7.2 Osteogenic Activity of Cells

To study the osteogenic activity of Saos-2 cells on scaffolds, specific ALP activity (n = 4) and intracellular calcium amount (n = 4) of the cells were measured. Scaffolds without cells served as the negative control. $4x10^4$ cells were seeded on each scaffold and osteogenic differentiation medium (DMEM containing 10% FBS, 1% penicillin-streptomycin, 50 µg/mL ascorbic acid, 10 mM β-glycerophosphate, and 10^{-8} M dexamethasone) was used for incubation of the scaffolds for 14 days. The cells were lysed with cycles of freezing and thawing in 300 µL PBS containing 0.1% Triton X-100, 0.1% v/w sodium azide and 1% protease inhibitor, and cell lysates were obtained on days 7 and 14. Freeze and thaw cycles were repeated 3 times. Lysate (75 µL) and p-nitrophenylphosphate (pNPP, 75 µL) substrate solution were mixed and 25 µL $MgCl_2$ was added. The mixture was then incubated at 37°C for 60 minutes. Subsequently, the absorbance was read at 405 nm with a microplate spectrophotometer (µQuant MQX200, Biotek, USA). Using different concentrations (0-250 µM) of p-nitrophenol, a calibration curve was constructed and used to determine the amount of p-nitrophenol produced. The ALP activity was normalized by the protein content to determine specific ALP activity of cells. The total amount of protein in the lysates was measured by the BCA method (Lozzi et al., 2008). Briefly, working reagent solution was prepared by mixing 1 mL of Cu_2SO_4 solution (2 g of cupric sulphate in 50 mL of water) and 50 mL of bicinchoninic acid solution. Then, 25 µL of cell lysate and 175 µL of working solution were incubated at 60°C for 15 minutes. The absorbance of the samples was measured with a microplate spectrophotometer at 562 nm (µQuant MQX200, Biotek, USA). Using a calibration curve with known concentrations of bovine serum albumin (BSA) (0 - 1.2 mg/mL) total protein amount was determined.

The amount of intracellular calcium was determined by the o-cresoptalein test using cell lysates (Nuttelman et al., 2005). 10 µL of the cell lysates was incubated overnight in 0.1 M HCl. 200 µL of o- cresoptalein and 8-hydroxyquinone-5-sulfonic acid in 2-amino-2-methyl-1,3 propanediol was mixed with the resulting solution to complex

with intracellular calcium. The absorbance was measured at 560 nm with a microplate reader. The calibration curve was obtained with different concentrations of $CaCl_2$ solution (0–200 μ/mL) and the amount of intracellular calcium was determined and normalized by protein content (BCA) of the cell lysates, as described above.

2.2.4 Statistical Analysis

SPSS software (ver. 26.0; IBM Corporation, NY, USA) was used for statistical analysis of the data. Multiple comparisons were done with one-way analysis of variance (ANOVA) with Tukey Post Hoc test. Results are shown as mean ± standard deviation (SD).

CHAPTER 3

RESULTS AND DISCUSSION

3.1 Characterization of B, Sr and Mg Multi-Doped Hydroxyapatite

3.1.1 Structural Characterization

3.1.1.1 X-Ray Diffraction Analysis

XRD patterns of the samples sintered at 700, 900 and 1100°C for 2h are shown in Figure 4. According to these patterns, HA, 0.5BHA and 2Sr0.5BHA groups sintered at 700 and 900°C showed pure HA pattern, while the other groups showed both β-TCP and HA patterns when compared to standard HA (JCPDS♯: 9-432) and β-TCP (JCPDS♯: 9-0169). It was also found that an increase in dopant amount caused biphasic structure. Phases in the samples calculated by XRD patterns according to Farzadi et al. (2011) are listed in Table 6.

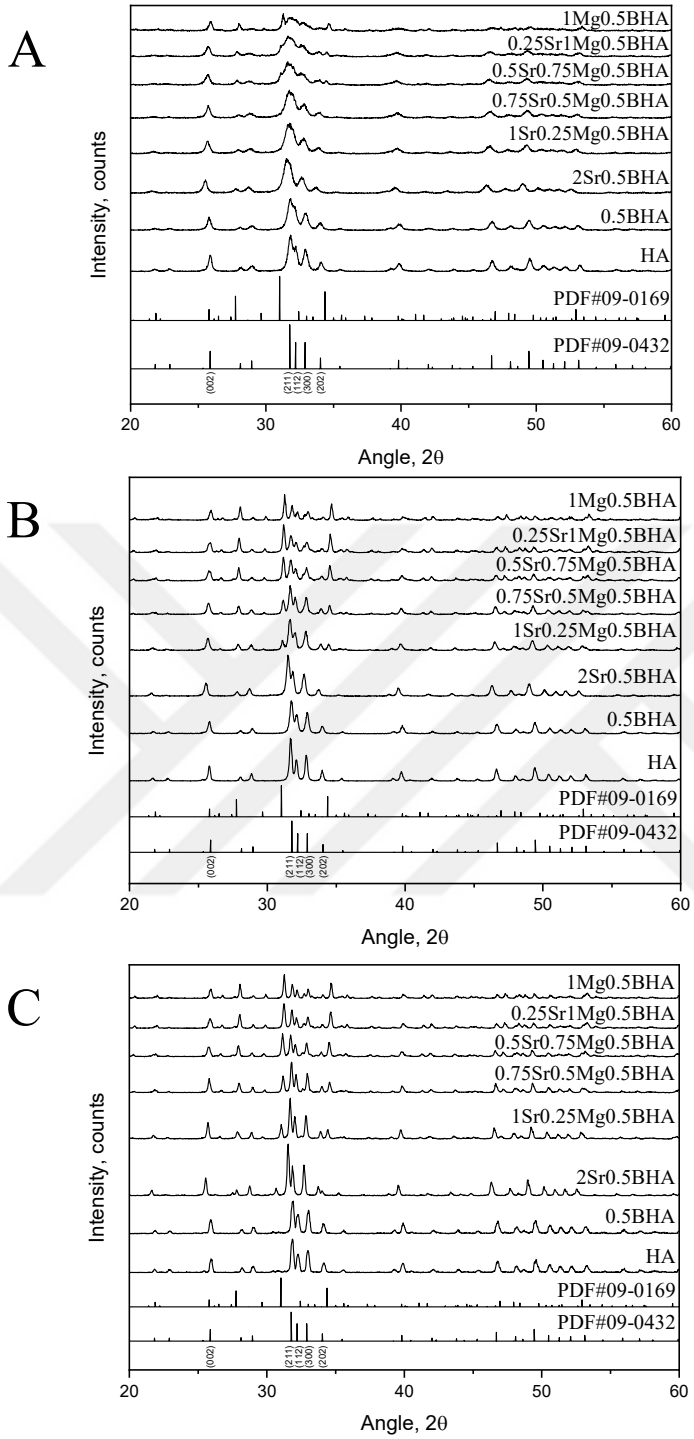

Figure 4. XRD patterns of the samples sintered at A) 700°C, B) 900°C and C) 1100°C. Vertical solid lines indicate the peaks of standard HA (PDF#09-0432) and dash lines β-TCP (PDF#09-0169).

As shown in Table 6, the β-TCP phase gradually increased as the Mg amount was increased. Mg was reported to have an inhibitory effect on the crystallization of HA and its presence increases the formation of β-TCP phase (Tampieri et al., 2004; Yılmaz and Evis, 2016). Veljovic et al. reported that the concentration limit of Mg ions in the precursor solution is 15 mol% for the apatite phase to disappear completely and the formation of monophasic β-TCP in unsintered samples (Veljovic et al., 2019). Previous studies reported that Sr can also cause biphasic structures to form (Kaygılı et al., 2015). HA was previously reported to remain as the main phase when 5 mol% Sr was substituted and sintering temperature was 1000°C, but when the Sr content was increased to 15 mol%, the mass fraction of β-TCP was higher than 80% (He et al., 2016). In a study on Sr and Mg co-doped into HA, the characteristic peaks of HA and β-TCP phases were observed in XRD patterns with the combined effect of Mg^{2+} and Sr^{2+} ions (Aina et al., 2012). In this thesis, according to XRD patterns, the effect on HA structure was mostly affected by the presence of Mg. Hayakawa et al. reported that thermal decomposition of HA to β-TCP was obtained for the B-doped HAs sintered above 700°C. Above 900°C, both HA and β-TCP phases were obtained with the formation of BHA particles (Hayakawa et al., 2007). B substitution was previously shown to result in the formation of β-TCP phase whose ratio ranges between 30.3% to 37.8% after being sintered between 1000-1200°C when the amount of B was 2 wt.% in the synthesis solution (Albayrak, 2016). In this thesis, no other phases or impurities were detected in the samples of B introduced HAs, there was only HA phase. Only reduction in the peak intensities was observed with the B doping.

Table 6. Amount of phases in the multi doped HAs after the XRD analysis calculated by the relative intensity ratio (RIR).

Sample	Phase Percent (%)					
	700°C		900°C		1100°C	
	HA	β-TCP	HA	β-TCP	HA	β-TCP
HA	100	0	100	0	95.6	4.4
0.5BHA	100	0	100	0	96.5	3.5
2Sr0.5BHA	100	0	100	0	95	5
1Sr0.25Mg0.5BHA	96.2	3.8	76.6	23.4	75.2	24.8
0.75Sr0.5Mg0.5BHA	88.2	11.8	65.3	34.7	65.2	34.8
0.5Sr0.75Mg0.5BHA	65	35	47	53	48.5	51.5
0.25Sr1Mg0.5BHA	63.3	36.7	37.5	62.5	42	58
1Mg0.5BHA	45.5	54.5	36.1	63.9	36.4	63.6

Amount of phases in the samples changed along with different sintering temperatures. When HA, 0.5BHA and 2Sr0.5BHA samples were sintered at 700 and 900°C, they had pure HA phase, biphasic (β-TCP and HA) phase was formed when sintered at 1100°C. As sintering temperature was increased from 700°C to 900°C, a considerable increase was observed in the amount of β-TCP phase for the Mg-containing samples. There was no major difference in phase quantities between the Mg-containing samples sintered at 900°C and 1100°C.

In XRD patterns of pure and doped HAs, as the sintering temperature was increased, the XRD peaks became narrower. This showed that the crystallinity of the samples gradually increased with increasing sintering temperature (Toledano-Osorio et al., 2020). The degree of crystallinity of the samples is presented in Table 7. The highest crystallinity for all specimens was obtained in specimens sintered at 1100°C as the XRD pattern was dense and narrow. In a study of Mg-doped HA, owing to the reduction in the crystallite size and increase in the lattice disorder peak broadening was found with the Mg^{2+} doping in the HA lattice (Ziani et al., 2014). In this thesis,

similar results were obtained for the Mg^{2+} doped samples which were sintered at 700°C and as the amount of Mg doping became higher (from 0.25% to 1% mole) peak broadening increased. On the other hand, for Mg-doped groups sintered at 900°C and 1100°C peak broadening was lower when compared to doped-HAs sintered at 700°C. When 2Sr0.5BHA was compared to pure HA, for the sintering temperatures of 700 and 900°C a small drop in the crystallinity was ascertained with the Sr doping. However, a small increase was obtained for the 2Sr0.5BHA group sintered at 1100°C. In the study of Kavitha et al., Sr doping caused peak broadening (Kavitha et al., 2014). B doping also decreased the degree of crystallinity and caused peak broadening when compared to pure HA. These results were in agreement with the literature (Geng et al., 2016; Kolmas et al., 2017).

XRD patterns of pure and multi-doped HAs exhibited well-defined peaks. However, the peak corresponding to the (211) plane of B-Sr and Mg multi-doped HA samples sintered at 700 and 1100°C shifted to slightly lower 2θ values compared to the standard HA. This shift may be due to the ionic radius differences between Sr^{2+} and Mg^{2+} which are replaced with Ca^{2+} (ionic radii of Ca^{2+}=1.00Å, Mg^{2+}=0.72Å and Sr^{2+}=1.18Å) and BO_3^{3-} with PO_4^{3-} (ionic radii of PO_4^{3-}=2.38Å and BO_3^{3-}=1.91Å) (Barheine et al., 2011; Bigi et al., 2007; Hakkı et al., 2010; Suchanek et al., 2004). The replacement of larger sized Ca^{2+} ions with smaller sized ions like Mg^{2+} and Zn^{2+} line resulted in shifting to the higher 2θ values (Dasgupta et al., 2010; Evis and Webster, 2011). However, the doping of Sr^{2+} and Ag^{+} -ions having higher ionic radii than Ca^{2+}- can cause an increase in the lattice parameters, which resulted in line shifting to lower 2θ values (Geng et al., 2016). Lattice parameters of the samples are provided in Table 8. With B doping into HA, the lattice parameter *a* decreased, while *c* increased with the increasing B amount (Barheine et al., 2011). As expected from the literature that lattice parameters increased with the doping of Sr and decreased with the doping of Mg due to ionic radius differences between Ca^{2+} and Sr^{2+} or Mg^{2+}, respectively. (Kheradmandfard and Fathi, 2013; O'Donnell et al., 2008).

Table 7. Degree of crystallinity of the multi doped HAs calculated from the XRD analysis.

Sample	Degree of Crystallinity (%)		
	700°C	900°C	1100°C
HA	70.5	94.0	97.0
0.5BHA	67.0	89.0	96.2
2Sr0.5BHA	65.8	91.3	98.2
1Sr0.25Mg0.5BHA	48.4	84.4	87.5
0.75Sr0.5Mg0.5BHA	44.6	75.9	87.0
0.5Sr0.75Mg0.5BHA	49.2	73.2	84.3
0.25Sr1Mg0.5BHA	47.2	76.1	83.5
1Mg0.5BHA	18.7	73.6	85.3

In Mg, Sr and B multi-doped samples, a leftward shift was observed, especially in samples where the amount of doped Sr was more than that of Mg and B. This left shifting in Mg, Sr and B multi-doped samples could be attributed to the lattice expansion due to doping compared to pure HA. Sr may push the Ca atoms away at a slightly longer distance, which may lead to local distortions (Terra et al., 2009). Consequently, larger lattice parameters of the Sr-doped HA were obtained. The shifting also means that substitution of the ions was successful.

There are mainly two factors that determine the likelihood of a lattice structure to accommodate different ions; (1) the size of the substituent ion (2) the ability of the structure to tolerate a certain degree of distortion (Bigi et al., 2016). According to Goldschmidt Rules, replacement of an ion in a crystal is expected when there is an ionic radius difference of less than 15%. When the ions have similar radii but different valence charges, substitution of one element for another preferably occurs where charges vary by no more than ±1. If there is charge imbalance due to the ionic substitution, a charge compensating ion is required, for example CO_3^{2-} for PO_4^{3-} coupled to Na^+ for Ca^{2+} in HA. When the above criteria are met, the substitution can still be limited by the poor flexibility of the structure and electronegativity difference of the competing ions forming bonds of different ionic character (Giacovazzo et al.,

2013). HA's flexible structure is open to great variety of cationic and anionic substitutions that can be controlled by ionic radii differences and charge factors.

Table 8. Lattice parameters of the samples.

Sample	Sintering Temperature					
	700°C		900°C		1100°C	
	a-Axis (Å)	c-Axis (Å)	a-Axis (Å)	c-Axis (Å)	a-Axis (Å)	c-Axis (Å)
HA	9.411	6.878	9.433	6.888	9.410	6.871
0.5BHA	9.399	6.884	9.420	6.891	9.405	6.874
2Sr0.5BHA	9.436	6.887	9.435	6.894	9.425	6.876
1Sr0.25Mg0.5BHA	9.431	6.882	9.429	6.893	9.422	6.875
0.75Sr0.5Mg0.5BHA	9.428	6.881	9.424	6.891	9.420	6.874
0.5Sr0.75Mg0.5BHA	9.423	6.882	9.421	6.892	9.419	6.873
0.25Sr1Mg0.5BHA	9.420	6.880	9.419	6.891	9.418	6.874
1Mg0.5BHA	9.409	6.879	9.414	6.892	9.404	6.874

The ionic radii difference between Ca^{2+} or PO_4^{3-} and dopants was calculated as -28%, +18% and -19.75% for Mg^{2+}, Sr^{2+} and BO_3^{3-} ions, respectively. Even if Mg^{2+} has higher electronegativity (1.31 by Pauling scale) than Sr^{2+}, due to having less ionic radii difference, Sr^{2+} can be expected to have more chance of doping into the HA structure. It was previously reported that larger ions than Ca^{2+} can be completely doped for calcium sites in HA (Famery et al., 1994). Moreover, Mg^{2+} ions are mainly adsorbed onto the HA crystalline surface. Therefore, there are much more Mg^{2+} ions on the surface of HA than in the structure of HA (Kalita and Bhatt, 2007; Kim, 2003). When it comes to comparing Ca^{2+} dopants and BO_3^{3-}, although B has higher electronegativity (2.051 by Pauling scale) than the others, ionic radius difference is

between the two. Therefore, it is expected to have chance of doping more than Mg^{2+} and less than Sr^{2+} into HA structure.

3.1.1.2 Fourier Transform Infrared Spectroscopy (FTIR)

FTIR spectra of the samples sintered at 700, 900 and 1100°C for 2h taken in 4000–400 cm^{-1} region are presented in Figure 5. In FTIR spectra, the stretching band at 3572 cm^{-1} originating from the OH^- stretching mode in HA phase was observed in all samples. The characteristic vibration band at 630 cm^{-1} of OH^- ions which proves the presence of HA, began to disappear as the ratio of the additive ion in HA increased as x+z or y+z being greater than or equal to 1 for $Ca_{10-x-y}Mg_xSr_y(PO_4)_{6-z}(BO_3)_z(OH)_2$. It can therefore be assumed that the transition to the β-TCP phase has begun as also seen in XRD analysis.

The weak peak at 1251cm^{-1} was assigned to ν_3 (BO_3) (Ternane et al., 2002), and observed in all B-doped groups. The intensity of this peak was higher for 0.5BHA group, when Sr and Mg were introduced while the intensity of the band decreased. Ion-doped HA powders exhibited wider bands compared to pure HA. The obtained FTIR spectra confirmed the formation of the doped HA particles (Alshemary et al., 2013). Intensities of the bands observed at 3572 cm^{-1} and 633 cm^{-1} were higher for HA. However, when the doping amount was increased above where x+z or y+z was greater than 1 for $Ca_{10-x-y}Mg_xSr_y(PO_4)_{6-z}(BO_3)_z(OH)_2$, intensities at 3572 cm^{-1} and 633 cm^{-1} bands started to decrease (Tõnsuaadu et al., 2012). Frasnelli et al. reported that at higher Sr content (5mol% and 7.5mol%), stretching band at 3572 cm^{-1} and 633 cm^{-1} gradually vanished (Frasnelli et al., 2017). Likewise, in a study that investigated the ion concentration and calcination temperature on the phase behavior of Sr doped HAs, OH^- bands at 550 cm^{-1}–650 cm^{-1} disappeared gradually as Sr concentration was increased (Mardziah et al., 2009). Since Sr^{2+} has a higher ionic radius than Ca^{2+}, the deformation in the cell was also increased as the amount of Sr^{2+} was increased. Therefore, a reduction in the intensity of these peaks occurred.

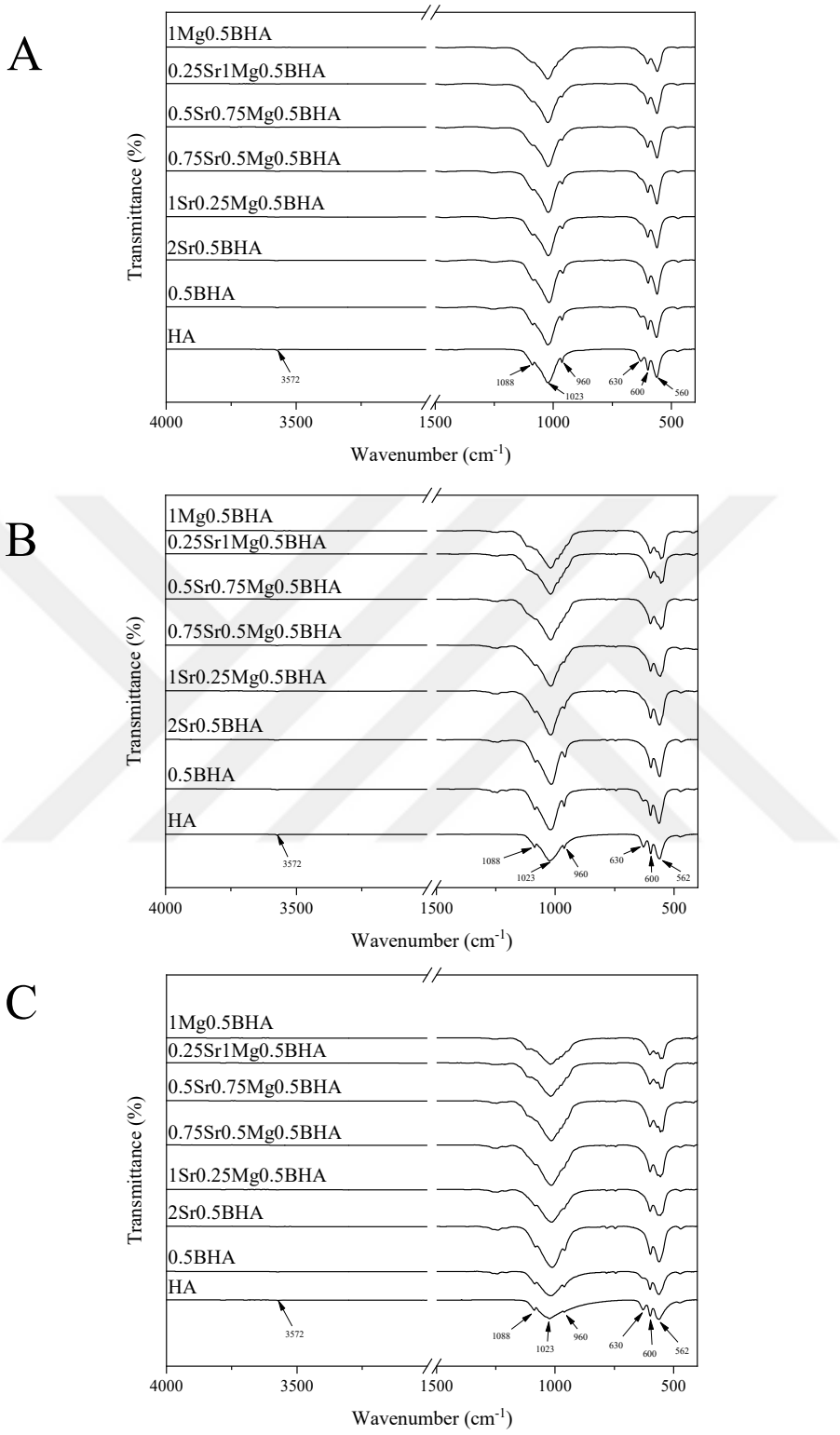

Figure 5. FTIR spectra of the samples sintered at A) 700°C, B) 900°C and C) 1100°C.

Five bands located at 562 (ν_4), 600 (ν_4), 1023 (ν_3), 1088 (ν_3), 960 cm^{-1} (ν_1) were attributed to the PO_4^{3-} group (Berzina-Cimdina and Borodajenko, 2012). The intensity and sharpness of the bands at 562, 600, 1023, 1088, 960 cm^{-1} increased as the amount of Sr^{2+} ion was increased. In other studies, the peak attributed to phosphate group in the FTIR spectra of the co-doped samples shifted to lower wavenumbers as the amount of Sr^{2+} ion was increased (Bigi et al., 2007). Similarly, in this thesis, this peak (at 562 cm^{-1}) shifted towards a lower wavenumber due to substitutional strain in the lattice (Ehret et al., 2017).

3.1.1.3 Thermogravimetric Analysis (TGA)

TGA analysis of the samples was performed by heating samples from 10°C to 1100°C with a rate of 20°C/min in a nitrogen atmosphere (Figure 6). A small amount of weight loss observed between 40 and 200°C might be due to the evaporation of adsorbed and structurally incorporated water (Gopi et al., 2014a). There was no sudden weight loss and steep slope that could be attributed to the decomposition of HA in the thermogram (Popa et al., 2015). No peaks referring to the transformation of HA to TCP were present as reported in other studies using air since there was no water in the pure nitrogen atmosphere (Liao et al., 1999). For the B-doped HA, a small amount of weight loss (almost 1%) occurred. However, in the study of Atila et al. (2019), the thermal stability of B-doped HA was found higher than that of HA, and the weight loss of BHA samples was also 0.81% while for HA loss was 1.89% (Atila et al., 2019). The maximum weight loss was obtained in 1Mg0.5BHA group probably due to having higher water-absorbing capacity (Kulanthaivel et al., 2015). Also, for the other groups, when the Mg amount was higher than x=0.5 ($Ca_{10-x-y}Mg_xSr_y(PO_4)_{6-z}(BO_3)_z(OH)_2$), the slope was higher for 100°C-400°C. It can be said that the presence of Sr, reduces the weight loss of the samples. For all samples there was no significant weight loss between 550°C and 1100°C, indicating that only the mineral phase (CaP) was left above 550°C.

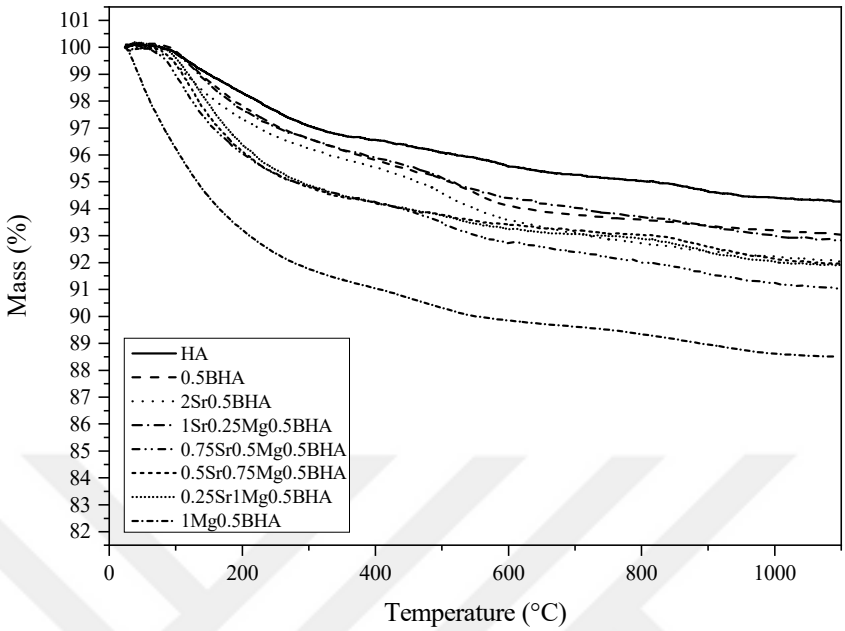

Figure 6. Thermal gravimetric analysis (TGA) curves displaying the mass loss of pure and doped HA samples.

3.1.1.4 Inductively Coupled Plasma-Mass Spectrometry (ICP-MS)

The chemical composition of B, Sr and Mg multi-doped HA powders was obtained from ICP-MS analysis (Table 9). ICP analysis confirmed the presence of Sr, Mg and B in the powders. Ca/P ratio is an important parameter that determines the properties of calcium phosphates. HA sintered between 1000°C and 1150°C with a stoichiometric Ca/P ratio of 1.67 had higher mechanical properties than non-stoichiometric HA (Ramesh et al., 2007). Phase stability of HA was conserved during the sintering regime of samples with a Ca/P ratio of 1.67. However, secondary phases were observed in the samples sintered at higher temperatures and Ca/P ratio was higher than 1.67 (calcium-rich) (Ramesh et al., 2007). For all multi-doped HA samples synthesized in this thesis except 1Mg0.5BHA, the molar ratio (Ca+Sr+Mg)/(P+B) ranged between 1.76 and 1.91 while Ca/P ratio was higher than the theoretical one: $1.73 < Ca/P < 1.91$ confirming that they were Ca-rich HA. In a

study, CaO phase was detected in calcium-rich HA (Ca/P = 1.87) which were sintered at 1300°C (Tan et al., 2015). In this thesis, only for the samples containing 0.5-1 mol% Mg sintered at 900 and 1100°C, there were small peaks matching with CaO in XRD patterns due to decomposition of HA phase.

Sintering is another parameter that affects the structure of ion-doped HA. It is stated in the literature that there may be a deviation in Ca/P ratio of stoichiometric HA with an increase in sintering temperature (Evis and Webster, 2011). Although stoichiometric HA could not be obtained in this thesis and fluctuations in Ca/P ratio occurred with the different sintering temperatures. For Sr, Mg, B multi doped-HAs, Ca/P ratio increased when the sintering temperature was increased from 700 to 900°C. Both the amounts of Ca and P increased with an increase in sintering temperature while oxygen amounts decreased. The increase in Ca was much greater than that of P (Pattanayak et al., 2007) when the sintering temperature was elevated. Therefore, it might have resulted an increase in Ca/P ratio. Loss of oxygen in the form of hydroxyl group and moisture could be the reason for that. However, there was a decrease when the temperature was increased from 900 to 1100°C for the same groups.

Table 9. ICP-MS analysis of the multi-doped HA samples sintered at different temperatures.

Sample	Sintering Temperature	Ca (mol x 10^{-3}/L)	P (mol x 10^{-3}/L)	B (mol x 10^{-3}/L)	Mg (mol x 10^{-3}/L)	Sr (mol x 10^{-3}/L)
HA	700°C	8.41 (10)	4.40 (6)	0.00 (0)	0.00 (0)	0.00 (0)
0.5BHA		7.81 (10)	3.91 (5.5)	0.35 (0.5)	0.00 (0)	0.00 (0)
2Sr0.5BHA		5.79 (8)	3.42 (5.5)	0.30 (0.5)	0.00 (0)	1.16 (2)
1Sr0.25Mg0.5BHA		7.29 (8.75)	4.04 (5.5)	0.35 (0.5)	0.19 (0.25)	0.65 (1)
0.75Sr0.5Mg0.5BHA		7.53 (8.75)	4.36 (5.5)	0.32 (0.5)	0.52 (0.5)	0.34 (0.75)
0.5Sr0.75Mg0.5BHA		7.41 (8.75)	4.26 (5.5)	0.33 (0.5)	0.34 (0.75)	0.47 (0.5)
0.25Sr1Mg0.5BHA		7.53 (8.75)	4.26 (5.5)	0.31 (0.5)	0.59 (1)	0.16 (0.25)
1Mg0.5BHA		11.40 (9)	8.98 (5.5)	0.19 (0.5)	0.81 (1)	0.00 (0)
HA	900°C	8.18 (10)	4.23 (6)	0.00 (0)	0.00 (0)	0.00 (0)
0.5BHA		6.94 (10)	3.39 (5.5)	0.11 (0.5)	0.00 (0)	0.00 (0)
2Sr0.5BHA		5.54 (8)	3.36 (5.5)	0.29 (0.5)	0.00 (0)	1.12 (2)
1Sr0.25Mg0.5BHA		6.81 (8.75)	3.91 (5.5)	0.34 (0.5)	0.17 (0.25)	0.61 (1)
0.75Sr0.5Mg0.5BHA		7.16 (8.75)	4.00 (5.5)	0.32 (0.5)	0.33 (0.5)	0.45 (0.75)
0.5Sr0.75Mg0.5BHA		7.14 (8.75)	4.00 (5.5)	0.30 (0.5)	0.49 (0.75)	0.03 (0.5)
0.25Sr1Mg0.5BHA		7.14 (8.75)	3.97 (5.5)	0.29 (0.5)	0.57 (1)	0.15 (0.25)
1Mg0.5BHA		12.00 (9)	9.59 (5.5)	0.20 (0.5)	0.87 (1)	0.00 (0)
HA	1100°C	7.01 (10)	3.71 (6)	0.00 (0)	0.00 (0)	0.00 (0)
0.5BHA		5.11 (10)	2.49 (5.5)	0.26 (0.5)	0.00 (0)	0.00 (0)
2Sr0.5BHA		4.79 (8)	2.87 (5.5)	0.28 (0.5)	0.00 (0)	0.95 (2)
1Sr0.25Mg0.5BHA		4.22 (8.75)	2.32 (5.5)	0.22 (0.5)	0.10 (0.25)	0.37 (1)
0.75Sr0.5Mg0.5BHA		6.11 (8.75)	3.55 (5.5)	0.28 (0.5)	0.28 (0.5)	0.39 (0.75)
0.5Sr0.75Mg0.5BHA		5.09 (8.75)	2.94 (5.5)	0.27 (0.5)	0.35 (0.75)	0.23 (0.5)
0.25Sr1Mg0.5BHA		6.79 (8.75)	3.81 (5.5)	0.30 (0.5)	0.55 (1)	0.14 (0.25)
1Mg0.5BHA		14.00 (9)	11.00 (5.5)	0.28 (0.5)	1.04 (1)	0.00 (0)

*Theoretical values were given in the parentheses.

3.1.1.5 Density Measurements

Densities of the samples sintered at 700, 900 and 1100°C for 2h were measured using 5 identical discs for each group to determine the effects of the ion content and sintering temperature. Average and relative densities are given in Table 10. Relative densities of sintered HAs at 700°C were higher than 82%. Although there was biphasic structure in some samples (Table 6), obtaining relative density higher than 82% can be interpreted as a successful densification. A significant difference was observed between the densities of control group (HA) and the groups of 2Sr0.5BHA, 1Sr0.25Mg0.5BHA, 0.75Sr0.5Mg0.5BHA, 0.25Sr1Mg0.5BHA, 1Mg0.5BHA which were sintered at 700°C. The densest sample was 2Sr0.5BHA sintered at 700°C, while pure HA sintered at 700°C had the lowest sample density with a relative density of 82.1%. However, having 82.1% relative density can still be accepted as a high density.

Average densities of HA, 0.5BHA, 2Sr0.5BHA and 1Mg0.5BHA were statistically different ($p<0.01$) when they were sintered either 700 or 900°C. A significant increase was ascertained between BHAs sintered at 900°C and 1100°C ($p<0.01$), 0.75Sr0.5Mg0.5BHAs sintered at 700-1100°C ($p<0.05$), 0.5Sr0.75Mg0.5BHAs sintered at 700-900°C ($p<0.05$) and 0.25Sr1Mg0.5BHAs sintered at 700-900°C ($p<0.05$) and 900-1100°C ($p<0.05$). This confirmed previous findings that as sintering temperature increased, the density of the sample also increased (Herliansyah et al., 2009; Muralithran and Ramesh, 2000; Wang and Chaki, 1993).

Table 10. The effect of sintering temperature and ion-doping on average and relative densities of the samples (n = 10, mean ± standard deviation).

Sample	Average density (g/cm^3)			Relative Density (%)		
	Sintering temperature			Sintering Temperature		
	700˚C	900˚C	1100˚C	700°C	900°C	1100°C
HA	$2.59\pm0.08^{*,\Phi}$	$3.01\pm0.07^{*}$	$3.07\pm0.12^{\bullet,\Phi}$	82.1±1.22	95.4±0.67	97.3±0.53
0.5BHA	$2.62\pm0.12^{\Psi,**}$	$2.94\pm0.11^{\Psi,+}$	$3.03\pm0.16^{**,+}$	83±0.80	93.2±0.56	96±0.91
2Sr 0.5BHA	$3.20\pm0.17^{\#,\Omega,++}$	$2.99\pm0.09^{\Omega}$	$3.01\pm0.14^{++}$	100±1.01	94.7±0.74	99.5±0.86
1Sr 0.25Mg 0.5BHA	$2.74\pm0.08^{\#}$	2.92±0.21	2.94±0.23	86.8±0.72	92.5±0.71	92.5±1.02
0.75Sr 0.5Mg 0.5BHA	$2.66\pm.014^{\#,¥}$	2.86±0.23	$2.92\pm0.06^{¥}$	84.3±0.62	90.6±0.51	97.6±0.36
0.5Sr 0.75Mg 0.5BHA	$2.91\pm0.08^{¤,Ø}$	2.96 ± 0.15^{Ø}	$3.08\pm0.16^{¤}$	92.2±0.74	93.8±1.04	96.6±0.74
0.25Sr 1Mg 0.5BHA	$2.88\pm0.03^{\#,£,\lambda}$	$2.95\pm0.16^{£}$	$3.05\pm0.28^{\bullet,\lambda}$	91.6±0.92	93.5±1.10	95.4±0.61
1Mg 0.5BHA	$2.80\pm0.23^{\#,‡,¢}$	$3.06\pm0.15^{‡}$	$3.14\pm0.13^{¢}$	88.7±1.24	97±0.87	93.2±0.52

Number sign (#) indicates that there is a significant difference ($p<0.01$) between the sample and control (pure HA) group sintered at 700°C, while ● shows statistical difference between the group and pure HA group sintered at 1100°C. *, Φ, Ψ, **, +, Ω, ++, ¥, ¤, Ø, £, λ, ‡, ¢ show significant difference for the same group sintered at different temperatures at $p<0.05$.

The density of the samples sintered at 900°C increased up to 90% of the theoretical density of HA. However, no significant difference was observed between the densities of pure and doped HAs sintered at 900°C. The relative densities of HAs sintered at 1100°C were above 92.5%. After this sintering temperature (at 1100°C), the highest densities among all HAs were obtained. Ion contributions to pure HA did not cause significant fluctuations in relative densities. Only for 0.25Sr1Mg0.5BHA, density was significantly different than pure HA (control). In this thesis, the use of microwave irradiation method in the synthesis of HAs was important in obtaining high relative densities. In literature, 95% condensed samples were obtained by exposure to microwave irradiation for 5 minutes, and when the duration was increased to 15 minutes 98% relative density was obtained (Vijayan and Varma, 2002).

In a study, the density increased with the increase in sintering temperature and decreased with the increase in the amount of B used in the synthesis step. For B doped HAs, when the sintering temperature was increased from 1000°C to 1200°C, very high increase was observed in the density (Albayrak and Uğurlu, 2016). In another study, the densities of B-doped HA obtained using 0%, 1.25%, 2.5%, 3.75% and 5 mol% B_2O_3 were found to be between 2.8 g/cm^3 and 2.9 g/cm^3, and as the amount of B_2O_3 increased, the density of HA increased (Massera et al., 2015). In this thesis, relative densities of B-doped HAs ranged from 83% to 96% which was in agreement with the literature.

In a study, the density of HA containing different amounts of Sr, sintered at 1200°C with both conventional and microwave sintering was investigated. 5% Sr-doped HA, sintered by microwave sintering reached a relative density of 96%. In HA with 10% Sr, the relative density reached approximately 98%. Relative densities of the samples sintered with conventional sintering increased from 90% to 96% in HAs with 5% and 10% Sr, respectively. Microwave sintering has a positive effect on the density of samples (Curran et al., 2011). In this thesis, HAs were synthesized by microwave irradiation method and density values of the Sr doped samples were between 2.66 g/cm^3 and 3.08 g/cm^3. Relative densities ranged from 84% to 100%.

The density of 0.7%, 1.8%, 3.1% and 3.2% wt. Mg-doped HA powders were found to be between 2.7-2.9 g/cm^3. These densities were lower than the density of the stoichiometric HA (3.16 g/cm^3). This was the result of the process of ionic substitution in the apatite structure, which was due to the increase in the number of structural defects (Landi et al., 2008). The density values obtained in this thesis are also consistent with the literature. The density values of Mg-doped samples were between 2.66 g/cm^3 and 3.14 g/cm^3.

The density of the samples increased with the sintering temperature as expected. The density values of the pure HA samples increased from 2.59 to 3.07 g/cm^3 with increasing sintering temperatures as seen in Table 10. Therefore, as the sintering temperature increased, the density of pure HA, which was closer to the theoretical density of 3.156 g/cm^3, was obtained. While there was no significant difference in the density of the HAs sintered at 900 and 1100°C except 0.5BHA, the relative densities of sintered pure and ion-doped HAs at 1100°C reached at least 92.5% of the theoretical density.

3.1.1.6 Vicker's Microhardness Measurements

The Vicker's microhardness of the sintered samples was measured to examine the effect of the addition of B, Sr and Mg ions to the structure of HA in terms of mechanical properties. The effect of temperature and ion doping on microhardness of the samples are shown in Table 11. According to the results, the lowest microhardness was obtained with 499.55 ± 33.31 MPa for 1Mg0.5BHA sample sintered at 700°C while the highest microhardness value (5067.52 ± 306.78 MPa) was obtained for 0.25Sr1Mg0.5BHA sintered at 1100°C.

The effects of sintering temperature on the mechanical properties of HA has been extensively studied. Vickers microhardness of pure HA ranged from 1.17 GPa to 6.86 GPa for various sintering temperatures (Muralithran and Ramesh, 2000; Ramesh et al., 2007). All HAs had the highest microhardness after sintering at

1300°C depending on the high relative densities of HAs, regardless of the amount of doping (Muralithran and Ramesh, 2000; Ramesh et al., 2007). These results showed that the sintering temperature had a significant effect on the microhardness of the HAs as it increased the density of the samples. Similar results were obtained in this thesis. As presented in Table 10, the densification of HAs with elevated sintering temperature was obtained. Accordingly, the microhardness of samples tended to increase. As seen in Table 11, the microhardness of almost all HAs significantly increased ($p<0.01$) with elevated sintering temperature which was in agreement with the literature.

Ion doping also had effects on the microhardness of the samples. In the study of Curran et al., an increase in microhardness was observed with the increase in Sr amount (Curran et al., 2011). In this thesis, the microhardness of the samples containing Sr sintered at 900°C was lower than the pure HA, but the microhardness of the samples containing Sr which were sintered at 700 and 1100°C was quite high compared to pure HA.

The microhardness values obtained in the study with Mg-doped HAs showed that the surface hardness of the nanocrystalline HA ceramics was affected by the presence of Mg during powder synthesis (Kalita and Bhatt, 2007). Accordingly, pure nano-HA exhibited a hardness of 323.6 ± 10.0 HV, while 1.0% wt. Mg-doped nano-HA had 387.5 ± 6.2 HV. This means a 20% increase for Mg-doped HA. Additionally, the relationship between density and microhardness was also examined and the density of sintered ceramics increased as the density increased. However, a significant decrease ($p<0.01$) in the microhardness of 1Mg0.5BHA samples was observed in this thesis. The hardness of the 0.5BHA sample sintered at 700°C was higher than that of pure HA, while the microhardness decreased by 50% when Mg was added to this sample. In this case, it can be said that in the light of the literature, doping of B and Mg together had a negative effect on the microhardness of the samples. However, it is explained in the following sections that this negative effect did not influence the biological and mechanical properties of materials.

Table 11. Vicker's microhardness of the samples (n=5, mean ± standard deviation).

Sample	Vicker's Microhardness (MPa)		
	Sintering Temperature		
	700°C	900°C	1100°C
HA	641.58 ± 125.47	2028.75 ± 186.19	2789 ± 296.24
0.5BHA	917.54 ± 166.87	1157.29 ± 167.04	2722.22 ± 319.87[£]
2Sr0.5BHA	1010.46 ± 160.22	786.12 ± 152.43	4025.16 ± 190.65
1Sr0.25Mg0.5BHA	927.04 ± 120.92[$]	1018.15 ± 156.89[$]	3890.45 ± 292.86
0.75Sr0.5Mg0.5BHA	941.384 ± 57.11	1319.78 ± 81.24	4253.04 ± 322.95
0.5Sr0.75Mg0.5BHA	1148.5 ± 189.46[$]	1046.65 ± 83.09[$]	3930.43 ± 310.59
0.25Sr1Mg0.5BHA	1132.7 ± 137.92[$]	1060.19 ± 98.92[$]	5067.52 ± 306.78
1Mg0.5BHA	499.55 ± 33.31	771.43 ± 52.04	2921.39 ± 306.05[£]

$ indicates that there was no statistically significant difference ($p>0.05$) for the same group which were sintered at 700 and 900°C.
£ indicates that there was no statistically significant difference ($p>0.05$) between the sample and pure HA for that sintering temperature.
There was a significant difference between the control group and other groups at that particular sintering temperature.

3.1.1.7 Scanning Electron Microscopy (SEM)

A general view of the HA particles sintered at different temperatures are shown in Figure 7 and their average grain sizes measured from SEM images are presented at Table 12. The morphology of synthesized HA particles in the SEM images was similar. Different phases (HA and β-TCP) of the materials could not be distinguished from each other just by investigating their morphology by means of SEM images. As the sintering temperature was elevated, the growth and coarsening of crystallites were confirmed by the SEM micrographs. Average grain sizes were in the range of 48-82 nm, 99-116 nm and 231-427 nm for the sintering temperatures of 700, 900 and 1100°C, respectively. In a study, the grain size of nHA particles sintered at 700°C remained at about 100 nm while for 900°C the grain size of the particles was tripled (Meejoo et al., 2006). HA-TCP composite powders sintered over a temperature range of 1000°–1300°C were reported to have an average grain size of 0.6–0.7 μm (Kıvrak

and Taş, 2005). In this thesis, smaller grain sizes were obtained for all sintering temperatures. Doping of different ions also affected the morphology of HA. In the samples involving B-Sr and Mg multi-doped, coarsening of the particles with elevated sintering temperature was much evident. Also, in pure HA, grain sizes upon sintering at 1100°C were higher compared to other samples. However, grain sizes of single or co-doped samples (2Sr0.5BHA, 0.5BHA and 1Mg0.5BHA) remained smaller than pure and multi-doped HAs. Even if the particle size of Mg and B co-doped sample was high for 700°C, as the sintering temperature was increased this doping hindered increase of the particle size. This effect was also reported for 1 wt-%Mg^{2+} doped HA (Kalita and Bhatt, 2007). The group reported that grain size of 1 wt-%Mg^{2+} doped HA was smaller than that of pure HA. In addition, since the Sr-hydroxyl distance is greater than the Ca-hydroxyl distance, the grains were expected to become more irregular as the hexagonal structure of HA was disrupted. Previous studies also showed that a fraction of Mg^{2+} ions incorporated into the HA structure leads to irregular grains and the remaining fraction adsorbed on the surface of HA inhibits grain growth (yields smaller grains) when the content of Mg^{2+} ions was low (~10%) (Geng et al., 2015). On the other hand, B incorporation was reported to result in a smaller, fine and ordered grain structure up to a certain dopant concentration (5%) (Pazarçeviren et al., 2021). In this thesis, a synergistic effect of three different dopant ions on grain size and morphology was observed. Among the samples sintered at 700°C while the average grain size of three ions multi-doped HAs was higher than observed in pure HA except 0.75Sr0.5Mg0.5BHA, it decreased for the samples sintered at 900°C and 1100°C. However, the changes between the groups at these sintering temperatures, were not statistically significant.

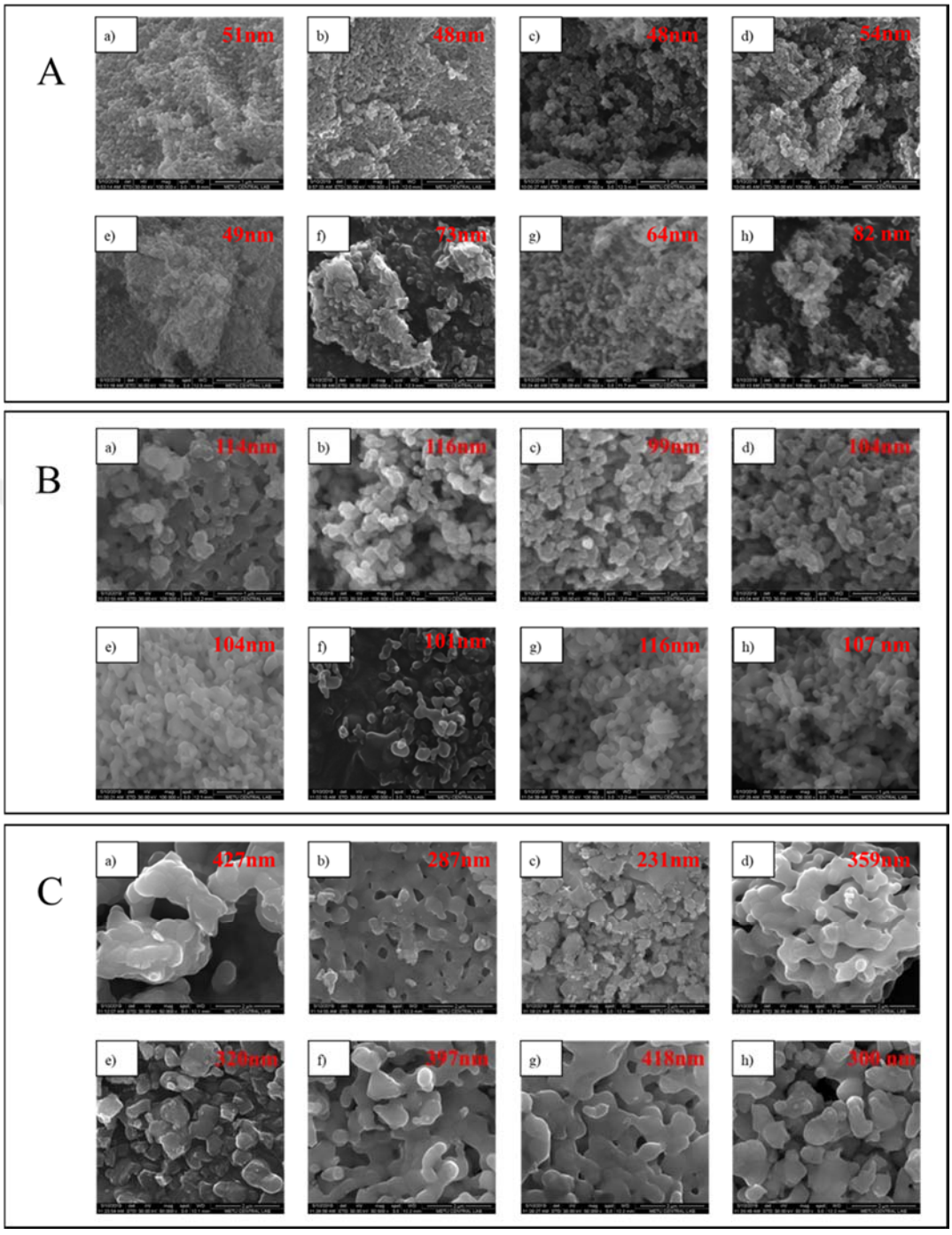

Figure 7. General view of HA particles sintered at A)700°C, B)900°C and C)1100°C; a) HA, b) 0.5BHA, c) 2Sr0.5BHA, d) 1Sr0.25Mg0.5BHA, e) 0.75Sr0.5Mg0.5BHA, f) 0.5Sr0.75Mg0.5BHA, g) 0.25Sr1Mg0.5BHA, h) 1Mg0.5BHA. Images provided evidence of increased grain size with increasing sintering temperatures.

Table 12. Average grain size of samples sintered at different temperatures.

Sample	Sintering Temperature	Average Grain Size (nm)
HA	700°C	$50.62 \pm 13.03^{\$,*}$
0.5BHA		$47.50 \pm 13.62^{\$,*}$
2Sr0.5BHA		$48.31 \pm 14.37^{\$,*}$
1Sr0.25Mg0.5BHA		$53.54 \pm 13.60^{\$,*}$
0.75Sr0.5Mg0.5BHA		$49.23 \pm 13.80^{\$,*}$
0.5Sr0.75Mg0.5BHA		$72.54 \pm 24.01^{*}$
0.25Sr1Mg0.5BHA		$63.81 \pm 18.36^{\$,*}$
1Mg0.5BHA		$82.34 \pm 27.91^{*}$
HA	900°C	$114.37 \pm 31.13^{+,\$}$
0.5BHA		$115.57 \pm 34.11^{+,\$}$
2Sr 0.5BHA		$98.80 \pm 27.56^{\$}$
1Sr 0.25Mg 0.5BHA		$103.75 \pm 32.80^{+,\$}$
0.75Sr 0.5Mg 0.5BHA		$103.76 \pm 31.47^{+,\$}$
0.5Sr 0.75Mg 0.5BHA		$100.71 \pm 30.97^{+}$
0.25Sr 1Mg 0.5BHA		$116.32 \pm 35.58^{+,\$}$
1Mg 0.5BHA		106.68 ± 36.59
HA	1100°C	$427.13 \pm 120.49^{*,+}$
0.5BHA		$287.34 \pm 122.05^{*,+}$
2Sr 0.5BHA		$231.45 \pm 136.35^{*}$
1Sr 0.25Mg 0.5BHA		$359.19 \pm 136.60^{*,+}$
0.75Sr 0.5Mg 0.5BHA		$319.96 \pm 149.15^{*,+}$
0.5Sr 0.75Mg 0.5BHA		$397.45 \pm 136.34^{*,+}$
0.25Sr 1Mg 0.5BHA		$418.14 \pm 152.43^{*,+}$
1Mg 0.5BHA		$300.24 \pm 191.60^{*}$

$ indicates that there is statistically significant difference ($p<0.05$) for the same group sintered at 700 and 900°C, while + and * represents statistical difference ($p<0.05$) for the same group sintered at 900-1100°C and 700-1100°C, respectively.

There is no significant difference between the groups at the particular sintering temperature.

3.1.2 Mechanical Properties

3.1.2.1 Compression Test

Pure and doped HAs sintered at 700, 900 and 1100°C were mechanically tested until facture was obtained. The maximum compressive strengths of the samples are given in Table 13.

Table 13. Compressive strength of samples sintered at 700, 900 and 1100°C (n=10).

Sample	σ_F (MPa)		
	700°C	900°C	1100°C
HA	8.67±2.11$^{\$,*}$	897.0±86.84$^{+,\$}$	3289.0±196.63$^{*,+}$
0.5BHA	10.79±2.06$^{\$,*}$	3027.8±162.52$^{\$,\#}$	2939.6±182.44*
2Sr 0.5BHA	21.77±3.63$^{\$,*}$	846.1±76.95$^{+,\$}$	5346.9±346.88$^{*,+}$
1Sr 0.25Mg 0.5BHA	16.23±3.27$^{\$,*}$	915.2±84.61$^{+,\$}$	1503.2±104.57$^{*,+,\#}$
0.75Sr 0.5Mg 0.5BHA	21.11±4.03$^{\$,*}$	1065.4±89.97$^{+,\$}$	6862.6±283.49$^{*,+,\#}$
0.5Sr 0.75Mg 0.5BHA	25.04±2.79$^{\$,*}$	1071.7±90.32$^{+,\$}$	5243.4±293.31$^{*,+}$
0.25Sr 1Mg 0.5BHA	21.89±3.66$^{\$,*}$	739.8±66.92$^{+,\$}$	3040.9±179.68$^{*,+}$
1Mg 0.5BHA	32.24±4.85$^{\$,*}$	998.3±91.07$^{+,\$}$	1924.9±124.73$^{*,+,\#}$

$ indicates that there is statistically significant difference ($p<0.05$) for the same group sintered at 700 and 900°C, while + and * represents statistical difference ($p<0.05$) for the same group sintered at 900-1100°C and 700-1100°C, respectively.

shows there is significant difference ($p<0.05$) between the marked group and all the groups at the particular sintering temperature.

The strength of brittle polycrystalline materials is highly dependent on porosity and grain size (Knudsen, 1959). Rao and Boehm (1974) reported that the compressive strength of apatite is exponentially dependent on porosity (Rao and Boehm, 1974).

Both the modulus of elasticity and Poisson's ratio were found to be linearly proportional to the density of sintered hydroxyapatite with a theoretical density

above 75%. As the porosity increased from about 8% to about 70%, compressive strength decreased logarithmically (Watts, 1993).

Aoki (1991) reported that the mechanical properties of sintered synthetic HA varied depending on the sintering temperature. According to this study, as the sintering temperature was varied between 1150 to 1300 °C, compressive strength of the samples increased from 308 ± 46 MPa to 509 ± 57 MPa while the elastic modulus of the samples increased from 42.2 ± 3.8 GPa to 81.4 ± 4.6 GPa (Aoki, 1991).

It was observed that the sample having the highest compressive strength was 0.75Sr0.5Mg0.5BHA ($p<0.05$) sintered at 1100°C, then 2Sr0.5BHA, 0.5Sr0.75Mg0.5BHA, HA, 0.25Sr1Mg0.5BHA, 0.5BHA, 1Mg0.5BHA and 1Sr0.25Mg 0.5BHA ($p<0.05$) groups were observed. Among the samples sintered at 900°C, the compressive strength of all groups increased with respect to the compressive strength of pure HA, except for the 2Sr0.5BHA and 0.25Sr1Mg0.5BHA groups. Accordingly, the groups having the highest compressive strength were as follows; 0.5BHA ($p<0.05$), 0.75Sr0.5Mg0.5BHA, 0.5Sr0.75Mg0.5BHA, 1Mg0.5BHA, 1Sr0.25Mg0.5BHA, HA, 2Sr0.5BHA and 0.25Sr1Mg0.5BHA. The compressive strength of all synthesized and sintered groups was found to be higher than the studies in literature (Akao et al., 1981; Aoki, 1991; Ascenzi and Bonucci, 1967; LeGeros, 1988).

Compared to the literature, the compressive strength of HA with different amounts of ion doped and sintered at different temperatures was approximately 10 times higher than that of cortical bone and approximately 3 times higher than dentine and dental enamel.

3.1.2.2 Diametral Test

Diametral tests of pure and doped HAs sintered at 700, 900 and 1100°C were performed until fracture (Table 14). The diametral strength of the samples ranged

from 3.87 to 18.04 MPa. The samples subjected to diametral testing had a density of 82.1-100.0% of the theoretical density of HA (Table 10).

Table 14. Diametral strength of the samples (n=10, mean ± standard deviation).

Sample	σD (MPa)		
	Sintering Temperature		
	700˚C	900˚C	1100˚C
HA	$4.25 \pm 0.34^{\Psi,+}$	$5.59 \pm 0.75^{*,+}$	$14.29 \pm 1.07^{\Psi,*}$
0.5BHA	$4.9 \pm 1.18^{**}$	$4.18 \pm 2.3^{\Phi}$	$17.38 \pm 2.35^{**,\Phi}$
2Sr0.5BHA	$4.86 \pm 0.47^{\Omega}$	$5.86 \pm 3.16^{***}$	$14.59 \pm 2.2^{\$,\Omega,***}$
1Sr0.25Mg0.5BHA	$3.87 \pm 0.95^{\lambda}$	$4.41 \pm 0.78^{\#,¥}$	$13.92 \pm 2.17^{\lambda,¥}$
0.75Sr0.5Mg0.5BHA	$6.01 \pm 2.51^{++}$	$5.87 \pm 2.1^{‡}$	$9.78 \pm 2.34^{\$,++,‡}$
0.5Sr0.75Mg0.5BHA	5.48 ± 3.42^{Ø}	$7.27 \pm 1.9^{£}$	$18.04 \pm 3.04^{Ø,£}$
0.25Sr1Mg0.5BHA	$5.05 \pm 1.78^{¤}$	$7.74 \pm 1.35^{\$,¤}$	$7.69 \pm 2.19^{\#}$
1Mg0.5BHA	$3.69 \pm 1.17^{\$,\bullet,\wedge}$	$6.73 \pm 2.17^{¢,\wedge}$	$10.42 \pm 2.06^{\$,\bullet,¢}$

Number sign (#) indicates $p<0.01$, dollar sign ($) indicates ($p<0.05$) between the sample and pure HA (control) for that sintering temperature. Ψ, +, *, **, Φ, Ω, ***, λ, ¥, ++, ‡, Ø, £, ¤, ●, ^, ¢ show significant difference for the same group sintered at different temperatures at $p<0.05$.

Diametral strength of HAs may vary with various parameters. Some of these parameters can be listed as the contact area during the test, the diameter and thickness of the disc, the amount of porosity in the sample, the distribution of the pores, and the Poisson ratio of the material (Chau and Wei, 2001; Evis and Öztürk, 2008). The diametral strength of HA varies between 1-35 MPa (Bigi et al., 1993; Evis and Öztürk, 2008; Komlev et al., 2003) which is a fairly wide range. Diametral strength of the samples in this thesis increased with an increase in the density and sintering temperatures as reported in previous studies (Evis and Öztürk, 2008). For only 0.75Sr0.5Mg0.5BHA; the diametral strength of the sample sintered at 900°C was numerically less than that of the sample sintered at 700°C, however there was no significant difference. Additionally, ion addition affected the diametral strength of the materials. For example, while the diametral strength of pure HA sintered at

1100°C was 14.29±1.07 MPa, the highest diametral strength (18.04±3.04 MPa) was obtained in a sample of 0.5Sr0.75Mg0.5BHA sintered at 1100°C. However, the lowest diametral strength (3.69±1.17 MPa) was obtained from a sample of 1Mg0.5BHA sintered at 700°C, which was significantly different than all groups ($p<0.05$). The addition of Mg^{2+} ion to HA reduces the strength of ceramics (Zyman et al., 2006).

The maximum diametral strength of HA was affected predominantly by the amount of porosity of the material (Bigi et al., 1993; Chau and Wei, 2001; Evis and Öztürk, 2008). However, other factors such as particle size, presence of impurities, distribution of pores, and the presence of second phases may also affect the diametral strength of HA. The presence of multiple phases such as β-TCP and HA may lead to a reduction in the diametral strength of the HA/β-TCP biphasic ceramics. This may be due to stress formation in samples due to differences in thermal expansion coefficients of co-existing phases (Ślósarczyk et al., 1997). However, biphasic ceramics had higher biological reactivity and osteointegration than pure HA (Kannan and Ferreira, 2006; Ślósarczyk et al., 1997). β-TCP phase in biphasic ceramics promotes bone growth due to its relatively higher biodegradation rate and bone-bonding ability (Yang and Wang, 1998). Interestingly, the highest diametral strength (18.0 MPa) was obtained in the 0.5Sr0.75Mg0.5BHA sample sintered at 1100°C with 51.5% β-TCP phase. It was previously proposed that due to the combination of compressive strengths of porous TCP and porous HA networks, the interpenetrating TCP/HA composite would have a sufficient compressive strength (Miao et al., 2005).

3.1.3 Biological Characterization

3.1.3.1 Alamar Blue™ Cell Viability Test

To mimic the ionic environment of natural bone, B, Mg or Sr doping to HA have been reported to improve osteogenic properties and biocompatibility of HA (Capuccini et al., 2009; Kulanthaivel et al., 2015; Tunçay et al., 2017). The viability

of Saos-2 cells on the pure and multi-doped HA sintered at 700, 900 and 1100°C was determined by the AlamarBlue^{TM} cell viability assay for 7 days (Figure 8). Pure HA was used as a control group because HAs are biocompatible and have positive effect on cell proliferation (Bose et al., 2010; Lee et al., 2013; Zhang et al., 2015). Relative cell viability on all the samples sintered at 700°C (Figure 8A) was higher than pure HA (control) except 0.75Sr0.5Mg0.5BHA which was also close to pure HA on the first day. The viability of cells in 0.5BHA group significantly increased ($p<0.05$). Cell viability on 1Sr0.25Mg0.5BHA increased two-fold with respect to pure HA ($p<0.05$). At the 4th day, cell viability almost doubled in 1Sr0.25Mg0.5BHA, 0.5Sr0.75Mg0.5BHA and 1Mg0.5BHA groups, while cell viability increase in 0.25Sr1Mg0.5BHA groups was 3.5-fold, demonstrating active bone cell proliferation. On the 7th day, the viability of cells in all groups, except 0.5BHA, significantly increased 2.5-3 times compared to the results of their first day, while the increase for 0.25Sr1Mg0.5BHA was 13%. For pure HA, this increase was about 0.5-fold. Even though the number of viable cells on 0.5BHA was less than the other groups, it was still higher than pure HA. Cell viability on 0.25Sr1Mg0.5BHA group decreased at day 7, but it was still higher than that of day 1.

Among the samples sintered at 900°C, results of the first day of incubation (Figure 8B) revealed that cell viability in all groups was 1.5-2.2 times higher than observed in pure HA ($p<0.05$ for 0.75Sr0.5Mg0.5BHA, $p<0.01$ for others). However, on the 4th day, cell viability in pure HA increased 2.5-fold, while cell viability in 0.5BHA group slightly decreased when compared to first day. Similarly to pure HA, the cell viability of the other groups was almost 3-fold. Nevertheless, on day 7, cell viability in 1Sr0.25Mg0.5BHA and 1Mg0.5BHA groups was lower than observed in pure HA group ($p<0.05$ for 1Sr0.25Mg0.5BHA, $p<0.01$ for 1Mg0.5BHA), while cells on 0.5BHA, 2Sr0.5BHA, 0.75Sr0.5Mg0.5BHA, 0.5Sr0.75Mg0.5BHA and 0.25Sr1Mg0.5BHA continued to proliferate. Çiftci et al. (2015) studied the adhesion, proliferation and osteogenic differentiation of human bone marrow-derived mesenchymal stem cells (MSCs) on B-doped nano HA. They reported that the

adhesion and proliferation rates of MSCs were higher on B-doped nano-HA than on those of pure HA (control) (Çiftci et al., 2014).

Relative cell viability on the samples sintered at 1100°C is presented in Figure 8C. Among all groups 2Sr0.5BHA had higher cell proliferation. The viability of 2Sr0.5BHA was 4 times higher ($p<0.01$) than that of control on day 7. The highest cell proliferation was observed in this group on all days. The doping of Sr into the structure of CaPs was reported to be beneficial on the response of various hard tissue-related cells *in vitro* (Avcı et al., 2017; Ravi et al., 2012). In this thesis, AlamarBlue™ assay results clearly showed that the Sr-doped HA was non-cytotoxic, and it also promoted cell proliferation. In another study, Sr-doped HA increased adhesion and proliferation of OPC1 cells and showed no negative effect on extracellular matrix formation and mineralization compared to pure HA (Xue et al., 2006).

Magnesium is one of the most important divalent ions associated with biological apatite. In a study by Qi et al., Ti6Al4V was coated with Mg doped HA ($(Ca_{10-x}Mg_x)(PO_4)_6(OH)_2$) and magnesium added up to $x = 2$ had no inhibitory effect on the growth of MG63 cells. The study of Landi et al., also showed that Mg-doped HA was a favorable biomaterial in terms of adhesion and proliferation of osteoblast-like cells (MG-63) as well as for osteoblast precursors (MSCs) compared to stoichiometric HA (Landi et al., 2008). In this thesis, B, Sr and Mg co-doped HA promoted cell proliferation which was in agreement with the literature (Gopi et al., 2014b; Qi et al., 2008).

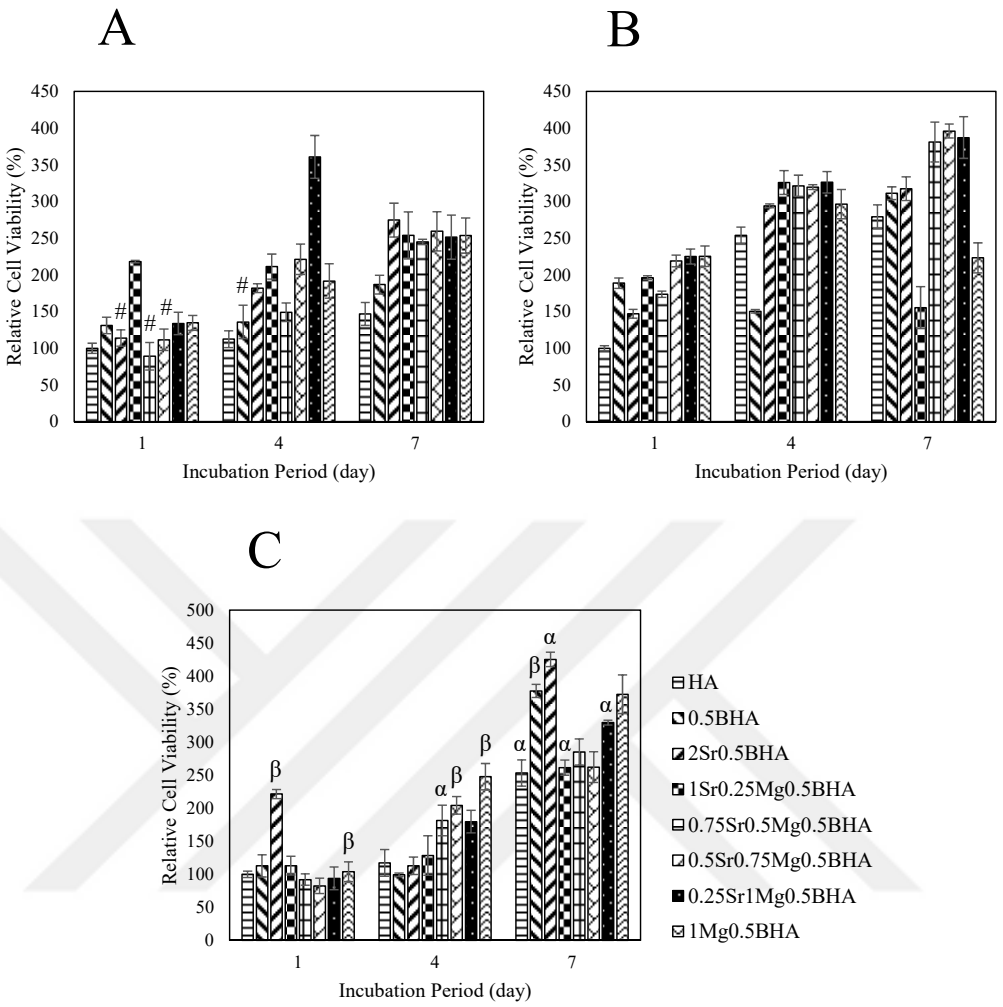

Figure 8. Viability of Saos-2 cells on pure and doped HA sintered at A) 700°C, B) 900°C and C) 1100° C and incubated for 1, 4 and 7 days (n=4). The error bars represent the standard error of means. For Figures A and B at day 1 there was significant difference ($p<0.05$) between pure HA and all groups sintered at the same temperature, except the groups indicated with # ($p>0.05$). α and β denote statistical difference between the group and pure HA group, at day 1 (α: $p<0.01$, β: $p<0.05$).

There was no toxic effect of the ion addition or the sintering temperature on Saos-2 cells. However, as the sintering temperature increased, the rate of proliferation of the cells was slower between 1st and 4th days, and highest increase was observed on the 7th day.

Many factors such as surface area, topography, surface energy of the implanted material affect the cell response (Ratner et al., 1987; Zreiqat et al., 2005).

Accordingly, they all depend on the grain size of the material (Webster, 2001). Most of the studies suggested that better cell proliferation rate was obtained on HA with smaller grain size. Due to the lower contact angle obtained with the reduction in the grain size, higher cell media interact with HA surface which is the reason for better cell proliferation rate (Bose et al., 2010). However, some studies showed that higher grain sized HA was obtained with higher sintering temperatures and the proliferation rate of cells on these HAs was higher than the others. For example, in a study of Wang et al., HA sintered with three different temperatures was seeded with Saos-2 cells. The highest proliferation rate of Saos-2 cells was obtained on HA sintered at high temperature (1200°C) (Wang et al., 2004). In the present study, when the sintering temperature increased from 700 to 900°C, cell proliferation rates were generally increased. With increasing the sintering temperature to 1100°C, a small decrease in the cell proliferation rate was observed. However, cell viability on the groups of 0.5BHA and 2Sr0.5BHA sintered at 1100°C remained as high as those on 900°C. Owing to higher diametral strength and crystallinity values, it can be thought that samples sintered at 1100°C have potential to be used in BTE.

3.1.3.2 Alkaline Phosphatase (ALP) Activity Test

During active bone deposition osteoblast cells produce ALP, therefore ALP is one of the early markers of osteogenic differentiation (Watts, 1999). ALP activity was determined to investigate the effect of B, Sr and Mg ions in the structure of HA, on the osteogenic activity of Saos-2 cells. Specific ALP activities of Saos-2 cells on pure and doped HAs after 7 and 14 days of incubation are presented in Figure 9.

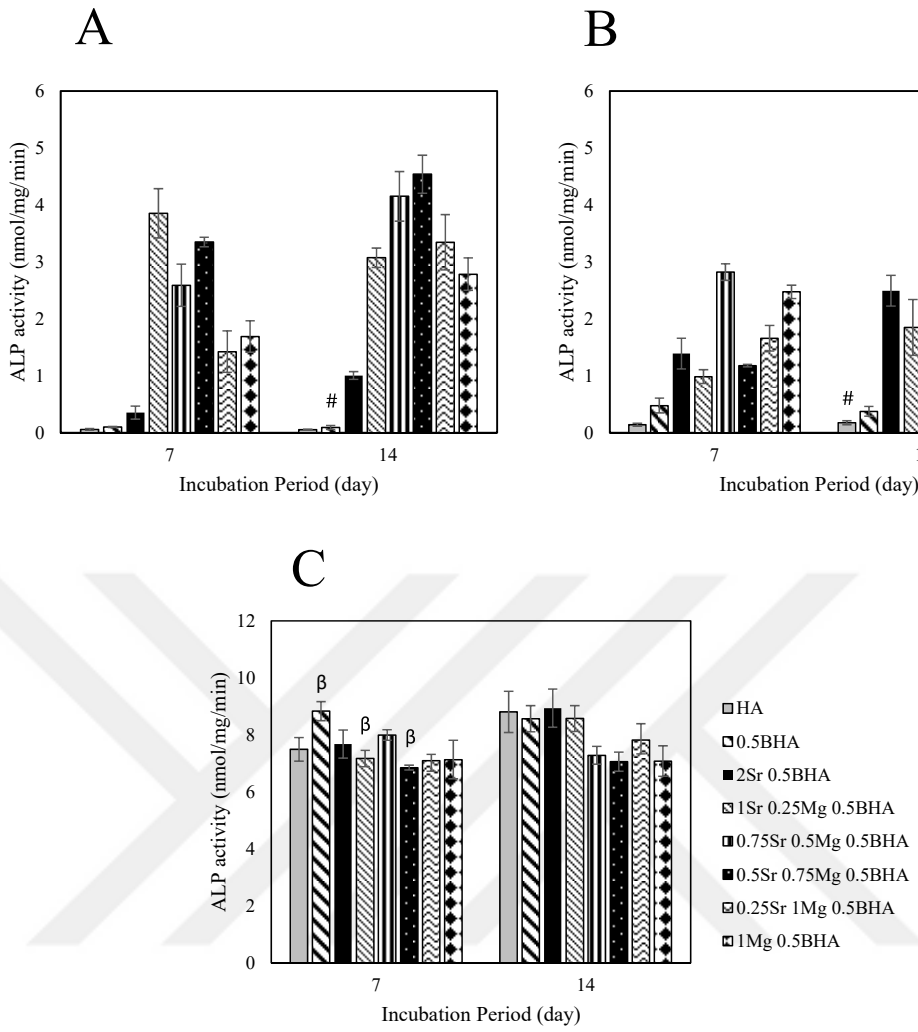

Figure 9. Specific ALP activity of Saos-2 cells seeded on pure and doped HA sintered at A) 700°C, B) 900°C and C) 1100°C and incubated in osteogenic differentiation medium at 37°C for 7 and 14 days (n=4). The error bars represent the standard error of means. For Figures A and B there was significant difference ($p<0.05$) between pure HA and all groups sintered at the same temperature at day 7, except the groups indicated with # ($p>0.05$). β implies the difference between pure HA and the given group at day 7 ($p<0.05$).

Among samples sintered at 700°C (Figure 9A), ALP activity of cells on 0.5BHA discs was quite close to that of pure HA. For the group 2Sr0.5BHA, ALP activity was higher than observed in pure HA on days 7 and 14. On day 7, 4-fold higher ALP activity was observed for 1Sr0.25Mg0.5BHA and 3-3.5-fold higher ALP activity for 0.75Sr0.5Mg0.5BHA and 0.5Sr0.75Mg0.5BHA groups compared to the control group. These results were also in agreement with the viability results (Figure 8). Compared to the control group, almost 2-fold increase in the osteogenic activity of

the cells on 0.25Sr1Mg0.5BHA and 1Mg0.5BHA groups was observed. On day 14, a slight decrease for 1Sr0.25Mg0.5BHA group was found while on the other group ALP activity continued to increase ($p<0.01$). ALP activity of cells on 1Sr0.25Mg0.5BHA reached its maximum value on day 7, while for 0.75Sr0.5Mg0.5BHA, 0.5Sr0.75Mg0.5BHA, 0.25Sr1Mg0.5BHA and 1Mg0.5BHA cells reached their maximum ALP activities on day 14. Moderate levels of Sr and Mg doping gave the highest ALP activity result for the samples sintered at 700°C. Proliferation of bone cell and bone formation *in vitro* were enhanced with Sr salts (Canalis, 1996), in a dose dependent manner, when they were both directly added into cell culture (Verberckmoes et al., 2003), and when they were associated to calcium-phosphate scaffolds (Qiu et al., 2006). Osteoblastic differentiation of MSC and osteogenic activity of MG63 cells were promoted with the presence of Sr in the samples (Capuccini et al., 2009; Coulombe et al., 2004; Curran et al., 2011). Other studies showed that Mg doping to HA structure leads to an increase in ALP production (Webster et al., 2004).

ALP activities of the Saos-2 cells on all doped HAs sintered at 900°C (Figure 9B) significantly increased ($p<0.05$ for 0.5BHA, $p<0.01$ for others) compared to pure HA. On day 7, the highest ALP activity was observed in 0.75Sr0.5Mg0.5BHA group. There was also 2.5-fold increase in 1Mg0.5BHA group compared to pure HA. On the 14^{th} day, among samples 0.75Sr0.5Mg0.5BHA and 0.5Sr0.75Mg0.5BHA gave the highest ALP activity result. Almost 5-fold increase was observed for these groups compared to pure HA. Again, 0.75Sr0.5Mg0.5BHA and 0.5Sr0.75Mg0.5BHA groups sintered at 900°C contributed the most to osteoblastic activity which was consistent with cell viability results (Figure 8B).

The osteogenic activity of cells on samples sintered at 1100°C (Figure 9C) was found to be quite high compared to samples sintered at 700 and 900°C. At day 7, ALP activity of the cells on 0.5BHA was significantly higher ($p<0.05$) than pure HA, while there was a slight decrease in the 1Sr0.25Mg0.5BHA and 0.5Sr0.75Mg0.5BHA groups ($p<0.05$). Moreover, even though no significant difference was found, lower ALP activity of cells was observed in other groups at

day 7 compared to pure HA. On the 14th day, among HA, 0.5BHA, 2Sr0.5BHA and 1Sr0.25Mg0.5BHA groups, for the groups having greater than or equal to 0.5 mol % Mg addition ($x \geq 0.5$, $Ca_{10-x-y}Mg_xSr_y(PO_4)_{6-z}B_z(OH)_2$), ALP activity of cells decreased or remained the same. Having higher osteoblastic activity on the samples sintered at 1100°C may be due to reaching confluency faster on these discs and transition from proliferation to differentiation state as reported by other researchers (Başar et al., 2010; Ratisoontorn et al., 2005).

3.2 Characterization of PCL-PEG-PCL

3.2.1 Fourier Transform Infrared Spectroscopy (FTIR)

PCL-PEG-PCL copolymer synthesized was characterized by FTIR analysis and its absorption peaks are presented in Figure 10A. Characteristic peaks of both PEG and PCL fragments were detected in the FTIR spectrum of the synthesized PCL-PEG-PCL triblock copolymer (Feng et al., 2012). Characteristic band of PCL, which is originating from C=O vibrations in the ester carbonyl group of the repeating PCL units, was detected at 1721 cm^{-1}. Another characteristic band of the PCL, which was assigned to -COO- vibrations was observed at 1238 cm^{-1}. Absorption bands resulted from symmetric and asymmetric -CH_2- stretching vibrations of homogeneous order of PCL units, were detected at 2945 cm^{-1} and 2866 cm^{-1}, respectively (Mishra et al., 2011). The tensile vibration for ether bonding of the PEG units in the PCL-PEG-PCL copolymer appeared at 1108 cm^{-1}. Peaks at 963 and 842 cm^{-1} were the characteristic bands of the crystal phase of PEG.

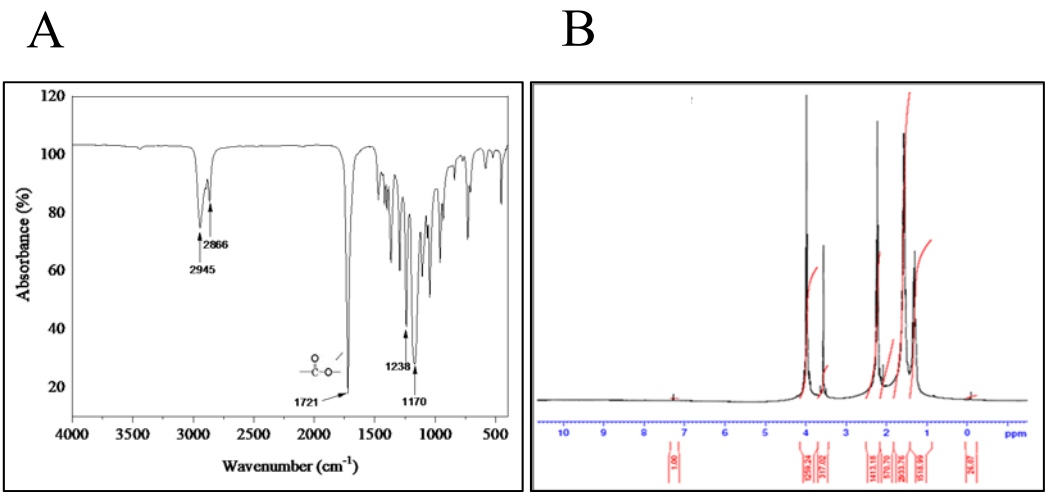

Figure 10. A) FTIR spectrum of synthesized PCL-PEG-PCL copolymer, B) ^{1}H NMR spectrum of synthesized PCL-PEG-PCL copolymer

3.2.2 Proton Nuclear Magnetic Resonance (^{1}H NMR) Spectroscopy

Synthesized PCL-PEG-PCL copolymer was characterized by ^{1}H NMR analysis and absorption peaks are presented in Figure 10B. The ^{1}H NMR spectrum of the PCL-PEG-PCL triblock copolymer displayed characteristic ^{1}H bands in accordance with the literature (Yuan et al., 2008). The peaks at 1.30, 1.65, 2.32 and 4.06 ppm define the methylene protons of -$(CH_2)_3$-, -$OCCH_2$- and -CH_2OOC- in PCL units, respectively. The peak at 3.65 ppm was due to -CH_2CH_2O- methylene protons in the PEG units in the block copolymer. Triblock copolymer formation was confirmed by very weak peaks at 4.23 and 3.82 ppm, resulting from -O-CH_2-CH_2- methylene protons in the PEG terminal associated with PCL blocks (Ma et al., 2010). ^{1}H NMR analysis showed that the synthesized polymer was a triblock copolymer and that the PEG blocks and PCL blocks were linked by ester bond.

The experimental and theoretical monomer ratios (ε-CL/EG) and average molecular weight (Mn) of the synthesized copolymer are given in Table 15. Mn value of the copolymer was determined using the initial concentration ratios and the integrity

ratio of the ^{1}H NMR peaks of the methylene protons (-CH_2-) belonging to the PCL and PEG segments at 4.07 ppm and 3.65 ppm, respectively (Liu et al., 2008).

Table 15. Average molecular weights of synthesized PCL-PEG-PCL triblock copolymer according to ^{1}H NMR and GPC analyses

Polymer	[ε-CL]/[EG]*	[ε-CL]/[EG]**	Mn*** (g/mol)	Mn& (g/mol)	Mw& (g/mol)	Mw/Mn&
PCL-PEG-PCL	9.25:1	3.96:1	45165.56	30486	47467	1.557

* Initial concentration ratio for polymerization reaction
** ^{1}H NMR peaks were used to calculate ε-PCL/PEG ratio.
*** The Mn value was determined based on the integrity ratio of ^{1}H NMR peaks at 4.07 ppm and 3.65 ppm.
& The Mn, Mw and Mw/Mn values were calculated from GPC analysis.

3.2.3 Gel Permeation Chromatography (GPC)

The number-average molecular weight (Mn), weight-average molecular weight (Mw) and polydispersity index (PDI, Mw/Mn) of the synthesized PCL-PEG-PCL triblock copolymer were obtained with GPC and the data obtained are presented in Table 15.

PDI is a measure of the molecular mass distribution in the polymer sample, and the PDI value for a homogeneous molecular weight polymer is 1. This value increases as the polymer dispersion becomes less homogeneous. Typical commercial polymers have PDI values in the range of 1.5-5. The PDI value of the synthesized PCL-PEG-PCL (1.557) was found to be very close to 1.5. This indicates that the triblock copolymer had a homogeneous molecular mass distribution.

3.3 Characterization of PCL-PEG-PCL/B, Sr, Mg Multi-Doped Hydroxyapatite Composite Scaffolds

3.3.1 Production of Composite Scaffolds

3.3.2 Determination of Porosity of Scaffolds

Macropores offer larger surface area for tissue growth in the implanted area, and having micropores inside macropores presents better cellular infiltration inside the scaffold (Gentile et al., 2012). It is known that the presence of different pore sizes in the scaffold structure causes faster and better bone healing (Roy et al., 2003). *In-vivo* studies have shown that a pore size less than 100 μm inhibits the bone growth (Lee et al., 2013). For this reason, the size of the porogen should be at least 100 μm in size. In order to obtain a homogeneous pore size, the porogen sizes must be homogeneous (Siddiq and Kennedy, 2015). For this reason, NaCl has been used in scaffolding after it is ground and sieved. After NaCl removal form the scaffolds, weight loss corresponded to the weight of NaCl added to the scaffolds very close to the theoretical ones (Table 16). The porosity of the scaffolds is also presented in Table 16**.** The porosity of each scaffold, in 1:1 PCL-PEG-PCL: NaCl 1:1.45 and PCL-PEG-PCL:NaCl ratios were about 50% and almost 60%, respectively, which were close to the theoretical values ($p<0.05$).

Table 16. Theoretical and experimental weight changes in scaffolds by removal of NaCl and experimental porosity of the scaffolds (n = 5)

Sample	Theoretical Weight Change (%)	Experimental Weight Change (%)	Experimental Porosity (%)
1:1	-65.52	-64.27±0.94	49.04±0.72*
1:1.45	-64.29	-63.08±1.02	58.87±0.95#
1:1+10% HA	-63.34	-61.23±1.35	48.33±1.07*
1:1+20% HA	-71.05	-70.3±0.96	49.49±0.68*
1:1.45+10% HA	-61.29	-59.88±1.67	58.61±1.64#
1:1.45+20% HA	-69.23	-68.25±0.98	59.15±0.85#
1:1+10% 0.5BHA	-63.34	-60.39±1.36	47.67±1.07*
1:1+20% 0.5BHA	-71.05	-70.86±1.54	49.87±1.08*
1:1.45+10% 0.5BHA	-61.29	-60.54±1.23	59.26±1.20#
1:1.45+20% 0.5BHA	-69.23	-68.88±1.92	59.69±1.66#
1:1+10% 2Sr 0.5BHA	-63.34	-63.06±1.78	49.77±1.41*
1:1+20% 2Sr 0.5BHA	-71.05	-69.92±0.96	49.21±0.67*
1:1.45+10% 2Sr 0.5BHA	-61.29	-59.86±1.20	58.60±1.17#
1:1.45+20% 2Sr 0.5BHA	-69.23	-68.41±1.52	59.29±1.32#
1:1+10% 0.5Sr 0.75Mg 0.5BHA	-63.34	-62.72±1.63	49.51±1.29*
1:1+20% 0.5Sr 0.75Mg 0.5BHA	-71.05	-69.07±1.21	48.61±0.85*
1:1.45+10% 0.5Sr 0.75Mg 0.5BHA	-61.29	-61.02±1.09	59.74±1.07#
1:1.45+20% 0.5Sr 0.75Mg 0.5BHA	-69.23	-68.78±1.47	59.61±1.27#

***** and # indicate significant difference ($p<0.05$) between 50% and 60% porosity, however there is no significant difference among the groups having the same porosity.

3.3.3 Thermogravimetric (TGA) Analysis of Scaffolds

After the compression molding process, scaffolds were incubated in a water bath for 2 days to make scaffolds free of porogen salt particles. Then, by heating the porous samples from 30°C to 1100°C, all contents except HA were removed. The results showed that the amount of HA in the scaffolds was very close to the theoretical values (Table 17).

Table 17. The amount of HA in the scaffolds

Sample	Theoretical Amount of HA (%)	Experimental Amount of HA (%)
1:1	0	0
1:1.45	0	0
1:1+10% HA	10	8.6
1:1+20% HA	20	16.4
1:1.45+10% HA	10	10.2
1:1.45+20% HA	20	17.4
1:1+10% 0.5BHA	10	8.2
1:1+20% 0.5BHA	20	16.8
1:1.45+10% 0.5BHA	10	9.3
1:1.45+20% 0.5BHA	20	17.1
1:1+10% 2Sr0.5BHA	10	8.5
1:1+20% 2Sr0.5BHA	20	18.2
1:1.45+10% 2Sr0.5BHA	10	8.8
1:1.45+20% 2Sr0.5BHA	20	16.9
1:1+10% 0.5Sr0.75Mg0.5BHA	10	9.1
1:1+20% 0.5Sr0.75Mg0.5BHA	20	17.2
1:1.45+10% 0.5Sr0.75Mg0.5BHA	10	8.9
1:1.45+20% 0.5Sr0.75Mg0.5BHA	20	17.3

3.3.4 *In Vitro* Degradation and Water Uptake Test

Degradation of polymers is affected by many factors, such as the molecular weight, molecular structure and composition of polymer, its crystallinity, and the presence of cross-links etc.(Göpferich, 1996). However, no significant change was observed in the structural unity and weights of pure PCL-PEG-PCL and PCL-PEG-PCL/B-Sr-Mg doped HA scaffolds during 3 weeks of incubation in PBS at 37°C. Moreover, the porosity of the scaffolds had no notable effect on the degradation of the scaffolds.

The water uptake of the scaffolds can propose the capacity to transport proteins and other body soluble substances from outside into and from inside to out of the scaffold, and can promote cellular invasion (Long et al., 2015). Water uptake capacity of the scaffolds containing 10% and 20% inorganic phase is presented in Figure 11A and 11B, respectively. This analysis showed that pure PCL-PEG-PCL and PCL-PEG-PCL/B-Sr-Mg doped HA scaffolds can keep a significant amount of water in their structure and water uptake continued to increase (Pazarçeviren et al., 2017; Türkkan et al., 2017). Higher water uptake ($p < 0.05$) was observed in 60% porous scaffolds with different amounts of pure/doped HA compared to their 50% porous counterparts. In addition, cationic ions like $Ca^{2+,}$ Sr^{2+} and Mg^{2+} in HA present strong water adsorption sites (Shimabayashi et al., 1981). Therefore, as the amount of inorganic phase increased, the water uptake percentage slightly increased, but there was no significant difference between the water uptake amounts of samples containing 20% inorganic phase and 10% inorganic phase. Similarly, no significant difference was found between the water uptake capacities of silk fibroin-PCL-PEG-PCL/PCL-based double-layered membranes containing different amounts (0%, 10% and 20% w/w to polymer) of Nano-CaP (Türkkan et al., 2017). However, in another study, ~65% porous PCL-PEG-PCL (PCEC) scaffolds containing different amounts of CLN were found to have higher water holding capacity than ~50% porous groups, and a significant difference was found between all groups (Pazarçeviren et al., 2017). This significant difference may have been due to non-homogeneous pore size distribution in the structure of the scaffolds. Water uptake capacity of materials is

highly influenced by the porosity. Therefore, higher porosity of the scaffolds provides large surface area and this could be the reason of higher water uptake (Park et al., 2015). In this thesis, porogen materials which were used for scaffolding were sieved to obtain homogeneous pore size distribution.

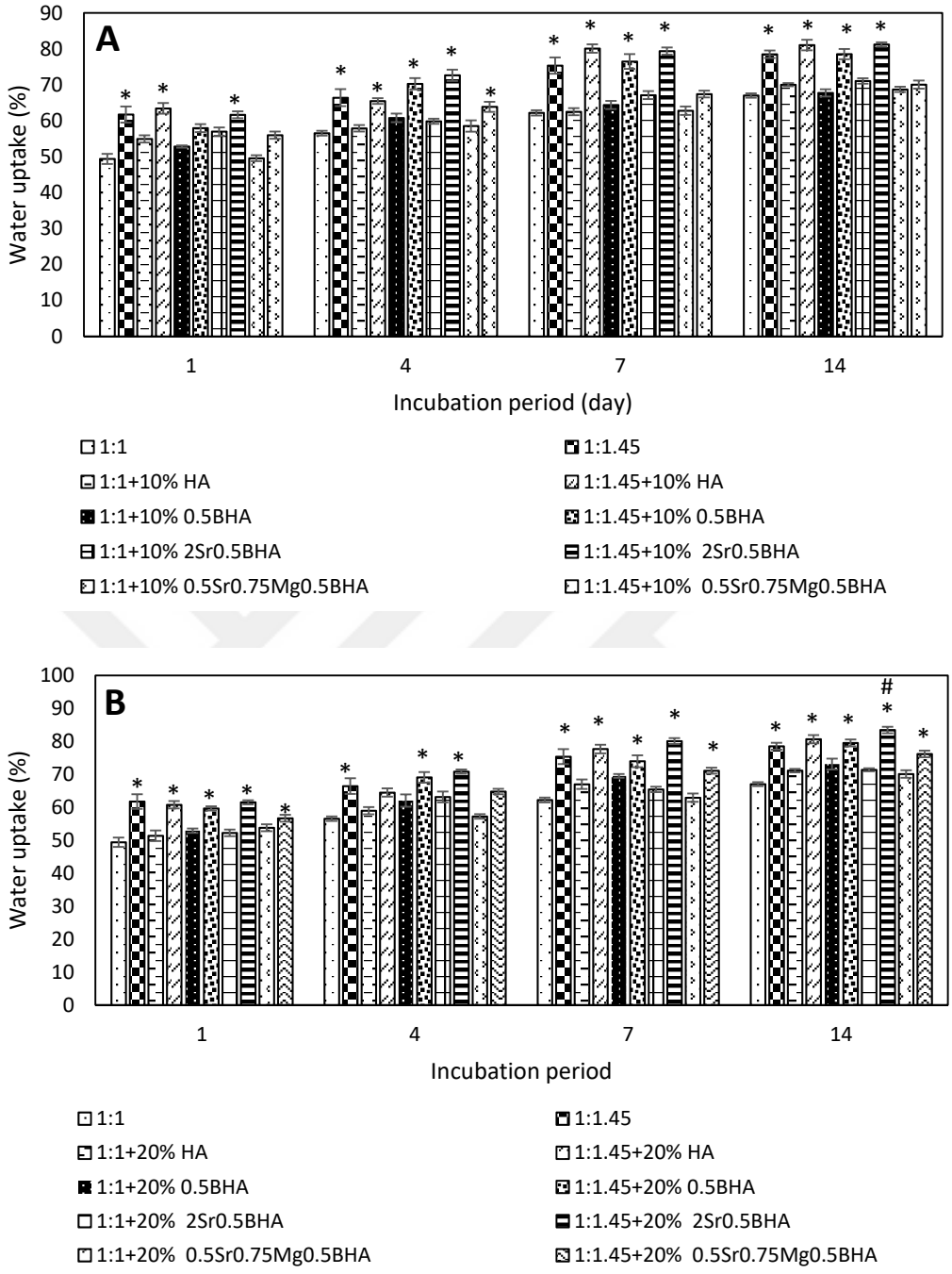

Figure 11. Water uptake capacity of the composite scaffolds containing A) 10% and B) 20% inorganic phase (n = 3). The water uptake capacity of the groups marked with * is significantly different from the 50% porous groups ($p<0.05$) at each incubation period. A significant difference is found between the water uptake capacity in the group marked with # and the other groups ($p<0.05$).

3.3.5 *In Vitro* Bioactivity Analysis

The bioactivity of the scaffolds was determined by placing scaffolds in SBF solution for different incubation periods (Figure 12 and Figure 13). CaP mineralization occurred on all scaffolds incubated in SBF solution. CaP precipitation was observed on scaffolds with 10% and 20% inorganic phases after 1 day of incubation, while in pure PCL-PEG-PCL scaffolds, a small amount of CaP precipitation was observed at the end of first week. Phosphate ions in SBF solution interact with positively charged calcium in pure HA, and positively charged calcium, magnesium and strontium ions in doped HA and transformed into amorphous CaP, which acts as a template for the formation of crystal apatite (Goh et al., 2014). Micro-sized spherical apatites formed on the surface of the scaffolds (Figure 12 and Figure 13). These apatites were observed without a regular orientation on the surface of the scaffolds and even in the inner regions of the pores. Faster CaP precipitation occurred on the scaffolds containing HA (especially pure HA and 2Sr0.5BHA) compared to the control group.

SEM analysis showed that apatite accumulation in 50% porous scaffolds was higher in the groups containing 20% 0.5BHA and 2Sr0.5BHA, among those with 60% porosity, the highest accumulation occurred in the scaffolds containing 10% HA and 20% 0.5BHA. This suggests that doping the B ion alone or with Sr increases bioactivity. Randomly distributed cauliflower-like apatite formations were observed in silk fibroin-PCL-PEG-PCL/PCL-based double-layer membranes containing 10% and 20% nano-CaP (Türkkan et al., 2017). In another study, more apatite was formed on the surface of Mg or Sr doped nano-HA/chitosan (nHA/CS) scaffolds than in pure nHA/CS scaffolds (Heshmatpour et al., 2018). In another study, SEM analysis showed that the addition of Sr ion to the structure of HA increases bioactivity (Suganthi et al., 2011). In the EDX elemental analysis, calcium, phosphate and oxygen ions present in the structure of CaPs were determined. In this analysis, the carbon ion originating from the polymer structure was also detected. At the end of 7 days of incubation, the Ca/P ratios of the apatite layer formed in the groups containing 50% porous pure HA and Sr and B doped HA (1.662 and 1.654,

respectively) were very close to the Ca/P ratio of stoichiometric HA (1.67). Ca/P ratios of sediments observed in other groups were in the range of 1.72-1.91, which belong to other CaP phases in the body (Paiva et al., 2006).

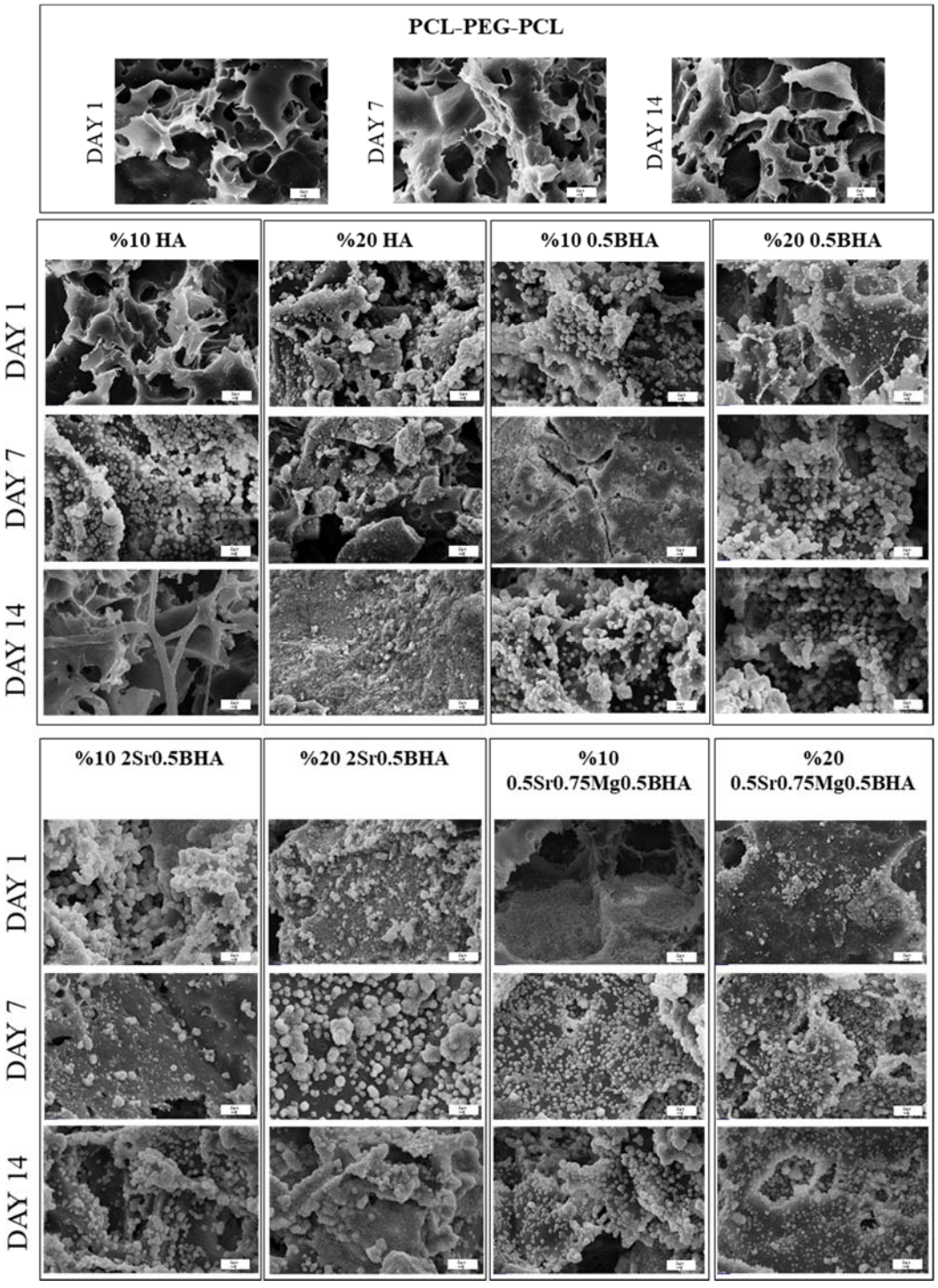

Figure 12. CaP accumulation on 50% porous scaffolds after 1, 7 and 14 days of incubation in SBF at 37ºC.

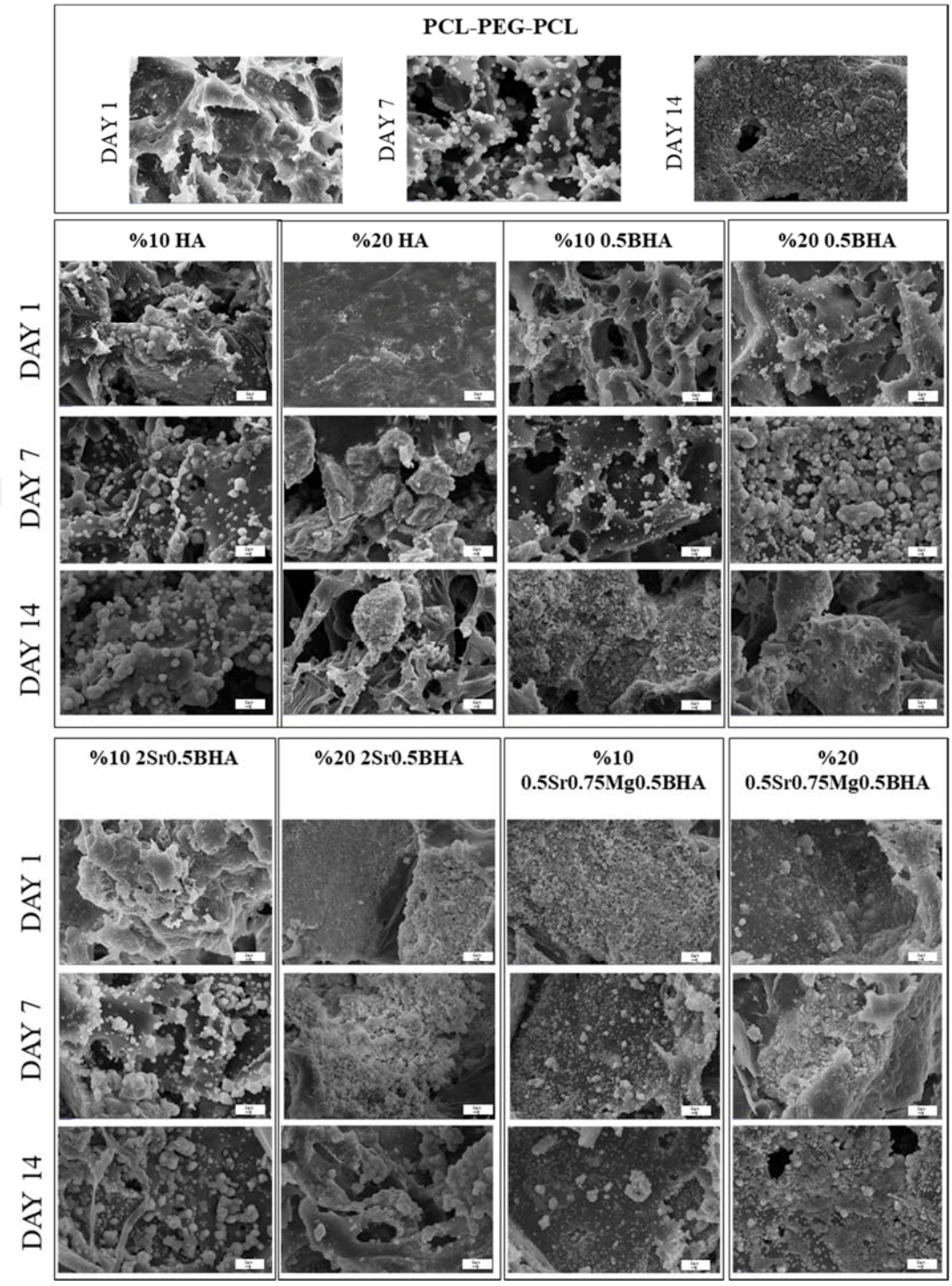

Figure 13. CaP accumulation on 60% porous scaffolds after 1, 7 and 14 days of incubation in SBF at 37ºC.

Change in pH of SBF in which pure PCL-PEG-PCL and PCL-PEG-PCL/B-Sr-Mg doped HA scaffolds were immersed for 14 days is shown in Figure 14. In the first 24h, there was a gradual increase in the pH value from 7.4 to 9.5 due to the ionic exchange between H^+ ions from SBF and Ca^{2+} ions on the surface (Alshemary et al., 2018). After 24h, pH of SBF in all samples decreased due to the use of OH- ions released by the SBF solution to form the apatite layer (Gu et al., 2004). After 7 days of incubation, the pH of the solution stabilized by the balance established between the dissolution/precipitation processes.

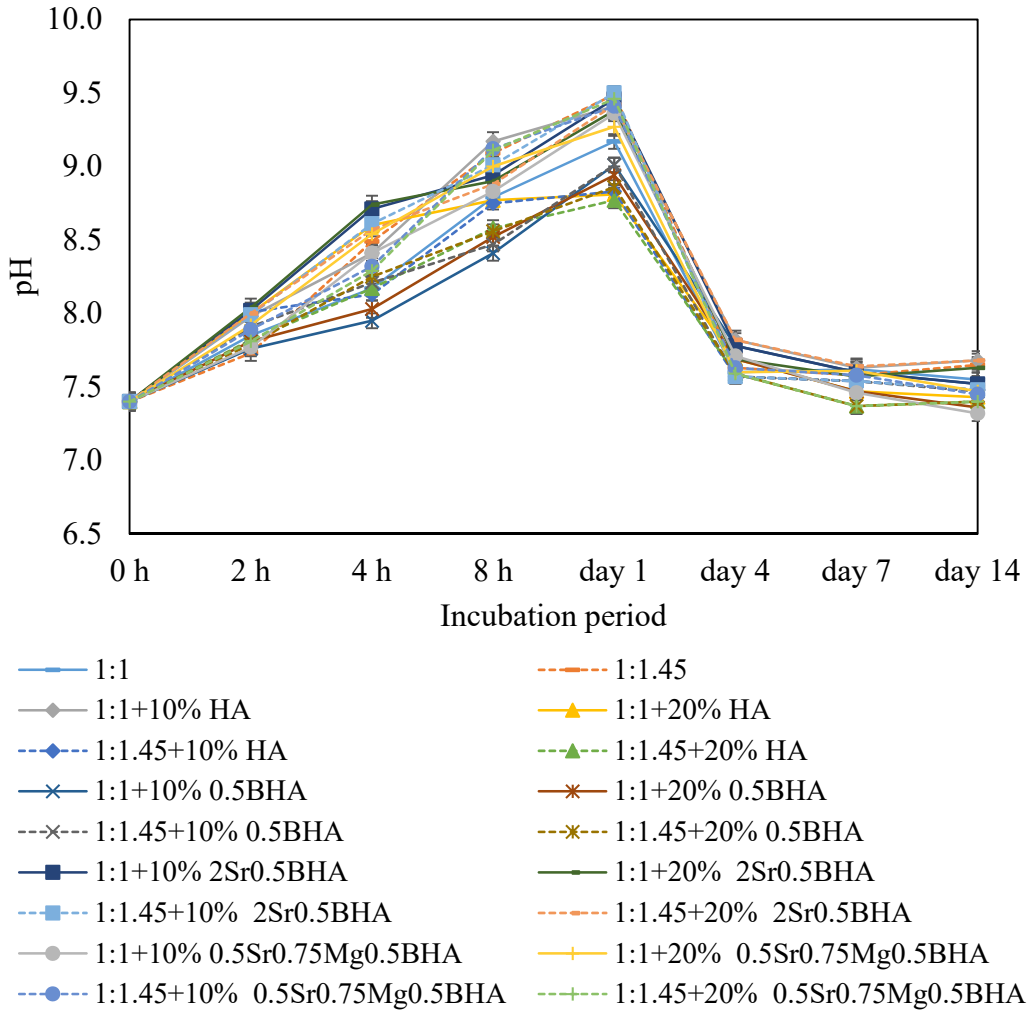

Figure 14. Change in the pH of SBF in which PCL-PEG-PCL/B-Sr-Mg doped HA scaffolds are incubated (n = 5)

3.3.6 Compression Test

In literature, the required mechanical strength of a scaffold has been specified as a minimum of 100 kPa depending on the target tissue (Zhang et al., 2006). Pure PCL-PEG-PCL and PCL-PEG-PCL / B-Sr-Mg doped HA composite scaffolds were mechanically tested and until 10% strain was obtained in the samples the test was continued. The compressive strength and modulus of the samples were obtained from the maximum point of the stress-strain curve (Table 18). Compressive strengths of all scaffolds were similar. Compressive strength decreases with increased porosity (Karageorgiou and Kaplan, 2005). Therefore, as expected, scaffold groups with 1:1 PCL-PEG-PCL: NaCl ratio (50% porosity) showed higher compressive strength than the other groups (60% porosity). Scaffolds containing 2Sr0.5BHA with 50% porosity (1:1 + 10% 2Sr0.5BHA and 1:1 + 20% 2Sr0.5BHA) had higher compressive strength than all other scaffolds ($p < 0.05$). The effect of HA content in composite scaffolds on the compressive strength of the scaffolds was clearly seen. Scaffolds with higher HA content provided better compressive strength than scaffolds containing less HA ($p < 0.01$). In addition, the highest compressive strength after 2Sr0.5BHA scaffolds was obtained in groups containing pure HA, 0.5BHA and 0.5Sr0.75Mg0.5BHA, respectively ($p < 0.05$). An average of 32%, 52%, 93% and 129% increase for scaffolds containing 0.5Sr0.75Mg0.5BHA, 0.5BHA, pure HA, and 2Sr0.5BHA was observed respectively, compared to the maximum compressive stresses of the control groups (50% and 60% porous pure PCL-PEG-PCL). Increase in porosity of scaffolds causes a decrease in the mechanical properties (Saghebasl et al., 2018). As stated in literature, as the volume of pores in the structure increases, stress concentration points increases around the perimeter of the pores (Rice, 1997). Therefore, the lower porosity of 50% porous scaffolds provided significantly higher compressive strength than the 60% porous scaffolds. Although not statistically significant, the compressive strength and compressive modulus were found higher in the 50% porous groups with the same ions than the 60% porous groups. In the study of Pazarçeviren et al., higher compressive strength and compressive modulus

were obtained in groups with low porosity (1:1 PCEC:$NaHCO_3$) than groups with high porosity (1: 2, PCEC: $NaHCO_3$). In addition, scaffolds with 20% inorganic phase (CLN) content offered better mechanical properties under compression compared to scaffolds containing 10% inorganic phases. Compressive modulus was also found lower in 1:2 (PCEC: $NaHCO_3$) groups with higher porosity (Pazarçeviren et al., 2017). Within studies conducted in the field of BTE, for example, a compressive strength of 4.5±0.3 MPa was obtained in composite scaffolds produced using Poly(lactide-co-glycolide) and HA (Kim et al., 2006). Compared to the literature, compressive strength and compression modulus of our scaffolds were found to be higher. However, both the type of materials used and the production method can change the results significantly. Due to its high contribution to the mechanical properties of scaffolds, scaffolds with 2Sr0.5BHA can be selected for further studies.

Table 18. Compressive strength and compressive modulus of the scaffolds (n=10)

Sample	Maximum Compressive Strength (MPa)	Compressive Modulus (MPa)
1:1	10.99 ± 0.27	62.74 ± 5.03
1:1.45	9.32 ± 0.16	59.88 ± 6.56
1:1+10% HA	19.11 ± 0.81$^{*,+}$	128.61 ± 7.59$^{*,+}$
1:1+20% HA	21.82 ± 0.86$^{*,+}$	134.72 ± 8.32$^{*,+}$
1:1.45+10% HA	18.65 ± 0.61$^{*,+}$	124.33 ± 8.87$^{*,+}$
1:1.45+20% HA	18.98 ± 0.52$^{*,+}$	126.92 ± 9.92$^{*,+}$
1:1+10% 0.5BHA	15.97 ± 0.82$^{*,\wedge}$	119.45 ± 7.44$^{*,\wedge}$
1:1+20% 0.5BHA	16.07 ± 0.97$^{*,\wedge}$	122.48 ± 6.96$^{*,\wedge}$
1:1.45+10% 0.5BHA	14.63 ± 0.41$^{*,\wedge}$	120.69 ± 5.98$^{*,\wedge}$
1:1.45+20% 0.5BHA	14.96 ± 0.63$^{*,\wedge}$	125.50 ± 8.09$^{*,\wedge}$
1:1+10% 2Sr0.5BHA	23.31 ± 0.37$^{*,\$}$	153.21 ± 9.17$^{*,\$}$
1:1+20% 2Sr0.5BHA	24.27 ± 1.14$^{*,\$}$	156.36 ± 7.94$^{*,\$}$
1:1.45+10% 2Sr0.5BHA	22.61 ± 0.96$^{*,\$}$	148.33 ± 7.93$^{*,\$}$
1:1.45+20% 2Sr0.5BHA	23.04 ± 0.74$^{*,\$}$	150.27 ± 7.12$^{*,\$}$
1:1+10% 0.5Sr0.75Mg0.5BHA	13.24 ± 0.71$^{*,£}$	117.63 ± 8.39$^{*,£}$
1:1+20% 0.5Sr0.75Mg0.5BHA	14.36 ± 0.68$^{*,£}$	120.06 ± 7.92$^{*,£}$
1:1.45+10% 0.5Sr0.75Mg0.5BHA	13.04 ± 0.60$^{*,£}$	113.49 ± 8.30$^{*,£}$
1:1.45+20% 0.5Sr0.75Mg0.5BHA	13.21 ± 0.84$^{*,£}$	116.98 ± 7.10$^{*,£}$

A statistically significant difference ($p<0.01$) was found when the groups marked with * were compared with 50% and 60% porous pure PCL-PEG-PCL (control). While the groups marked with +, ^, $ and £ did not have a significant difference within themselves, they had a difference of $p<0.05$ from the other groups.

3.3.7 Cell Culture Studies

3.3.7.1 Alamar Blue™ Cell Viability Test

Viability of Saos-2 cells on pure PCL-PEG-PCL and PCL-PEG-PCL/B-Sr-Mg doped HA composite scaffolds was evaluated by the AlamarBlue™ cell viability test after 1, 4 and 7 days of incubation (Figure 15A and 15B). Cell viability on pure PCL-PEG-PCL was considered 100% at the respective time point.

Higher cell viability was observed on pure PCL-PEG-PCL with 60% porosity compared to 50% porous pure PCL-PEG-PCL group ($p < 0.05$). In the other groups, it was observed that 60% porosity resulted in higher cell viability compared to 50% porosity for each group. However, no significant difference was found ($p = 0.08$). Cell viability on the scaffolds increased with time, except for the groups containing 0.5Sr0.75Mg0.5BHA and 10% 0.5BHA.

Among 50% porous samples, there were significant increase ($p<0.05$) in cell viability on the composite scaffolds containing 20% of HA, 0.5BHA and 2Sr0.5BHA compared to scaffolds containing 10% inorganic content. When 60% porous scaffolds were examined, smaller increase ($p<0.05$) was detected on scaffolds containing 20% 0.5BHA, 2Sr0.5BHA and 0.5Sr0.75Mg0.5BHA than containing 10% inorganic content compared to counterparts with 50%. However, scaffolds having 60% porosity with 10% HA showed better cell viability than scaffolds having 20% HA.

Bone typically contains 70% inorganic CaP and approximately 0.035% of the calcium content in the bone skeletal system contains different elements such as Sr and Mg (Habibovic and Barralet, 2011). The importance of these elements in natural bone health and cell proliferation has been documented by many researchers (Bonjour et al., 2009; Molino et al., 2017; Tao et al., 2016). In addition, Sr, Mg and B ions can have a positive effect especially on the proliferation and osteogenic differentiation of osteoblastic cells (Gentleman et al., 2010; Kim et al., 2017; Molino

et al., 2017). Therefore, in this thesis, it was expected to obtain higher cell viability in groups containing ion-doped HA than in groups containing pure HA with 50% porosity. However, no significant increase was observed in groups containing Mg-Sr-B ions together (0.5Sr0.75Mg0.5BHA) regardless of the porosity ratio and the amount of inorganic content. Among the samples containing ceramics, highest viability was observed on scaffolds containing 2Sr0.5BHA ($p < 0.01$). It was previously reported that higher cell density was observed on Sr-HA and Mg-HA coatings made on titanium for bone implants compared to HA coatings since the presence of these ions is known to facilitate the replication process of the preosteoblastic cells (Roy et al., 2011). A study reported that bone marrow derived stem cells on SrCaP/PCL/CS (chitosan) composite membranes showed the highest proliferation compared to PCL/CS and CaP/PCL/CS membranes and this proliferation accelerating effect of Sr^{2+} was attributed to the activation of the calcium-sensing receptor (CaR) (Ye et al., 2019). Another study conducted with Sr-doped borate-based bioactive glass scaffolds showed that, while borate-based bioglass inhibited the proliferation of MG-63 cells, strontium-doped borate-based bioglass significantly increased the proliferation of the same cells. The reason was that Sr which was doped in bioglass suppressed the rapid release of B and the cytotoxicity of glass scaffolds was minimized at least (Yin et al., 2018). As known, release of B can be cytotoxic. Nontoxic range of concentration is 5-25 mM (Brown et al., 2009; Fu et al., 2009). This shows that the Sr ion plays an important role in cell proliferation since Sr is a natural bone-seeking trace element that accumulates in the skeleton, especially in new trabecular bone and depending on the skeletal site, as in this thesis.

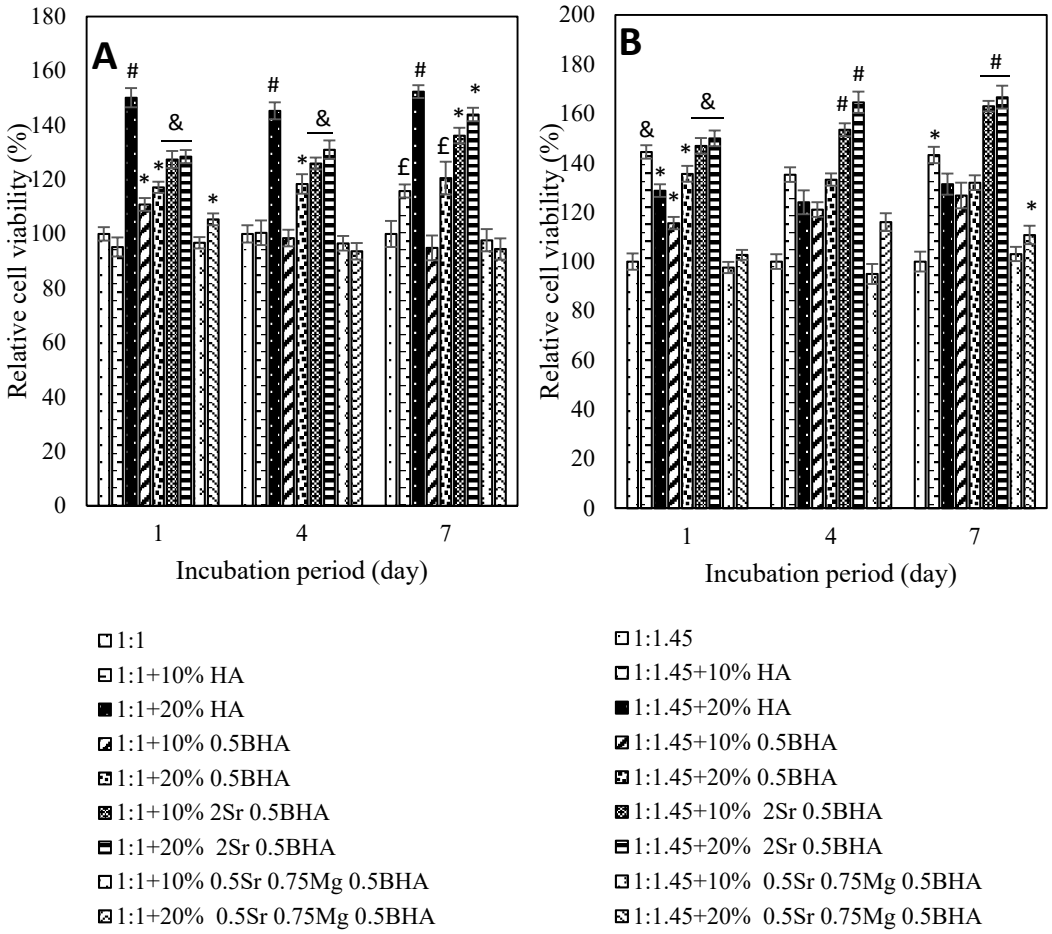

Figure 15**.** Relative cellular viability of Saos-2 cells on A) 50% porous B) 60% porous pure PCL-PEG-PCL and PCL-PEG-PCL / B-Sr-Mg doped HA composite scaffolds. Samples are incubated for 1, 4 and 7 days (n = 4). At each incubation period, a significant difference is found between the cell viability in the groups marked with *, &, £ and the other groups ($p<0.05$). The groups marked with £ do not differ significantly among themselves. Groups marked with # are significantly different from all groups ($p <0.01$). Viability on pure PCL-PEG-PCL was accepted as 100%.

3.3.7.2 Osteogenic Activity of Cells

Alkaline phosphatase (ALP) is a natural enzyme produced by osteoblast cells during osteogenesis. To investigate the early stage of cell differentiation, ALP expression and intracellular calcium accumulation are considered an early osteoblastic marker of osteogenic differentiation. The specific ALP activities of Saos-2 cells on composite scaffolds having different inorganic content (10% and 20%) with 50% and 60% porosity are presented in Figure 16A and 16B.

When 50% and 60% porous scaffolds were compared, it was found that the degree of porosity and the amount of inorganic phase did not make a significant difference on the ALP activity level. Cells on scaffolds containing HA with Sr and B co-doped (2Sr0.5BHA) showed the highest ALP activity (2.6-fold to control group) during the incubation period, regardless of the porosity. On the scaffolds containing only B-doped or Mg-Sr-B multi-doped HA, ALP activity was lower than 2Sr0.5BHA but very close to each other. Interestingly, cells on scaffolds with pure HA showed higher ALP activity than cells on B or Mg-Sr-B doped scaffolds. In literature, there were some studies that on the samples with B and Mg ions, ALP activity was lower than the control groups. For example, in a study conducted with B-supplemented S53P4 commercial bioglasses, ALP activity of cells incubated in both normal and osteogenic media significantly decreased compared to the control group (without boron) at days 7 and 14 (Ojansivu et al., 2018). The ALP activity of MG63 cells seeded on Mg doped bone cement and pure HA bone cement samples did not show a significant difference on the 4^{th} day, but on the 7^{th} day significantly higher ALP activity of MG63 cells on Mg added samples was observed compared to pure HA (Lu et al., 2011). As a result, obtaining lower ALP activity on scaffolds containing B-doped or Mg-Sr-B multi-doped HA than containing pure HA was probably an effect of the B ion contribution since B release can be cytotoxic or not sufficient to stimulate bone regeneration (Çiftci Dede et al., 2021). ALP activity of the cells significantly decreased at the end of the 14 days. Similarly, ALP levels of cells on PCL-PEG-PCL scaffolds with 10% and 20% CLN peaked in the first week, while

ALP levels of cells on the pure PCL-PEG-PCL scaffold peaked in the third week (Pazarçeviren et al., 2017).

Intracellular calcium accumulation after 7 and 14 days of incubation in osteogenic differentiation medium of Saos-2 cells seeded on composite scaffolds having different inorganic content (10% and 20%) with 50% and 60% porosity is presented in Figure 17A and 17B.

In parallel with specific ALP activity results, the highest intracellular calcium accumulation was observed in scaffolds containing 2Sr0.5BHA, HA, 0.5BHA and 0.5Sr0.75Mg0.5BHA, respectively. Although HA, 0.5BHA and 0.5Sr0.75Mg0.5BHA containing groups differed significantly ($p < 0.01$) from the control group, there was no significant difference among themselves. Obtaining higher intracellular calcium accumulation in scaffolds containing inorganic phase compared to pure PCL-PEG-PCL scaffolds was consistent with the literature. In nCaP-silk fibroin-PCL-PEG-PCL/PCL-based double-layer membranes, the presence of nCaP was found to improve the intracellular calcium storage of cells (Türkkan et al., 2017). A similar result was obtained in the study with PCL-PEG-PCL scaffolds containing Clinoptilolite (CLN). It was shown that hFOB cells seeded on scaffolds with CLN accumulated more intracellular calcium than in the control group (Pazarçeviren et al., 2017). At the end of the second week, the amount of intracellular calcium decreased in all groups. This was an expected result as specific ALP activities were also high at the end of the first week and significantly decreased at the end of the second week. As stated by Birmingham et al. (2012), intracellular calcium accumulation and increase in ALP activity occur simultaneously, exhibiting osteoblastic dependence (Birmingham et al., 2012). When 50% and 60% porous scaffolds were compared, it was found that the degree of porosity did not make a significant difference on the amount of intracellular calcium.

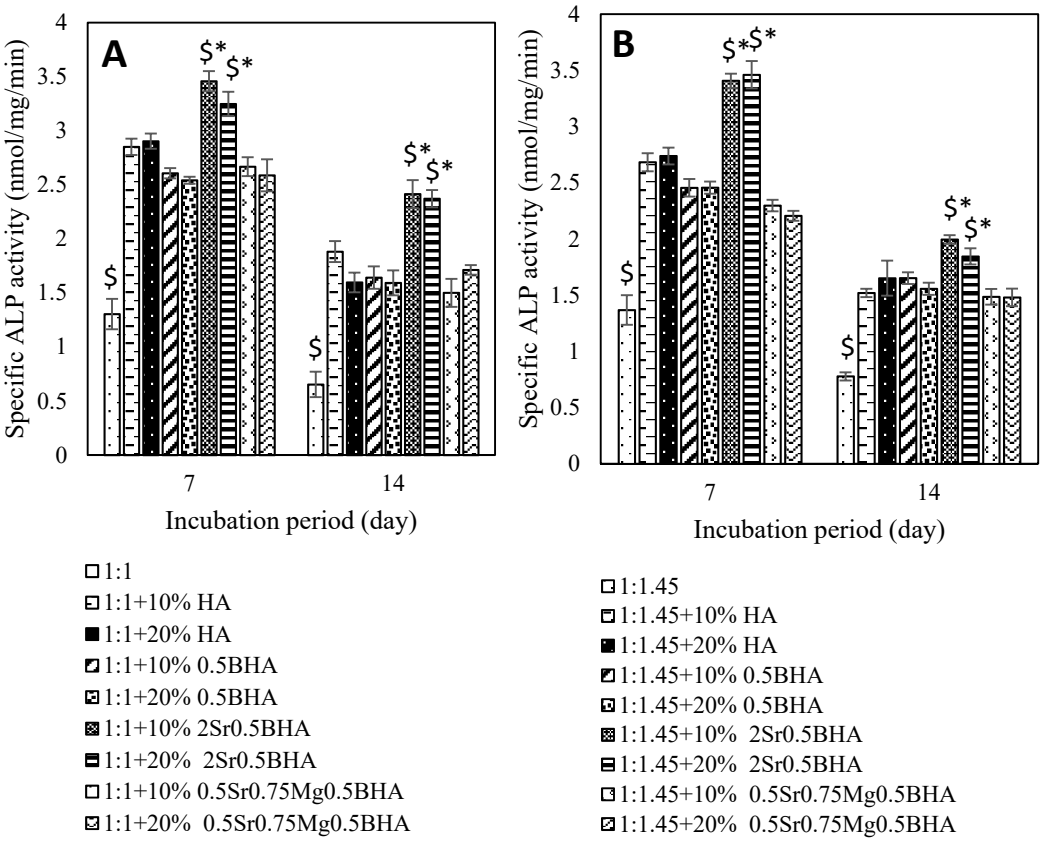

Figure 16. Specific ALP activity of Saos-2 cells seeded on A) 50% porous, B) 60% porous PCL-PEG-PCL/B-Sr-Mg doped HA composite scaffolds. Samples were incubated in osteogenic differentiation medium at 37°C for 7 and 14 days (n = 4). Error bars represent the standard error of the means (n = 4). A statistically significant difference ($p < 0.01$) in the ALP activity is found between the groups indicated by $ and the other groups. While the groups marked with $* do not differ significantly within themselves, they are different from the other groups at a level of significance of 0.01.

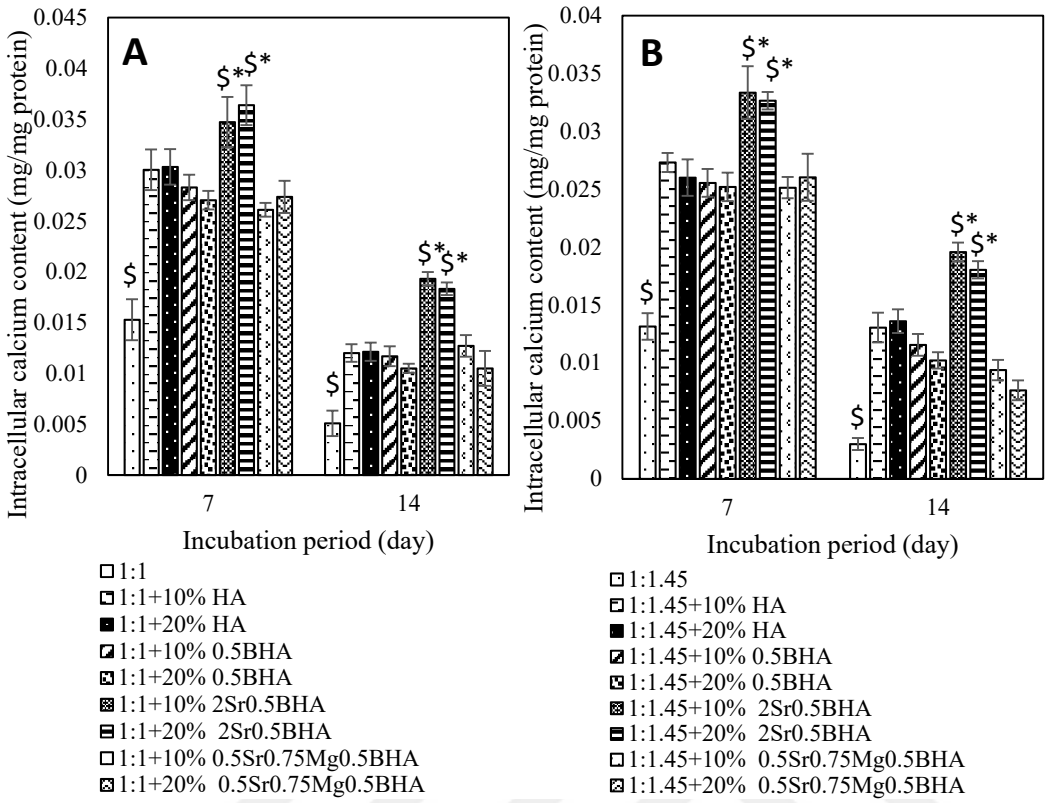

Figure 17. The amount of intracellular calcium accumulation of Saos-2 cells seeded on composite scaffolds with A) 50% porosity, B) 60% porosity. Samples were incubated in osteogenic differentiation medium at 37°C for 7 and 14 days (n = 4). Error bars represent the standard error of the means (n = 4). A statistically significant difference ($p < 0.01$) is found between the groups indicated by $ and the other groups. While the groups marked with $* do not differ significantly within themselves, they are different from the other groups at a level of significance of 0.01.

CHAPTER 4

CONCLUSION

In this study 3D porous composite scaffolds of PCL-PEG-PCL containing different amount of B-Sr-Mg multi-doped HAs were produced with compression molding and salt leaching method for BTE applications. The effect of the amount of inorganic phase and the porosity on the mechanical and the biological properties were investigated. The structural analysis determined by XRD and FTIR proved that B, Sr and Mg ions can be multi-doped successfully to the structure of HA. When the dopant amount was increased above x+z or y+z was greater than or equal to 1 for $Ca_{10-x-y}Mg_xSr_y(PO_4)_{6-z}(BO_3)_z(OH)_2$, biphasic structure was obtained. Especially, increasing Mg ion-doping (x=0.25 to 1) increased the amount of β-TCP gradually. Crystallinity and density of the samples gradually increased with increasing the sintering temperature. Microhardness of the samples increased within increase the sintering temperature. The addition of Mg^{+2} ion to HA reduced the diametral strength of the materials. B, Sr and Mg co-doped HA did not show any cytotoxic effect on Saos-2 cells. Additionally, such doping promoted cell proliferation whereas cells on samples sintered at 1100°C had higher osteogenic activity than on samples sintered at 700 and 900°C. For osteogenic differentiation level, samples sintered at 1100°C was found to be quite high compared to samples sintered at 700 and 900°C. Overall, results obtained in this study revealed that with the doping of Sr, Mg and B ions, biological properties of HA were clearly upgraded and samples sintered at 1100°C were suggested to have potential as a biomaterial for bone implant applications.

PCL-PEG-PCL/ B-Sr-Mg multi-doped HA composite scaffolds were fabricated with the method of compression molding/particulate leaching for bone regeneration applications. The effect of varying amount of multi-doped HA and porosity on the mechanical and biological properties were examined. The presence of pure or B-Sr-

Mg multi-doped HA was shown to improve the water uptake ability and the mechanical properties of the scaffolds. *In vitro* bioactivity study revealed that composite scaffolds containing HA (especially pure HA, 0.5BHA and 2Sr0.5BHA) showed faster CaP precipitation compared to the control group and apatite accumulation on these groups was higher. The presence of HA promoted an osteoinductive environment for the proliferation and osteogenic activity of osteoblastic cells. Highest relative cell viability and ALP activity of Saos-2 cells were observed on 2Sr0.5BHA containing PCL-PEG-PCL scaffolds. Therefore, PCL-PEG-PCL with 2Sr0.5BHA composite scaffolds are promising candidates for BTE applications.

REFERENCES

Aaseth, J., Boivin, G., Andersen, O., 2012. Osteoporosis and trace elements – An overview. J. Trace Elem. Med. Biol. 26, 149–152. https://doi.org/10.1016/j.jtemb.2012.03.017

Aina, V., Lusvardi, G., Annaz, B., Gibson, I.R., Imrie, F.E., Malavasi, G., Menabue, L., Cerrato, G., Martra, G., 2012. Magnesium- and strontium-co-substituted hydroxyapatite: the effects of doped-ions on the structure and chemico-physical properties. J. Mater. Sci. Mater. Med. 23, 2867–2879. https://doi.org/10.1007/s10856-012-4767-3

Akao, M., Aoki, H., Kato, K., 1981. Mechanical properties of sintered hydroxyapatite for prosthetic applications. J. Mater. Sci. 16, 809–812. https://doi.org/10.1007/BF02402799

Albayrak, O., 2016. Structural and mechanical characterization of boron doped biphasic calcium phosphate produced by wet chemical method and subsequent thermal treatment. Mater. Charact. 113, 82–89. https://doi.org/10.1016/j.matchar.2016.01.006

Albayrak, Ö., Uğurlu, M., 2016. Bor katkılı hidroksiapatit üretimi ve karakterizasyonu: Bor oranı ve sinterleme sıcaklığının yapı ve mekanik özellikler üzerindeki etkisi. J. Fac. Eng. Archit. Gazi Univ. 31, 749–761. https://doi.org/10.17341/gummfd.59636

AlHammad, M.S., 2016. Nanostructure hydroxyapatite based ceramics by sol gel method. J. Alloys Compd. 661, 251–256. https://doi.org/10.1016/j.jallcom.2015.11.045

Alshemary, A.Z., Engin Pazarceviren, A., Tezcaner, A., Evis, Z., 2018. Fe3+/SeO42− dual doped nano hydroxyapatite: A novel material for biomedical applications. J. Biomed. Mater. Res. - Part B Appl. Biomater. 106,

340–352. https://doi.org/10.1002/jbm.b.33838

Alshemary, A.Z., Goh, Y.-F., Akram, M., Razali, I.R., Abdul Kadir, M.R., Hussain, R., 2013. Microwave assisted synthesis of nano sized sulphate doped hydroxyapatite. Mater. Res. Bull. 48, 2106–2110. https://doi.org/10.1016/j.materresbull.2013.02.015

Aoki, H., 1991. Science and medical applications of hydroxyapatite. Sci. Med. Appl. HA 85, 1–57.

Ascenzi, A., Bonucci, E., 1967. The tensile properties of single osteons. Anat. Rec. 158, 375–386. https://doi.org/10.1002/ar.1091580403

Atila, D., Karataş, A., Evcin, A., Keskin, D., Tezcaner, A., 2019. Bacterial cellulose-reinforced boron-doped hydroxyapatite/gelatin scaffolds for bone tissue engineering. Cellulose 26, 9765–9785. https://doi.org/10.1007/s10570-019-02741-1

Avcı, M., Yilmaz, B., Tezcaner, A., Evis, Z., 2017. Strontium doped hydroxyapatite biomimetic coatings on Ti6Al4V plates. Ceram. Int. 43, 9431–9436. https://doi.org/10.1016/j.ceramint.2017.04.117

Badylak, S.F., Gilbert, T.W., 2008. Immune response to biologic scaffold materials. Semin. Immunol. 20, 109–116. https://doi.org/10.1016/j.smim.2007.11.003

Barheine, S., Hayakawa, S., Jäger, C., Shirosaki, Y., Osaka, A., 2011. Effect of disordered structure of boron-containing calcium phosphates on their in vitro biodegradability. J. Am. Ceram. Soc. 94, 2656–2662. https://doi.org/10.1111/j.1551-2916.2011.04400.x

Başar, B., Tezcaner, A., Keskin, D., Evis, Z., 2010. Improvements in microstructural, mechanical, and biocompatibility properties of nano-sized hydroxyapatites doped with yttrium and fluoride. Ceram. Int. 36, 1633–1643. https://doi.org/10.1016/j.ceramint.2010.02.033

Bertoni, E., Bigi, A., Cojazzi, G., Gandolfi, M., Panzavolta, S., Roveri, N., 1998.

Nanocrystals of magnesium and fluoride substituted hydroxyapatite. J. Inorg. Biochem. 72, 29–35. https://doi.org/10.1016/S0162-0134(98)10058-2

Berzina-Cimdina, L., Borodajenko, N., 2012. Research of calcium phosphates using fourier transform infrared spectroscopy, in: Infrared Spectroscopy - Materials Science, Engineering and Technology. InTech. https://doi.org/10.5772/36942

Bigi, A., Boanini, E., Capuccini, C., Gazzano, M., 2007. Strontium-substituted hydroxyapatite nanocrystals. Inorganica Chim. Acta 360, 1009–1016. https://doi.org/10.1016/j.ica.2006.07.074

Bigi, A., Boanini, E., Gazzano, M., 2016. Ion substitution in biological and synthetic apatites, in: Biomineralization and Biomaterials. Elsevier, pp. 235–266. https://doi.org/10.1016/B978-1-78242-338-6.00008-9

Bigi, A., Falini, G., Foresti, E., Ripamonti, A., Gazzano, M., Roveri, N., 1993. Magnesium influence on hydroxyapatite crystallization. J. Inorg. Biochem. 49, 69–78. https://doi.org/10.1016/0162-0134(93)80049-F

Birmingham, E., Niebur, G., McHugh, P., Shaw, G., Barry, F., McNamara, L., 2012. Osteogenic differentiation of mesenchymal stem cells is regulated by osteocyte and osteoblast cells in a simplified bone niche. Eur. Cells Mater. 23, 13–27. https://doi.org/10.22203/eCM.v023a02

Bohner, M., 2000. Calcium orthophosphates in medicine: From ceramics to calcium phosphate cements. Injury 31, D37–D47. https://doi.org/10.1016/S0020-1383(00)80022-4

Bonjour, J.-P., Guéguen, L., Palacios, C., Shearer, M.J., Weaver, C.M., 2009. Minerals and vitamins in bone health: the potential value of dietary enhancement. Br. J. Nutr. 101, 1581–1596. https://doi.org/10.1017/S0007114509311721

Bose, S., Dasgupta, S., Tarafder, S., Bandyopadhyay, A., 2010. Microwave-processed nanocrystalline hydroxyapatite: Simultaneous enhancement of

mechanical and biological properties. Acta Biomater. 6, 3782–3790. https://doi.org/10.1016/j.actbio.2010.03.016

Bose, S., Fielding, G., Tarafder, S., Bandyopadhyay, A., 2013. Understanding of dopant-induced osteogenesis and angiogenesis in calcium phosphate ceramics. Trends Biotechnol. 31, 594–605. https://doi.org/10.1016/j.tibtech.2013.06.005

Bose, S., Roy, M., Bandyopadhyay, A., 2012. Recent advances in bone tissue engineering scaffolds. Trends Biotechnol. 30, 546–554. https://doi.org/10.1016/j.tibtech.2012.07.005

Brown, R.F., Rahaman, M.N., Dwilewicz, A.B., Huang, W., Day, D.E., Li, Y., Bal, B.S., 2009. Effect of borate glass composition on its conversion to hydroxyapatite and on the proliferation of MC3T3-E1 cells. J. Biomed. Mater. Res. Part A 88A, 392–400. https://doi.org/10.1002/jbm.a.31679

Cabrera, W.E., Schrooten, I., De Broe, M.E., D'Haese, P.C., 1999. Strontium and bone. J. Bone Miner. Res. 14, 661–668. https://doi.org/10.1359/jbmr.1999.14.5.661

Cacciotti, I., Bianco, A., Lombardi, M., Montanaro, L., 2009. Mg-substituted hydroxyapatite nanopowders: Synthesis, thermal stability and sintering behaviour. J. Eur. Ceram. Soc. 29, 2969–2978. https://doi.org/10.1016/j.jeurceramsoc.2009.04.038

Callister Jr, W.D., 2000. Materials Science and Engineering - An Introduction (5th ed.). Anti-Corrosion Methods Mater. 47. https://doi.org/10.1108/acmm.2000.12847aae.001

Canalis, E., 1996. The divalent strontium salt S12911 enhances bone cell replication and bone formation in vitro. Bone 18, 517–523. https://doi.org/10.1016/8756-3282(96)00080-4

Capuccini, C., Torricelli, P., Boanini, E., Gazzano, M., Giardino, R., Bigi, A., 2009. Interaction of Sr-doped hydroxy apatite nanocrystals with osteoclast and

osteoblast-like cells. J. Biomed. Mater. Res. - Part A 89, 594–600. https://doi.org/10.1002/jbm.a.31975

Chang, K.-Y., Cheng, L.-W., Ho, G.-H., Huang, Y.-P., Lee, Y.-D., 2009. Fabrication and characterization of poly(γ-glutamic acid)-graft-chondroitin sulfate/polycaprolactone porous scaffolds for cartilage tissue engineering. Acta Biomater. 5, 1937–1947. https://doi.org/10.1016/j.actbio.2009.02.002

Chau, K.T., Wei, X.X., 2001. A new analytic solution for the diametral point load strength test on finite solid circular cylinders. Int. J. Solids Struct. 38, 1459–1481. https://doi.org/10.1016/S0020-7683(00)00122-0

Chen, H., Sun, K., Tang, Z., Law, R. V., Mansfield, J.F., Czajka-Jakubowska, A., Clarkson, B.H., 2006. Synthesis of fluorapatite nanorods and nanowires by direct precipitation from solution. Cryst. Growth Des. 6, 1504–1508. https://doi.org/10.1021/cg0600086

Chen, L., Mccrate, J.M., Lee, J.C.M., Li, H., 2011. The role of surface charge on the uptake and biocompatibility of hydroxyapatite nanoparticles with osteoblast cells. Nanotechnology 22, 105708. https://doi.org/10.1088/0957-4484/22/10/105708

Choi, W.-Y., Kim, H.-E., Koh, Y.-H., 2013. Production, mechanical properties and in vitro biocompatibility of highly aligned porous poly(ε-caprolactone) (PCL)/hydroxyapatite (HA) scaffolds. J. Porous Mater. 20, 701–708. https://doi.org/10.1007/s10934-012-9644-4

Chong, E.J., Phan, T.T., Lim, I.J., Zhang, Y.Z., Bay, B.H., Ramakrishna, S., Lim, C.T., 2007. Evaluation of electrospun PCL/gelatin nanofibrous scaffold for wound healing and layered dermal reconstitution. Acta Biomater. 3, 321–30. https://doi.org/10.1016/j.actbio.2007.01.002

Çiftci Dede, E., Korkusuz, P., Bilgiç, E., Çetinkaya, M.A., Korkusuz, F., 2021. Boron nano-hydroxyapatite composite increases the bone regeneration of ovariectomized rabbit femurs. Biol. Trace Elem. Res. 1–14.

https://doi.org/10.1007/s12011-021-02626-0

Çiftci, E., Köse, S., Korkusuz, P., Timuçin, M., Korkusuz, F., 2014. Boron containing nano hydroxyapatites (B-n-HAp) stimulate mesenchymal stem cell adhesion, proliferation and differentiation. Key Eng. Mater. 631, 373–378. https://doi.org/10.4028/www.scientific.net/KEM.631.373

Coulombe, J., Faure, H., Robin, B., Ruat, M., 2004. In vitro effects of strontium ranelate on the extracellular calcium-sensing receptor. Biochem. Biophys. Res. Commun. 323, 1184–1190. https://doi.org/10.1016/j.bbrc.2004.08.209

Curran, D.J., Fleming, T.J., Towler, M.R., Hampshire, S., 2011. Mechanical parameters of strontium doped hydroxyapatite sintered using microwave and conventional methods. J. Mech. Behav. Biomed. Mater. 4, 2063–2073. https://doi.org/10.1016/j.jmbbm.2011.07.005

Dahlin, C., Johansson, A., Hoffman, M., Molenberg, A., 2014. Early biocompatibility of poly (ethylene glycol) hydrogel barrier materials for guided bone regeneration. An in vitro study using human gingival fibroblasts (HGF-1). Clin. Oral Implants Res. 25, 16–20. https://doi.org/10.1111/clr.12076

Dasgupta, S., Banerjee, S.S., Bandyopadhyay, A., Bose, S., 2010. Zn- and Mg-doped hydroxyapatite nanoparticles for controlled release of protein. Langmuir 26, 4958–4964. https://doi.org/10.1021/la903617e

Dorozhkin, S., 2009. Calcium orthophosphates in nature, Biology and Medicine. Materials (Basel). 2, 399–498. https://doi.org/10.3390/ma2020399

Ehret, C., Aid-Launais, R., Sagardoy, T., Siadous, R., Bareille, R., Rey, S., Pechev, S., Etienne, L., Kalisky, J., de Mones, E., Letourneur, D., Amedee Vilamitjana, J., 2017. Strontium-doped hydroxyapatite polysaccharide materials effect on ectopic bone formation. PLoS One 12, e0184663. https://doi.org/10.1371/journal.pone.0184663

Erdemli, O., Çaptug, O., Bilgili, H., Orhan, D., Tezcaner, A., Keskin, D., 2010. In

vitro and in vivo evaluation of the effects of demineralized bone matrix or calcium sulfate addition to polycaprolactone–bioglass composites. J. Mater. Sci. Mater. Med. 21, 295–308. https://doi.org/10.1007/s10856-009-3862-6

Evis, Z., Öztürk, F., 2008. Investigation of tensile strength of hydroxyapatite with various porosities by diametral strength test. Mater. Sci. Technol. 24, 474–478. https://doi.org/10.1179/174328408X278439

Evis, Z., Webster, T.J., 2011. Nanosize hydroxyapatite: Doping with various ions. Adv. Appl. Ceram. 110, 311–321. https://doi.org/10.1179/1743676110Y.0000000005

Fadeev, I. V., Shvorneva, L.I., Barinov, S.M., Orlovskii, V.P., 2003. Synthesis and structure of magnesium-substituted hydroxyapatite. Inorg. Mater. 39, 947–950. https://doi.org/10.1023/A:1025509305805

Famery, R., Richard, N., Boch, P., 1994. Preparation of α- and β-tricalcium phosphate ceramics, with and without magnesium addition. Ceram. Int. 20, 327–336. https://doi.org/10.1016/0272-8842(94)90050-7

Farzadi, A., Bakhshi, F., Solati-Hashjin, M., Asadi-Eydivand, M., Osman, N.A.A., 2014. Magnesium incorporated hydroxyapatite: Synthesis and structural properties characterization. Ceram. Int. 40, 6021–6029. https://doi.org/10.1016/j.ceramint.2013.11.051

Farzadi, A., Solati-Hashjin, M., Bakhshi, F., Aminian, A., 2011. Synthesis and characterization of hydroxyapatite/β-tricalcium phosphate nanocomposites using microwave irradiation. Ceram. Int. 37, 65–71. https://doi.org/10.1016/j.ceramint.2010.08.021

Feng, P., Peng, S., Shuai, C., Gao, C., Yang, W., Bin, S., Min, A., 2020. In situ generation of hydroxyapatite on biopolymer particles for fabrication of bone scaffolds owning bioactivity. ACS Appl. Mater. Interfaces 12, 46743–46755. https://doi.org/10.1021/acsami.0c13768

Feng, R., Song, Z., Zhai, G., 2012. Preparation and in vivo pharmacokinetics of curcumin-loaded PCL-PEG-PCL triblock copolymeric nanoparticles. Int. J. Nanomedicine 7, 4089–4098. https://doi.org/10.2147/IJN.S33607

Frasnelli, M., Cristofaro, F., Sglavo, V.M., Dirè, S., Callone, E., Ceccato, R., Bruni, G., Cornaglia, A.I., Visai, L., 2017. Synthesis and characterization of strontium-substituted hydroxyapatite nanoparticles for bone regeneration. Mater. Sci. Eng. C 71, 653–662. https://doi.org/10.1016/j.msec.2016.10.047

Fu, H., Fu, Q., Zhou, N., Huang, W., Rahaman, M.N., Wang, D., Liu, X., 2009. In vitro evaluation of borate-based bioactive glass scaffolds prepared by a polymer foam replication method. Mater. Sci. Eng. C 29, 2275–2281. https://doi.org/10.1016/j.msec.2009.05.013

Fu, S., Wang, X., Guo, G., Shi, S., Liang, H., Luo, F., Wei, Y., Qian, Z., 2010. Preparation and characterization of nano-hydroxyapatite/poly(ε-caprolactone)−poly(ethylene glycol)−poly(ε-caprolactone) composite fibers for tissue engineering. J. Phys. Chem. C 114, 18372–18378. https://doi.org/10.1021/jp106488t

Fuh, L.-J., Huang, Y.-J., Chen, W.-C., Lin, D.-J., 2017. Preparation of micro-porous bioceramic containing silicon-substituted hydroxyapatite and beta-tricalcium phosphate. Mater. Sci. Eng. C 75, 798–806. https://doi.org/10.1016/j.msec.2017.02.065

Gao, J., Wang, M., Shi, C., Wang, L., Zhu, Y., Wang, D., 2017. A facile green synthesis of trace Si, Sr and F multi-doped hydroxyapatite with enhanced biocompatibility and osteoconduction. Mater. Lett. 196, 406–409. https://doi.org/10.1016/j.matlet.2017.03.054

Gaucher, G., Dufresne, M.-H., Sant, V.P., Kang, N., Maysinger, D., Leroux, J.-C., 2005. Block copolymer micelles: preparation, characterization and application in drug delivery. J. Control. Release 109, 169–188. https://doi.org/10.1016/j.jconrel.2005.09.034

Gautam, S., Dinda, A.K., Mishra, N.C., 2013. Fabrication and characterization of PCL/gelatin composite nanofibrous scaffold for tissue engineering applications by electrospinning method. Mater. Sci. Eng. C 33, 1228–1235. https://doi.org/10.1016/j.msec.2012.12.015

Geng, Z., Cui, Z., Li, Z., Zhu, S., Liang, Y., Liu, Y., Li, X., He, X., Yu, X., Wang, R., Yang, X., 2016. Strontium incorporation to optimize the antibacterial and biological characteristics of silver-substituted hydroxyapatite coating. Mater. Sci. Eng. C 58, 467–477. https://doi.org/10.1016/j.msec.2015.08.061

Geng, Z., Cui, Z., Li, Z., Zhu, S., Liang, Y., Lu, W.W., Yang, X., 2015. Synthesis, characterization and the formation mechanism of magnesium- and strontium-substituted hydroxyapatite. J. Mater. Chem. B 3, 3738–3746. https://doi.org/10.1039/C4TB02148G

Gentile, P., Mattioli-Belmonte, M., Chiono, V., Ferretti, C., Baino, F., Tonda-Turo, C., Vitale-Brovarone, C., Pashkuleva, I., Reis, R.L., Ciardelli, G., 2012. Bioactive glass/polymer composite scaffolds mimicking bone tissue. J. Biomed. Mater. Res. Part A 100A, 2654–2667. https://doi.org/10.1002/jbm.a.34205

Gentleman, E., Fredholm, Y.C., Jell, G., Lotfibakhshaiesh, N., O'Donnell, M.D., Hill, R.G., Stevens, M.M., 2010. The effects of strontium-substituted bioactive glasses on osteoblasts and osteoclasts in vitro. Biomaterials 31, 3949–3956. https://doi.org/10.1016/j.biomaterials.2010.01.121

Giacovazzo, C., Monaco, H.L., Artioli, G., Viterbo, D., Milanesio, M., Gilli, G., Gilli, P., Zanotti, G., Ferraris, G., Catti, M., 2013. Fundamentals of Crystallography, Third. ed, Fundamentals of Crystallography. Oxford University Press. https://doi.org/10.1093/acprof:oso/9780199573653.001.0001

Gloria, A., De Santis, R., Ambrosio, L., 2010. Polymer-based composite scaffolds for tissue engineering. J. Appl. Biomater. Biomech. 8, 57–67. https://doi.org/10.1177/228080001000800201

Goh, Y.-F., Alshemary, A.Z., Akram, M., Abdul Kadir, M.R., Hussain, R., 2014.

Bioactive glass: An in-vitro comparative study of doping with nanoscale copper and silver particles. Int. J. Appl. Glas. Sci. 5, 255–266. https://doi.org/10.1111/ijag.12061

Göpferich, A., 1996. Mechanisms of polymer degradation and erosion. Biomaterials 17, 103–114. https://doi.org/10.1016/0142-9612(96)85755-3

Gopi, D., Ramya, S., Rajeswari, D., Karthikeyan, P., Kavitha, L., 2014a. Strontium, cerium co-substituted hydroxyapatite nanoparticles: Synthesis, characterization, antibacterial activity towards prokaryotic strains and in vitro studies. Colloids Surfaces A Physicochem. Eng. Asp. 451, 172–180. https://doi.org/10.1016/j.colsurfa.2014.03.035

Gopi, D., Shinyjoy, E., Kavitha, L., 2014b. Synthesis and spectral characterization of silver/magnesium co-substituted hydroxyapatite for biomedical applications. Spectrochim. Acta Part A Mol. Biomol. Spectrosc. 127, 286–291. https://doi.org/10.1016/j.saa.2014.02.057

Grubova, I.Y., Surmeneva, M.A., Ivanova, A.A., Kravchuk, K., Prymak, O., Epple, M., Buck, V., Surmenev, R.A., 2015. The effect of patterned titanium substrates on the properties of silver-doped hydroxyapatite coatings. Surf. Coatings Technol. 276, 595–601. https://doi.org/10.1016/j.surfcoat.2015.06.010

Gu, Y.W., Khor, K.A., Cheang, P., 2004. Bone-like apatite layer formation on hydroxyapatite prepared by spark plasma sintering (SPS). Biomaterials 25, 4127–4134. https://doi.org/10.1016/j.biomaterials.2003.11.030

Güler, H., Gündoğmaz, G., Kurtuluş, F., Çelik, G., Gacanoğlu, Ş.S., 2011. Solid state synthesis of calcium borohydroxyapatite. Solid State Sci. 13, 1916–1920. https://doi.org/10.1016/j.solidstatesciences.2011.08.016

Guo, D., Xu, K., Zhao, X., Han, Y., 2005. Development of a strontium-containing hydroxyapatite bone cement. Biomaterials 26, 4073–4083. https://doi.org/10.1016/j.biomaterials.2004.10.032

Habibovic, P., Barralet, J.E., 2011. Bioinorganics and biomaterials: Bone repair. Acta Biomater. 7, 3013–3026. https://doi.org/10.1016/j.actbio.2011.03.027

Hakkı, S.S., Bozkurt, B.S., Hakkı, E.E., 2010. Boron regulates mineralized tissue-associated proteins in osteoblasts (MC3T3-E1). J. Trace Elem. Med. Biol. 24, 243–250. https://doi.org/10.1016/j.jtemb.2010.03.003

Hayakawa, S., Sakai, A., Tsuru, K., Osaka, A., Fujii, E., Kawabata, K., Jaeger, C., 2007. Preparation and characterization of boron-containing hydroxyapatite. Key Eng. Mater. 361–363, 191–194. https://doi.org/10.4028/www.scientific.net/KEM.361-363.191

He, L., Dong, G., Deng, C., 2016. Effects of strontium substitution on the phase transformation and crystal structure of calcium phosphate derived by chemical precipitation. Ceram. Int. 42, 11918–11923. https://doi.org/10.1016/j.ceramint.2016.04.116

Heidenau, F., Mittelmeier, W., Detsch, R., Haenle, M., Stenzel, F., Ziegler, G., Gollwitzer, H., 2005. A novel antibacterial titania coating: Metal ion toxicity and in vitro surface colonization. J. Mater. Sci. Mater. Med. 16, 883–888. https://doi.org/10.1007/s10856-005-4422-3

Heo, S.-J., Kim, S.-E., Wei, J., Hyun, Y.-T., Yun, H.-S., Kim, D.-H., Shin, J.W., Shin, J.-W., 2009. Fabrication and characterization of novel nano- and micro-HA/PCL composite scaffolds using a modified rapid prototyping process. J. Biomed. Mater. Res. A 89, 108–16. https://doi.org/10.1002/jbm.a.31726

Herliansyah, M.K., Hamdi, M., Ide-Ektessabi, A., Wildan, M.W., Toque, J.A., 2009. The influence of sintering temperature on the properties of compacted bovine hydroxyapatite. Mater. Sci. Eng. C 29, 1674–1680. https://doi.org/10.1016/j.msec.2009.01.007

Heshmatpour, F., Lashteneshaee, S.H., Samadipour, M., 2018. Study of in vitro bioactivity of nano hydroxyapatite composites doped by various cations. J. Inorg. Organomet. Polym. Mater. 28, 2063–2068.

https://doi.org/10.1007/s10904-018-0864-1

Hing, K.A., Best, S.M., Bonfield, W., 1999. Characterization of porous hydroxyapatite. J. Mater. Sci. Mater. Med. 10, 135–145. https://doi.org/10.1023/A:1008929305897

Huang, M.-H., Li, S., Coudane, J., Vert, M., 2003. Synthesis and characterization of block copolymers of ε-caprolactone and DL-lactide initiated by ethylene glycol or poly(ethylene glycol). Macromol. Chem. Phys. 204, 1994–2001. https://doi.org/10.1002/macp.200350054

İpekoglu, M., Altıntaş, S., 2009. Synthesis of nanosized calcium deficient hydroxyapatite by microwave, in: 2009 14th National Biomedical Engineering Meeting. IEEE, pp. 1–4. https://doi.org/10.1109/BIYOMUT.2009.5130361

Jimi, E., Hirata, S., Osawa, K., Terashita, M., Kitamura, C., Fukushima, H., 2012. The current and future therapies of bone regeneration to repair bone defects. Int. J. Dent. 2012, 1–7. https://doi.org/10.1155/2012/148261

Jodati, H., Yılmaz, B., Evis, Z., 2020. A review of bioceramic porous scaffolds for hard tissue applications: Effects of structural features. Ceram. Int. 46, 15725–15739. https://doi.org/10.1016/j.ceramint.2020.03.192

Kaito, T., Myoui, A., Takaoka, K., Saito, N., Nishikawa, M., Tamai, N., Ohgushi, H., Yoshikawa, H., 2005. Potentiation of the activity of bone morphogenetic protein-2 in bone regeneration by a PLA–PEG/hydroxyapatite composite. Biomaterials 26, 73–79. https://doi.org/10.1016/j.biomaterials.2004.02.010

Kalita, S.J., Bhardwaj, A., Bhatt, H.A., 2007. Nanocrystalline calcium phosphate ceramics in biomedical engineering. Mater. Sci. Eng. C 27, 441–449. https://doi.org/10.1016/j.msec.2006.05.018

Kalita, S.J., Bhatt, H.A., 2007. Nanocrystalline hydroxyapatite doped with magnesium and zinc: Synthesis and characterization. Mater. Sci. Eng. C 27, 837–848. https://doi.org/10.1016/j.msec.2006.09.036

Kannan, S., Ferreira, J.M.F., 2006. Synthesis and thermal stability of hydroxyapatite−β-tricalcium phosphate composites with cosubstituted sodium, magnesium, and fluorine. Chem. Mater. 18, 198–203. https://doi.org/10.1021/cm051966i

Karageorgiou, V., Kaplan, D., 2005. Porosity of 3D biomaterial scaffolds and osteogenesis. Biomaterials 26, 5474–91. https://doi.org/10.1016/j.biomaterials.2005.02.002

Kashte, S., Jaiswal, A.K., Kadam, S., 2017. Artificial bone via bone tissue engineering: Current scenario and challenges. Tissue Eng. Regen. Med. 14, 1–14. https://doi.org/10.1007/s13770-016-0001-6

Kaygılı, O., Keser, S., Kom, M., Eroksuz, Y., Dorozhkin, S. V., Ates, T., Ozercan, I.H., Tatar, C., Yakuphanoglu, F., 2015. Strontium substituted hydroxyapatites: Synthesis and determination of their structural properties, in vitro and in vivo performance. Mater. Sci. Eng. C 55, 538–546. https://doi.org/10.1016/j.msec.2015.05.081

Ke, D., Vu, A.A., Bandyopadhyay, A., Bose, S., 2019. Compositionally graded doped hydroxyapatite coating on titanium using laser and plasma spray deposition for bone implants. Acta Biomater. 84, 414–423. https://doi.org/10.1016/j.actbio.2018.11.041

Kheradmandfard, M., Fathi, M.H., 2013. Fabrication and characterization of nanocrystalline Mg-substituted fluorapatite by high energy ball milling. Ceram. Int. 39, 1651–1658. https://doi.org/10.1016/j.ceramint.2012.08.007

Kim, H.-K., Han, H.-S., Lee, K.-S., Lee, D.-H., Lee, J.W., Jeon, H., Cho, S.-Y., Roh, H.-J., Kim, Y.-C., Seok, H.-K., 2017. Comprehensive study on the roles of released ions from biodegradable Mg-5 wt% Ca-1 wt% Zn alloy in bone regeneration. J. Tissue Eng. Regen. Med. 11, 2710–2724. https://doi.org/10.1002/term.2166

Kim, S.-S., Sun Park, M., Jeon, O., Yong Choi, C., Kim, B.-S., 2006. Poly(lactide-

co-glycolide)/hydroxyapatite composite scaffolds for bone tissue engineering. Biomaterials 27, 1399–1409. https://doi.org/10.1016/j.biomaterials.2005.08.016

Kim, S., 2003. Synthesis of Si, Mg substituted hydroxyapatites and their sintering behaviors. Biomaterials 24, 1389–1398. https://doi.org/10.1016/S0142-9612(02)00523-9

Kim, Y.B., Kim, G.H., 2015. PCL/alginate composite scaffolds for hard tissue engineering: Fabrication, characterization, and cellular activities. ACS Comb. Sci. 17, 87–99. https://doi.org/10.1021/co500033h

Kıvrak, N., Taş, A.C., 2005. Synthesis of calcium hydroxyapatite-tricalcium phosphate (HA-TCP) composite bioceramic powders and their sintering behavior. J. Am. Ceram. Soc. 81, 2245–2252. https://doi.org/10.1111/j.1151-2916.1998.tb02618.x

Knop, K., Hoogenboom, R., Fischer, D., Schubert, U.S., 2010. Poly(ethylene glycol) in drug delivery: Pros and cons as well as potential alternatives. Angew. Chem. Int. Ed. Engl. 49, 6288–308. https://doi.org/10.1002/anie.200902672

Knudsen, F.P., 1959. Dependence of mechanical strength of brittle polycrystalline specimens on porosity and grain size. J. Am. Ceram. Soc. 42, 376–387. https://doi.org/10.1111/j.1151-2916.1959.tb13596.x

Koh, Y.-H., Jun, I.-K., Kim, H.-E., 2006. Fabrication of poly(ε-caprolactone)/hydroxyapatite scaffold using rapid direct deposition. Mater. Lett. 60, 1184–1187. https://doi.org/10.1016/j.matlet.2005.10.103

Kohane, D.S., Langer, R., 2008. Polymeric biomaterials in tissue engineering. Pediatr. Res. 63, 487–491. https://doi.org/10.1203/01.pdr.0000305937.26105.e7

Kokubo, T., Takadama, H., 2006. How useful is SBF in predicting in vivo bone bioactivity? Biomaterials 27, 2907–2915.

https://doi.org/10.1016/j.biomaterials.2006.01.017

Kolmas, J., Velard, F., Jaguszewska, A., Lemaire, F., Kerdjoudj, H., Gangloff, S.C., Kaflak, A., 2017. Substitution of strontium and boron into hydroxyapatite crystals: Effect on physicochemical properties and biocompatibility with human Wharton-Jelly stem cells. Mater. Sci. Eng. C 79, 638–646. https://doi.org/10.1016/j.msec.2017.05.066

Komlev, V.S., Barinov, S.M., Rustichelli, F., 2003. Strength enhancement of porous hydroxyapatite ceramics by polymer impregnation. J. Mater. Sci. Lett. 22, 1215–1217. https://doi.org/10.1023/A:1025300617681

Kulanthaivel, S., Mishra, U., Agarwal, T., Giri, S., Pal, K., Pramanik, K., Banerjee, I., 2015. Improving the osteogenic and angiogenic properties of synthetic hydroxyapatite by dual doping of bivalent cobalt and magnesium ion. Ceram. Int. 41, 11323–11333. https://doi.org/10.1016/j.ceramint.2015.05.090

Kutikov, A.B., Song, J., 2013. An amphiphilic degradable polymer/hydroxyapatite composite with enhanced handling characteristics promotes osteogenic gene expression in bone marrow stromal cells. Acta Biomater. 9, 8354–8364. https://doi.org/10.1016/j.actbio.2013.06.013

Landi, E., Logroscino, G., Proietti, L., Tampieri, A., Sandri, M., Sprio, S., 2008. Biomimetic Mg-substituted hydroxyapatite: From synthesis to in vivo behaviour. J. Mater. Sci. Mater. Med. 19, 239–247. https://doi.org/10.1007/s10856-006-0032-y

Laurencin, D., Almora-Barrios, N., de Leeuw, N.H., Gervais, C., Bonhomme, C., Mauri, F., Chrzanowski, W., Knowles, J.C., Newport, R.J., Wong, A., Gan, Z., Smith, M.E., 2011. Magnesium incorporation into hydroxyapatite. Biomaterials 32, 1826–1837. https://doi.org/10.1016/j.biomaterials.2010.11.017

Lee, J.-M., Choi, B.B.R., Choi, J.-H., Kim, G.-C., Hwang, D.-S., Chang, M.C., Byun, J.-H., Kim, U.-K., 2013. Osteoblastic response to the hydroxyapatite/gelatin nanocomposite and bio-calcium phosphate cement. Tissue Eng. Regen. Med.

10, 47–52. https://doi.org/10.1007/s13770-013-0344-1

LeGeros, R.Z., 1988. Calcium phosphate materials in restorative dentistry: A review. Adv. Dent. Res. 2, 164–80. https://doi.org/10.1177/08959374880020011101

Liao, C.-J., Lin, F.-H., Chen, K.-S., Sun, J.-S., 1999. Thermal decomposition and reconstitution of hydroxyapatite in air atmosphere. Biomaterials 20, 1807–1813. https://doi.org/10.1016/S0142-9612(99)00076-9

Lin, Z., Cao, S., Chen, X., Wu, W., Li, J., 2013. Thermoresponsive hydrogels from phosphorylated ABA triblock copolymers: A potential scaffold for bone tissue engineering. Biomacromolecules 14, 2206–2214. https://doi.org/10.1021/bm4003442

Liu, C.B., Gong, C.Y., Huang, M.J., Wang, J.W., Pan, Y.F., Zhang, Y. De, Li, G.Z., Gou, M.L., Wang, K., Tu, M.J., Wei, Y.Q., Qian, Z.Y., 2008. Thermoreversible gel–sol behavior of biodegradable PCL-PEG-PCL triblock copolymer in aqueous solutions. J. Biomed. Mater. Res. Part B Appl. Biomater. 84B, 165–175. https://doi.org/10.1002/jbm.b.30858

Long, T., Yang, J., Shi, S.S., Guo, Y.P., Ke, Q.F., Zhu, Z.A., 2015. Fabrication of three-dimensional porous scaffold based on collagen fiber and bioglass for bone tissue engineering. J. Biomed. Mater. Res. - Part B Appl. Biomater. 103, 1455–1464. https://doi.org/10.1002/jbm.b.33328

Lozzi, I., Pucci, A., Pantani, O.L., D'Acqui, L.P., Calamai, L., 2008. Interferences of suspended clay fraction in protein quantitation by several determination methods. Anal. Biochem. 376, 108–114. https://doi.org/10.1016/j.ab.2008.01.040

Lu, J., Wei, J., Yan, Y., Li, H., Jia, J., Wei, S., Guo, H., Xiao, T., Liu, C., 2011. Preparation and preliminary cytocompatibility of magnesium doped apatite cement with degradability for bone regeneration. J. Mater. Sci. Mater. Med. 22, 607–615. https://doi.org/10.1007/s10856-011-4228-4

Lusvardi, G., Menabue, L., Saladini, M., 2002. Reactivity of biological and synthetic hydroxyapatite towards ZN(II) ion, solid-liquid investigations. J. Mater. Sci. Mater. Med. 13, 91–98. https://doi.org/10.1023/A:1013655123340

Ma, G., Miao, B., Song, C., 2010. Thermosensitive PCL-PEG-PCL hydrogels: Synthesis, characterization, and delivery of proteins. J. Appl. Polym. Sci. 116, 1985–1993. https://doi.org/10.1002/app.31654

Makadia, H.K., Siegel, S.J., 2011. Poly lactic-co-glycolic acid (PLGA) as biodegradable controlled drug delivery carrier. Polymers (Basel). 3, 1377–1397. https://doi.org/10.3390/polym3031377

Manjili, H.K., Sharafi, A., Danafar, H., Hosseini, M., Ramazani, A., Ghasemi, M.H., 2016. Poly(caprolactone)–poly(ethylene glycol)–poly(caprolactone) (PCL–PEG–PCL) nanoparticles: A valuable and efficient system for in vitro and in vivo delivery of curcumin. RSC Adv. 6, 14403–14415. https://doi.org/10.1039/C5RA24942B

Mardziah, C.M., Sopyan, I., Ramesh, S., 2009. Strontium-doped hydroxyapatite nanopowder via sol-gel method: Effect of strontium concentration and calcination temperature on phase behavior. Trends Biomater. Artif. Organs 23, 105–113.

Marie, P.J., Ammann, P., Boivin, G., Rey, C., 2001. Mechanisms of action and therapeutic potential of strontium in bone. Calcif. Tissue Int. 69, 121–129. https://doi.org/10.1007/s002230010055

Marques, C.F., Matos, A.C., Ribeiro, I.A.C., Gonçalves, L.M., Bettencourt, A., Ferreira, J.M.F., 2016. Insights on the properties of levofloxacin-adsorbed Sr- and Mg-doped calcium phosphate powders. J. Mater. Sci. Mater. Med. 27, 123. https://doi.org/10.1007/s10856-016-5733-2

Massera, J., Shpotyuk, Y., Sabatier, F., Jouan, T., Boussard-Plédel, C., Roiland, C., Bureau, B., Petit, L., Boetti, N.G., Milanese, D., Hupa, L., 2015. Processing and characterization of novel borophosphate glasses and fibers for medical

applications. J. Non. Cryst. Solids 425, 52–60. https://doi.org/10.1016/j.jnoncrysol.2015.05.028

Mazón, P., De Aza, P.N., 2018. Porous scaffold prepared from α′L-Dicalcium silicate doped with phosphorus for bone grafts. Ceram. Int. 44, 537–545. https://doi.org/10.1016/j.ceramint.2017.09.208

Meejoo, S., Maneeprakorn, W., Winotai, P., 2006. Phase and thermal stability of nanocrystalline hydroxyapatite prepared via microwave heating. Thermochim. Acta 447, 115–120. https://doi.org/10.1016/j.tca.2006.04.013

Meunier, P.J., 2002. Strontium ranelate: Dose-dependent effects in established postmenopausal vertebral osteoporosis--A 2-year randomized placebo controlled trial. J. Clin. Endocrinol. Metab. 87, 2060–2066. https://doi.org/10.1210/jc.87.5.2060

Miao, X., Lim, W.-K.K., Huang, X., Chen, Y., 2005. Preparation and characterization of interpenetrating phased TCP/HA/PLGA composites. Mater. Lett. 59, 4000–4005. https://doi.org/10.1016/j.matlet.2005.07.062

Mishra, G.P., Tamboli, V., Mitra, A.K., 2011. Effect of hydrophobic and hydrophilic additives on sol-gel transition and release behavior of timolol maleate from polycaprolactone-based hydrogel. Colloid Polym. Sci. 289, 1553–1562. https://doi.org/10.1007/s00396-011-2476-y

Molino, G., Bari, A., Baino, F., Fiorilli, S., Vitale-Brovarone, C., 2017. Electrophoretic deposition of spray-dried Sr-containing mesoporous bioactive glass spheres on glass–ceramic scaffolds for bone tissue regeneration. J. Mater. Sci. 52, 9103–9114. https://doi.org/10.1007/s10853-017-1026-5

Muralithran, G., Ramesh, S., 2000. The effects of sintering temperature on the properties of hydroxyapatite. Ceram. Int. 26, 221–230. https://doi.org/10.1016/S0272-8842(99)00046-2

Nair, L.S., Laurencin, C.T., 2007. Biodegradable polymers as biomaterials. Prog.

Polym. Sci. 32, 762–798. https://doi.org/10.1016/j.progpolymsci.2007.05.017

Ni, G.X., Lu, W.W., Xu, B., Chiu, K.Y., Yang, C., Li, Z.Y., Lam, W.M., Luk, K.D.K., 2006. Interfacial behaviour of strontium-containing hydroxyapatite cement with cancellous and cortical bone. Biomaterials 27, 5127–5133. https://doi.org/10.1016/j.biomaterials.2006.05.030

Nicolais, L., Gloria, A., Ambrosio, L., 2010. The mechanics of biocomposites, in: Biomedical Composites. Elsevier, pp. 411–440. https://doi.org/10.1533/9781845697372.3.411

Niu, Y., Dong, W., Guo, H., Deng, Y., Guo, L., An, X., He, D., Wei, J., Li, M., 2014. Mesoporous magnesium silicate-incorporated poly(ε-caprolactone)-poly(ethylene glycol)-poly(ε-caprolactone) bioactive composite beneficial to osteoblast behaviors. Int. J. Nanomedicine 9, 2665–75. https://doi.org/10.2147/IJN.S59040

Nuttelman, C.R., Tripodi, M.C., Anseth, K.S., 2005. Synthetic hydrogel niches that promote hMSC viability. Matrix Biol. 24, 208–218. https://doi.org/10.1016/j.matbio.2005.03.004

O'Donnell, M.D., Fredholm, Y., de Rouffignac, A., Hill, R.G., 2008. Structural analysis of a series of strontium-substituted apatites. Acta Biomater. 4, 1455–1464. https://doi.org/10.1016/j.actbio.2008.04.018

Ojansivu, M., Mishra, A., Vanhatupa, S., Juntunen, M., Larionova, A., Massera, J., Miettinen, S., 2018. The effect of S53P4-based borosilicate glasses and glass dissolution products on the osteogenic commitment of human adipose stem cells. PLoS One 13, e0202740. https://doi.org/10.1371/journal.pone.0202740

Özbek, Y.Y., Baştan, F.E., Üstel, F., 2016. Synthesis and characterization of strontium-doped hydroxyapatite for biomedical applications. J. Therm. Anal. Calorim. 125, 745–750. https://doi.org/10.1007/s10973-016-5607-3

Paiva, A.O., Duarte, M.G., Fernandes, M.H.V., Gil, M.H., Costa, N.G., 2006. In vitro

studies of bioactive glass/polyhydroxybutyrate composites. Mater. Res. 9, 417–423. https://doi.org/10.1590/S1516-14392006000400013

Park, H.J., Lee, O.J., Lee, M.C., Moon, B.M., Ju, H.W., Lee, J. min, Kim, J.-H., Kim, D.W., Park, C.H., 2015. Fabrication of 3D porous silk scaffolds by particulate (salt/sucrose) leaching for bone tissue reconstruction. Int. J. Biol. Macromol. 78, 215–223. https://doi.org/10.1016/j.ijbiomac.2015.03.064

Pattanayak, D.K., Dash, R., Prasad, R.C., Rao, B.T., Rama Mohan, T.R., 2007. Synthesis and sintered properties evaluation of calcium phosphate ceramics. Mater. Sci. Eng. C 27, 684–690. https://doi.org/10.1016/j.msec.2006.06.021

Pazarçeviren, A.E., Tezcaner, A., Keskin, D., Kolukısa, S.T., Sürdem, S., Evis, Z., 2021. Boron-doped biphasic hydroxyapatite/β-tricalcium phosphate for bone tissue engineering. Biol. Trace Elem. Res. 199, 968–980. https://doi.org/10.1007/s12011-020-02230-8

Pazarçeviren, E., Erdemli, Ö., Keskin, D., Tezcaner, A., 2017. Clinoptilolite/PCL-PEG-PCL composite scaffolds for bone tissue engineering applications. J. Biomater. Appl. 31, 1148–1168. https://doi.org/10.1177/0885328216680152

Piao, L., Dai, Z., Deng, M., Chen, X., Jing, X., 2003. Synthesis and characterization of PCL/PEG/PCL triblock copolymers by using calcium catalyst. Polymer (Guildf). 44, 2025–2031. https://doi.org/10.1016/S0032-3861(03)00087-9

Popa, C.L., Bartha, C.M., Albu, M., Guegan, R., Motelica-Heino, M., Chifiriuc, M.C., Bleotu, C., Badea, M.L., Antohe, S., 2015. Synthesis, characterization and cytotoxicity evaluation on zinc doped hydroxyapatite in collagen matrix. Dig. J. Nanomater. Biostructures 10, 681–691.

Price, C.T., Langford, J.R., Liporace, F.A., 2012. Essential nutrients for bone health and a review of their availability in the average north american diet. Open Orthop. J. 6, 143–149. https://doi.org/10.2174/1874325001206010143

Qi, G., Zhang, S., Khor, K.A., Lye, S.W., Zeng, X., Weng, W., Liu, C.,

Venkatraman, S.S., Ma, L.L., 2008. Osteoblastic cell response on magnesium-incorporated apatite coatings. Appl. Surf. Sci. 255, 304–307. https://doi.org/10.1016/j.apsusc.2008.06.106

Qiu, K., Zhao, X.J., Wan, C.X., Zhao, C.S., Chen, Y.W., 2006. Effect of strontium ions on the growth of ROS17/2.8 cells on porous calcium polyphosphate scaffolds. Biomaterials 27, 1277–1286. https://doi.org/10.1016/j.biomaterials.2005.08.006

Radovanović, Ž., Jokić, B., Veljović, D., Dimitrijević, S., Kojić, V., Petrović, R., Janaćković, D., 2014. Antimicrobial activity and biocompatibility of Ag+- and Cu2+-doped biphasic hydroxyapatite/α-tricalcium phosphate obtained from hydrothermally synthesized Ag+- and Cu2+-doped hydroxyapatite. Appl. Surf. Sci. 307, 513–519. https://doi.org/10.1016/j.apsusc.2014.04.066

Ramesh, S., Tan, C.Y., Hamdi, M., Sopyan, I., Teng, W.D., 2007. The influence of Ca/P ratio on the properties of hydroxyapatite bioceramics, in: International Conference on Smart Materials and Nanotechnology in Engineering. p. 64233A. https://doi.org/10.1117/12.779890

Rao, W.R., Boehm, R.F., 1974. A study of sintered apatites. J. Dent. Res. 53, 1351–1354. https://doi.org/10.1177/00220345740530061001

Ratisoontorn, C., Seto, M.L., Broughton, K.M., Cunningham, M.L., 2005. In vitro differentiation profile of osteoblasts derived from patients with Saethre–Chotzen syndrome. Bone 36, 627–634. https://doi.org/10.1016/j.bone.2005.01.010

Ratner, B.D., Johnston, A.B., Lenk, T.J., 1987. Biomaterial surfaces. J. Biomed. Mater. Res. 21, 59–90.

Ravi, N.D., Balu, R., Sampath Kumar, T.S., 2012. Strontium-substituted calcium deficient hydroxyapatite nanoparticles: synthesis, characterization, and antibacterial properties. J. Am. Ceram. Soc. 95, 2700–2708. https://doi.org/10.1111/j.1551-2916.2012.05262.x

Rezwan, K., Chen, Q.Z., Blaker, J.J., Boccaccini, A.R., 2006. Biodegradable and bioactive porous polymer/inorganic composite scaffolds for bone tissue engineering. Biomaterials 27, 3413–31. https://doi.org/10.1016/j.biomaterials.2006.01.039

Rice, R.W., 1997. Limitations of pore-stress concentrations on the mechanical properties of porous materials. J. Mater. Sci. 32, 4731–4736. https://doi.org/10.1023/A:1018674713006

Rodríguez-Valencia, C., López-Álvarez, M., Cochón-Cores, B., Pereiro, I., Serra, J., González, P., 2013. Novel selenium-doped hydroxyapatite coatings for biomedical applications. J. Biomed. Mater. Res. A 101, 853–61. https://doi.org/10.1002/jbm.a.34387

Roy, M., Bandyopadhyay, A., Bose, S., 2011. Induction plasma sprayed Sr and Mg doped nano hydroxyapatite coatings on Ti for bone implant. J. Biomed. Mater. Res. Part B Appl. Biomater. 99B, 258–265. https://doi.org/10.1002/jbm.b.31893

Roy, T.D., Simon, J.L., Ricci, J.L., Rekow, E.D., Thompson, V.P., Parsons, J.R., 2003. Performance of degradable composite bone repair products made via three-dimensional fabrication techniques. J. Biomed. Mater. Res. 66A, 283–291. https://doi.org/10.1002/jbm.a.10582

Rude, R.K., Gruber, H.E., 2004. Magnesium deficiency and osteoporosis: Animal and human observations. J. Nutr. Biochem. 15, 710–716. https://doi.org/10.1016/j.jnutbio.2004.08.001

Saghebasl, S., Davaran, S., Rahbarghazi, R., Montaseri, A., Salehi, R., Ramazani, A., 2018. Synthesis and in vitro evaluation of thermosensitive hydrogel scaffolds based on (PNIPAAm-PCL-PEG-PCL-PNIPAAm)/gelatin and (PCL-PEG-PCL)/gelatin for use in cartilage tissue engineering. J. Biomater. Sci. Polym. Ed. 29, 1185–1206. https://doi.org/10.1080/09205063.2018.1447627

Salma-Ancane, K., Stipniece, L., Borodajenko, N., Jakovlevs, D., Berzina-Cimdina,

L., 2012. Incorporation of magnesium ions into synthetic hydroxyapatite: Synthesis and characterization. Key Eng. Mater. 527, 26–31. https://doi.org/10.4028/www.scientific.net/KEM.527.26

Serra, T., Ortiz-Hernandez, M., Engel, E., Planell, J.A., Navarro, M., 2014. Relevance of PEG in PLA-based blends for tissue engineering 3D-printed scaffolds. Mater. Sci. Eng. C. Mater. Biol. Appl. 38, 55–62. https://doi.org/10.1016/j.msec.2014.01.003

Shimabayashi, S., Tamura, C., Nakagaki, M., 1981. Adsorption of mono- and divalent metal cations on hydroxyapatite in water. Chem. Pharm. Bull. 29, 2116–2122. https://doi.org/10.1248/cpb.29.2116

Shuai, C., Yang, W., Feng, P., Peng, S., Pan, H., 2021. Accelerated degradation of HAP/PLLA bone scaffold by PGA blending facilitates bioactivity and osteoconductivity. Bioact. Mater. 6, 490–502. https://doi.org/10.1016/j.bioactmat.2020.09.001

Siddiq, A.R., Kennedy, A.R., 2015. Porous poly-ether ether ketone (PEEK) manufactured by a novel powder route using near-spherical salt bead porogens: Characterization and mechanical properties. Mater. Sci. Eng. C 47, 180–188. https://doi.org/10.1016/j.msec.2014.11.044

Ślósarczyk, A., Paluszkiewicz, C., Gawlicki, M., Paszkiewicz, Z., 1997. The FTIR spectroscopy and QXRD studies of calcium phosphate based materials produced from the powder precursors with different ratios. Ceram. Int. 23, 297–304. https://doi.org/10.1016/S0272-8842(96)00016-8

Speirs, A.D., Oxland, T.R., Masri, B.A., Poursartip, A., Duncan, C.P., 2005. Calcium phosphate cement composites in revision hip arthroplasty. Biomaterials 26, 7310–7318. https://doi.org/10.1016/j.biomaterials.2005.05.062

Stanić, V., Dimitrijević, S., Antić-Stanković, J., Mitrić, M., Jokić, B., Plećaš, I.B., Raičević, S., 2010. Synthesis, characterization and antimicrobial activity of copper and zinc-doped hydroxyapatite nanopowders. Appl. Surf. Sci. 256,

6083–6089. https://doi.org/10.1016/j.apsusc.2010.03.124

Suchanek, W.L., Byrappa, K., Shuk, P., Riman, R.E., Janas, V.F., TenHuisen, K.S., 2004. Preparation of magnesium-substituted hydroxyapatite powders by the mechanochemical–hydrothermal method. Biomaterials 25, 4647–4657. https://doi.org/10.1016/j.biomaterials.2003.12.008

Suganthi, R.V., Elayaraja, K., Joshy, M.I.A., Chandra, V.S., Girija, E.K., Kalkura, S.N., 2011. Fibrous growth of strontium substituted hydroxyapatite and its drug release. Mater. Sci. Eng. C 31, 593–599. https://doi.org/10.1016/j.msec.2010.11.025

Sun, Z.P., Ercan, B., Evis, Z., Webster, T.J., 2010. Microstructural, mechanical, and osteocompatibility properties of Mg2+/F(-)-doped nanophase hydroxyapatite. J. Biomed. Mater. Res. A 94, 806–15. https://doi.org/10.1002/jbm.a.32745

Surmeneva, M.A., Chaikina, M. V., Zaikovskiy, V.I., Pichugin, V.F., Buck, V., Prymak, O., Epple, M., Surmenev, R.A., 2013. The structure of an RF-magnetron sputter-deposited silicate-containing hydroxyapatite-based coating investigated by high-resolution techniques. Surf. Coatings Technol. 218, 39–46. https://doi.org/10.1016/j.surfcoat.2012.12.023

Swetha, M., Sahithi, K., Moorthi, A., Srinivasan, N., Ramasamy, K., Selvamurugan, N., 2010. Biocomposites containing natural polymers and hydroxyapatite for bone tissue engineering. Int. J. Biol. Macromol. 47, 1–4. https://doi.org/10.1016/j.ijbiomac.2010.03.015

Tampieri, A., Celotti, G.C., Landi, E., Sandri, M., 2004. Magnesium doped hydroxyapatite: Synthesis and characterization. Key Eng. Mater. 264–268, 2051–2054. https://doi.org/10.4028/www.scientific.net/KEM.264-268.2051

Tan, C.Y., Singh, R., Teh, Y.C., Tan, Y.M., Yap, B.K., 2015. The effects of calcium-to-phosphorus ratio on the densification and mechanical properties of hydroxyapatite ceramic. Int. J. Appl. Ceram. Technol. 12, 223–227. https://doi.org/10.1111/ijac.12249

Tao, Z.-S., Zhou, W.-S., He, X.-W., Liu, W., Bai, B.-L., Zhou, Q., Huang, Z.-L., Tu, K., Li, H., Sun, T., Lv, Y.-X., Cui, W., Yang, L., 2016. A comparative study of zinc, magnesium, strontium-incorporated hydroxyapatite-coated titanium implants for osseointegration of osteopenic rats. Mater. Sci. Eng. C 62, 226–232. https://doi.org/10.1016/j.msec.2016.01.034

Ternane, R., Cohen-Adad, M.T., Panczer, G., Goutaudier, C., Kbir-Ariguib, N., Trabelsi-Ayedi, M., Florian, P., Massiot, D., 2002. Introduction of boron in hydroxyapatite: Synthesis and structural characterization. J. Alloys Compd. 333, 62–71. https://doi.org/10.1016/S0925-8388(01)01558-4

Terra, J., Dourado, E.R., Eon, J.G., Ellis, D.E., Gonzalez, G., Rossi, A.M., 2009. The structure of strontium-doped hydroxyapatite: An experimental and theoretical study. Phys. Chem. Chem. Phys. 11, 568–577. https://doi.org/10.1039/b802841a

Toledano-Osorio, M., Aguilera, F.S., Osorio, R., Muñoz-Soto, E., Pérez-Álvarez, M.C., López-López, M.T., Lynch, C.D., Toledano, M., 2020. Hydroxyapatite-based cements induce different apatite formation in radicular dentin. Dent. Mater. 36, 167–178. https://doi.org/10.1016/j.dental.2019.11.023

Tõnsuaadu, K., Gross, K.A., Plūduma, L., Veiderma, M., 2012. A review on the thermal stability of calcium apatites. J. Therm. Anal. Calorim. 110, 647–659. https://doi.org/10.1007/s10973-011-1877-y

Tunçay, E.Ö., Demirtaş, T.T., Gümüşderelioğlu, M., 2017. Microwave-induced production of boron-doped HAp (B-HAp) and B-HAp coated composite scaffolds. J. Trace Elem. Med. Biol. 40, 72–81. https://doi.org/10.1016/j.jtemb.2016.12.005

Türkkan, S., Pazarçeviren, A.E., Keskin, D., Machin, N.E., Duygulu, Ö., Tezcaner, A., 2017. Nanosized CaP-silk fibroin-PCL-PEG-PCL/PCL based bilayer membranes for guided bone regeneration. Mater. Sci. Eng. C 80, 484–493. https://doi.org/10.1016/j.msec.2017.06.016

Uysal, İ., Severcan, F., Evis, Z., 2013. Characterization by fourier transform infrared spectroscopy of hydroxyapatite co-doped with zinc and fluoride. Ceram. Int. 39, 7727–7733. https://doi.org/10.1016/j.ceramint.2013.03.029

Veljovic, D., Matic, T., Stamenic, T., Kojic, V., Dimitrijevic-Brankovic, S., Lukic, M.J., Jevtic, S., Radovanovic, Z., Petrovic, R., Janackovic, D., 2019. Mg/Cu co-substituted hydroxyapatite – Biocompatibility, mechanical properties and antimicrobial activity. Ceram. Int. https://doi.org/10.1016/j.ceramint.2019.07.219

Verberckmoes, S.C., De Broe, M.E., D'Haese, P.C., 2003. Dose-dependent effects of strontium on osteoblast function and mineralization. Kidney Int. 64, 534–543. https://doi.org/10.1046/j.1523-1755.2003.00123.x

Veronese, F.M., Pasut, G., 2005. PEGylation, successful approach to drug delivery. Drug Discov. Today 10, 1451–8. https://doi.org/10.1016/S1359-6446(05)03575-0

Vetalice, J.A., 2012. Orthopaedic Industry Annual Report - Focus on Joint Replacement. OrthoKnow.

Vijayan, S., Varma, H., 2002. Microwave sintering of nanosized hydroxyapatite powder compacts. Mater. Lett. 56, 827–831. https://doi.org/10.1016/S0167-577X(02)00622-5

Wang, C., Duan, Y., Markovic, B., Barbara, J., Rolfe Howlett, C., Zhang, X., Zreiqat, H., 2004. Proliferation and bone-related gene expression of osteoblasts grown on hydroxyapatite ceramics sintered at different temperature. Biomaterials 25, 2949–2956. https://doi.org/10.1016/j.biomaterials.2003.09.088

Wang, P.E., Chaki, T.K., 1993. Sintering behaviour and mechanical properties of hydroxyapatite and dicalcium phosphate. J. Mater. Sci. Mater. Med. 4, 150–158. https://doi.org/10.1007/BF00120384

Watts, D.C., 1993. Concise encyclopedia of medical and dental materials. J. Dent.

21, 317. https://doi.org/10.1016/0300-5712(93)90117-9

Watts, N.B., 1999. Clinical utility of biochemical markers of bone remodeling. Clin. Chem. 45, 1359–1368. https://doi.org/10.1093/clinchem/45.8.1359

Webster, T.J., 2001. Nanophase ceramics: The future orthopedic and dental implant material, in: Advances in Chemical Engineering. pp. 125–166. https://doi.org/10.1016/S0065-2377(01)27005-7

Webster, T.J., Massa-Schlueter, E.A., Smith, J.L., Slamovich, E.B., 2004. Osteoblast response to hydroxyapatite doped with divalent and trivalent cations. Biomaterials 25, 2111–2121. https://doi.org/10.1016/j.biomaterials.2003.09.001

Williams, D.F., 1987. Definitions in biomaterials: Proceedings of a consensus conference of the European Society for Biomaterials, Chester, England, March 3-5, 1986. Defin. Biomater. Proc. a Consens. Conf. Eur. Soc. Biomater. Chester, England, March 3-5, 1986,.

Woodruff, M.A., Hutmacher, D.W., 2010. The return of a forgotten polymer—Polycaprolactone in the 21st century. Prog. Polym. Sci. 35, 1217–1256. https://doi.org/10.1016/j.progpolymsci.2010.04.002

Xu, H.H.K., Carey, L.E., Simon, C.G., Takagi, S., Chow, L.C., 2007. Premixed calcium phosphate cements: Synthesis, physical properties, and cell cytotoxicity. Dent. Mater. 23, 433–441. https://doi.org/10.1016/j.dental.2006.02.014

Xue, W., Moore, J.L., Hosick, H.L., Bose, S., Bandyopadhyay, A., Lu, W.W., Cheung, K.M.C., Luk, K.D.K., 2006. Osteoprecursor cell response to strontium-containing hydroxyapatite ceramics. J. Biomed. Mater. Res. Part A 79A, 804–814. https://doi.org/10.1002/jbm.a.30815

Yang, C., Guo, Y. kui, Zhang, M. lin, 2010. Thermal decomposition and mechanical properties of hydroxyapatite ceramic. Trans. Nonferrous Met. Soc. China

(English Ed. 20, 254–258. https://doi.org/10.1016/S1003-6326(09)60131-X

Yang, W.-W., Pierstorff, E., 2012. Reservoir-based polymer drug delivery systems. J. Lab. Autom. 17, 50–58. https://doi.org/10.1177/2211068211428189

Yang, X., Wang, Z., 1998. Synthesis of biphasic ceramics of hydroxyapatite and β-tricalcium phosphate with controlled phase content and porosity. J. Mater. Chem. 8, 2233–2237. https://doi.org/10.1039/a802067a

Ye, H., Zhu, J., Deng, D., Jin, S., Li, J., Man, Y., 2019. Enhanced osteogenesis and angiogenesis by PCL/chitosan/Sr-doped calcium phosphate electrospun nanocomposite membrane for guided bone regeneration. J. Biomater. Sci. Polym. Ed. 30, 1505–1522. https://doi.org/10.1080/09205063.2019.1646628

Yin, H., Yang, C., Gao, Y., Wang, C., Li, M., Guo, H., Tong, Q., 2018. Fabrication and characterization of strontium-doped borate-based bioactive glass scaffolds for bone tissue engineering. J. Alloys Compd. 743, 564–569. https://doi.org/10.1016/j.jallcom.2018.01.099

Yılmaz, B., Evis, Z., 2016. Boron-Substituted Bioceramics: A Review. J. Boron 1, 6–14.

Yuan, Y., Liu, C., Zhang, Y., Shan, X., 2008. Sol–gel auto-combustion synthesis of hydroxyapatite nanotubes array in porous alumina template. Mater. Chem. Phys. 112, 275–280. https://doi.org/10.1016/j.matchemphys.2008.05.068

Zandinejad, A.A., Atai, M., Pahlevan, A., 2006. The effect of ceramic and porous fillers on the mechanical properties of experimental dental composites. Dent. Mater. https://doi.org/10.1016/j.dental.2005.04.027

Zhang, J., Zhang, H., Wu, L., Ding, J., 2006. Fabrication of three dimensional polymeric scaffolds with spherical pores. J. Mater. Sci. 41, 1725–1731. https://doi.org/10.1007/s10853-006-2873-7

Zhang, S., Prabhakaran, M.P., Qin, X., Ramakrishna, S., 2015. Biocomposite scaffolds for bone regeneration: Role of chitosan and hydroxyapatite within

poly-3-hydroxybutyrate-co-3-hydroxyvalerate on mechanical properties and in vitro evaluation. J. Mech. Behav. Biomed. Mater. 51, 88–98. https://doi.org/10.1016/j.jmbbm.2015.06.032

Zhao, J., Guo, L.Y., Yang, X.B., Weng, J., 2008. Preparation of bioactive porous HA/PCL composite scaffolds. Appl. Surf. Sci. 255, 2942–2946. https://doi.org/10.1016/j.apsusc.2008.08.056

Zhu, H., Guo, D., Sun, L., Li, H., Hanaor, D.A.H., Schmidt, F., Xu, K., 2018. Nanostructural insights into the dissolution behavior of Sr-doped hydroxyapatite. J. Eur. Ceram. Soc. 38, 5554–5562. https://doi.org/10.1016/j.jeurceramsoc.2018.07.056

Zhu, Q.-X., Li, Y.-M., Han, D., 2015. Co-substitution of carbonate and fluoride in hydroxyapatite: Effect on substitution type and content. Front. Mater. Sci. 9, 192–198. https://doi.org/10.1007/s11706-015-0294-8

Ziani, S., Meski, S., Khireddine, H., 2014. Characterization of magnesium-doped hydroxyapatite prepared by sol-gel process. Int. J. Appl. Ceram. Technol. 11, 83–91. https://doi.org/10.1111/ijac.12093

Zreiqat, H., Valenzuela, S.M., Nissan, B. Ben, Roest, R., Knabe, C., Radlanski, R.J., Renz, H., Evans, P.J., 2005. The effect of surface chemistry modification of titanium alloy on signalling pathways in human osteoblasts. Biomaterials 26, 7579–7586. https://doi.org/10.1016/j.biomaterials.2005.05.024

Zyman, Z., Tkachenko, M., Epple, M., Polyakov, M., Naboka, M., 2006. Magnesium-substituted hydroxyapatite ceramics. Materwiss. Werksttech. 37, 474–477. https://doi.org/10.1002/mawe.200600022